



저작자표시-비영리-변경금지 2.0 대한민국

이용자는 아래의 조건을 따르는 경우에 한하여 자유롭게

- 이 저작물을 복제, 배포, 전송, 전시, 공연 및 방송할 수 있습니다.

다음과 같은 조건을 따라야 합니다:



저작자표시. 귀하는 원저작자를 표시하여야 합니다.



비영리. 귀하는 이 저작물을 영리 목적으로 이용할 수 없습니다.



변경금지. 귀하는 이 저작물을 개작, 변형 또는 가공할 수 없습니다.

- 귀하는, 이 저작물의 재이용이나 배포의 경우, 이 저작물에 적용된 이용허락조건을 명확하게 나타내어야 합니다.
- 저작권자로부터 별도의 허가를 받으면 이러한 조건들은 적용되지 않습니다.

저작권법에 따른 이용자의 권리는 위의 내용에 의하여 영향을 받지 않습니다.

이것은 [이용허락규약\(Legal Code\)](#)을 이해하기 쉽게 요약한 것입니다.

[Disclaimer](#)

공학박사학위논문

**A study on damaged zone around an opening in rock-like  
material due to thermo-mechanical loading**

열-역학적 하중에 의한 암석모사시료 공동주변  
손상영역에 관한 연구

2017 년 2 월

서울대학교 대학원  
에너지시스템공학부

**ZHANG Nan**

**A study on damaged zone around an opening in rock-like  
material due to thermo-mechanical loading**

**열-역학적 하중에 의한 암석모사시료 공동주변  
손상영역에 관한 연구**

지도교수 전 석 원

이 논문을 공학박사 학위논문으로 제출함  
2016 년 10 월

서울대학교 대학원  
에너지시스템공학부  
ZHANG Nan

ZHANG Nan 의 공학박사 학위논문을 인준함  
2016 년 12 월

위 원 장 \_\_\_\_\_ (인)

부위원장 \_\_\_\_\_ (인)

위 원 \_\_\_\_\_ (인)

위 원 \_\_\_\_\_ (인)

위 원 \_\_\_\_\_ (인)

# **ABSTRACT**

## **A study on damaged zone around an opening in rock-like material due to thermo-mechanical loading**

ZHANG Nan

Department of Energy Systems Engineering

The Graduate School

Seoul National University

The influence of the elevated temperature on the evolution of the EDZ in the rock is an important issue for the safety assessment of radioactive waste repositories. The thermal stress induced additional damage may promote the degradation of mechanical properties of rock mass and increase the extent of the EDZ around the deposition openings which may provide a preferential pathway for radionuclides to migrate.

Biaxial compression tests were performed to investigate the brittle failure around the underground excavations using cubic mortar specimen with a central circular opening. Acoustic emission technique was applied to monitor the failure process around the circular opening. Three failure grades were identified base on the absolute AE energy results. Laboratory heater tests were conducted

under confined condition with both intact (undamaged) and damaged cement mortar specimen to study the effect of elevated temperature on the damaged zone. In addition, the effect of damaged zone to the temperature distribution was also investigated in the heater tests.

Numerical simulation were performed using an elastic damage model with the consideration of the heterogeneity of rock-like material to simulate the brittle failure around a circular opening under biaxial compression loading condition. Furthermore, based on the elastic damage model, the coupled thermo-mechanical analysis were implemented to simulate the laboratory heater tests. The validation of the proposed numerical model was achieved by comparison the simulation results with laboratory experimental results.

Furthermore, for the purpose of evaluating the applicability of the numerical model, numerical simulations were carried out to investigate the thermo-mechanical behaviors at the rock pillar in Äspö pillar stability experiment. The simulation results were agreed well with the simulation results from other numerical codes and the in situ experimental observations. It is believed that the results of this research can contribute to the understanding of coupled thermo-mechanical process in the damaged zone around a circular opening, in the context of deep geological disposal of high-level waste.

**Keywords: Thermo-mechanical, damaged zone, spalling, heater test, acoustic emission, numerical simulation.**

**Student Number: 2008-30707**

# TABLE OF CONTENTS

<b>ABSTRACT .....</b>	<b>i</b>
<b>TABLE OF CONTENTS .....</b>	<b>iii</b>
<b>LIST OF FIGURES.....</b>	<b>vi</b>
<b>1. Introduction .....</b>	<b>1</b>
1.1 Motivation .....	1
1.2 Research objectives .....	11
1.3 Outline of dissertation .....	12
<b>2. Literature review .....</b>	<b>13</b>
2.1 Excavation Damaged/Disturbed Zone (EDZ) .....	13
2.1.1 In situ investigation of EDZ.....	13
2.1.2 In situ heater tests in crystalline rock.....	19
2.2 Thermo-mechanical behavior of rock.....	30
2.2.1 Temperature-dependent properties of rock .....	30
2.2.2 Thermal cracking behavior of rock.....	34
<b>3. Laboratory experimental study .....</b>	<b>36</b>
3.1 Description of model test.....	38
3.1.1 Specimen and its properties .....	38
3.1.2 AE measurement system.....	45

3.2 Biaxial compression test.....	56
3.2.1 Experimental set-up and procedure .....	56
3.2.2 Results of biaxial compression tests .....	59
3.3 Heater tests .....	74
3.3.1 Experimental apparatus and procedure.....	74
3.3.2 Results of heater tests .....	80
<b>4. Numerical simulation.....</b>	<b>89</b>
4.1 Numerical model .....	89
4.1.1 Model description .....	89
4.1.2 Calibration of numerical model .....	95
4.2 Numerical simulation of biaxial compression test.....	98
4.3 Numerical simulation of heater test.....	102
4.4 Case study - Äspö Pillar Stability Experiment (APSE).....	122
<b>5. Conclusions and discussions.....</b>	<b>139</b>
5.1 Conclusions .....	139
5.2 Discussions .....	142
<b>References .....</b>	<b>143</b>
<b>Appendix.....</b>	<b>163</b>
<b>초 록.....</b>	<b>174</b>

# LIST OF TABLE

Table 2.1 Overview of measured results of excavation-induced damage from major experiments (Bäckblom, 2008).....	18
Table 3.1 Experimental scheme of the experimental study.....	37
Table 3.2 Physical and mechanical properties of cement mortar.....	41
Table 3.3 Brittleness index of cement mortar and two kinds of rocks.....	43
Table 3.4 Specifications of PICO sensor (PAC, 2011a).....	46
Table 3.5 Coordinates of AE sensors.....	49
Table 3.6 Summary of set-up parameters for AE measurement system.....	52
Table 3.7 The stress level of visible macro cracks and heavy spalling from four biaxial compression tests.....	63
Table 3.8 Depths and extents of failed zone of four tested specimens.....	71
Table 3.9 Specifications of thermocouple.....	76
Table 4.1 Input parameters for simulation of uniaxial compression test.....	96
Table 4.2 Comparison of the depth and extent between the test results and simulation results.....	101
Table 4.3 Input parameters for simulation of heater test.....	113
Table 4.4 Äspö diorite properties derived from laboratory tests (Staub et al. 2004, Andersson 2007, Kristensson and Hökmark 2007).....	125
Table 4.5 Analysis steps of the excavation stages in the 3D simulation.....	126
Table 4.6 Input parameters for 2D numerical simulation.....	130
Table 4.7 Pillar failure depths obtained from different numerical codes.....	138

# LIST OF FIGURES

Figure 1.1 Schematic illustration of a KBS-3V repository (SKB, 2004).....	2
Figure 1.2 Spalling in a vertical raise bored shaft in an underground mine (Hoek and Martin, 2014).....	3
Figure 1.3 Illustration of the brittle failure (spalling) (Martin et al. 2005). ....	4
Figure 1.4 Äspö Pillar Stability Experiment (APSE) at the experiment tunnel (Andersson, 2007). ....	6
Figure 1.5 Spalling observed at APSE pillar: (a) v-shaped notch; (b) spalling slab (Andersson, 2007).....	6
Figure 2.1 Sketch of failed, the damaged and the disturbed zone (Bäckblom and Martin, 1999).....	15
Figure 2.2 Summary of the EDZ characterisation methods (modified from Hudson et al., 2009) .....	17
Figure 2.3 Location of AECL’s Mine-by test tunnel and in-situ stress orientation (Martin and Christiansson, 2009).....	20
Figure 2.4 Spalling in the roof and floor at AECL’s Mine-by test tunnel (Read and Martin, 1996).....	20
Figure 2.5 Spalling developed in stage 1 of the HFT: view from top of borehole HFT and close-up view of breakout (Read, 2004). ....	21
Figure 2.6 Location of the Äspö pillar stability experiment (Andersson and Martin, 2009).....	22

Figure 2.7 Layout of ONKALO URL and the POSE-niche (Valli et al., 2013). .....	23
Figure 2.8 Schematic representation of the experimental area in the ONKALO underground facility (Siren et al., 2015). .....	24
Figure 2.9 Post-experiment fractures on the wall of experimental borehole ONK-EH3 (Valli et al., 2013).....	25
Figure 2.10 GPR responses (black areas represent the damaged volume) at experimental borehole ONK-EH3: (a) before heating; (b) after heating (Valli et al., 2013). .....	26
Figure 2.11 Layout of the KURT and location of the BHT area (Kwon et al., 2013). .....	28
Figure 2.12 Rock joints at BHT area (Kwon et al., 2013).....	28
Figure 2.13 Layout of the boreholes drilled for the BHT (Kwon et al., 2013). .....	29
Figure 3.1 Schematic diagram of the experimental scheme.....	37
Figure 3.2 Cubic cement mortar specimen with a central circular opening and front view of the specimen. ....	38
Figure 3.3 Stress-strain curve of cement mortar obtained from uniaxial compression test. ....	40
Figure 3.4 Mohr's failure envelope obtained from triaxial tests and typical failure pattern of cement mortar specimen after triaxial test.....	40
Figure 3.5 Microscopy image of cement mortar material (300X).....	44
Figure 3.6 Schematic layout of AE sensors.....	49

Figure 3.7 Three-view drawings of two sensor holders (mm). .....	50
Figure 3.8 Main parameters of AE waveform (Huang et al., 1998).....	53
Figure 3.9 Absolute energy features (Shahidan et al., 2016). .....	55
Figure 3.10 Schematic view of the test system of biaxial compression test. .	56
Figure 3.11 Experimental setup of biaxial compression test.....	57
Figure 3.12 Close-up view of experimental setup.....	57
Figure 3.13 Loading mode used in the biaxial compression test. ....	58
Figure 3.14 Brittle failure process around a circular opening. ....	59
Figure 3.15 Close-up view of the brittle failure. ....	59
Figure 3.16 Cumulative AE counts and count rate (#CM-M1).....	61
Figure 3.17 Cumulative absolute energy and absolute energy rate .....	62
Figure 3.18 AE source locations in three-dimensional view (#CM-M1). .....	64
Figure 3.19 Projection of AE sources localizations on xz-plane in each time interval: (a) 0~200 seconds; (b) 200~400 seconds; (c) 400~600 seconds; (d) 600~688 seconds and (e) 0~688 seconds (#CM-M1). .....	65
Figure 3.20 Illustration of the D-shaped tunnel with an effective tunnel radius (a) and the depth of failure ( $R_f$ ). (Martin et al., 1999).....	69
Figure 3.21 3D laser profiler. ....	70
Figure 3.22 3D contour of failed zone (#CM-M1). (Unit: mm).....	70
Figure 3.23 Profile of failed zone and calculation method of depth ( $d_f$ ) and extent ( $\theta$ ) of failed zone. ....	71

Figure 3.24 Relationship between normalized depth ( $d_f/a$ ) of failed zone and the stress level ( $\sigma_{\max}/\sigma_c$ ) in this research. ....	72
Figure 3.25 Comparison of normalized depth ( $d_f/a$ ) of failed zone and the stress level ( $\sigma_{\max}/\sigma_c$ ) between laboratory test results and field observations (modified from Martin et al., 1999 and Cheon, 2006) .....	72
Figure 3.26 Summary of uniaxial testing of blocks containing a circular opening (Martin, 1997). ....	73
Figure 3.27 Ratio of the calculated tangential stress to $\sigma_c$ at which breakouts initiate for various borehole diameters (Martin, 1997). ....	73
Figure 3.28 Watlow cartridge heater. ....	75
Figure 3.29 Heater control unit. ....	75
Figure 3.30 K-type thermocouple. ....	76
Figure 3.31 Schematic view of the thermocouple arrangement: (a) 3D view; (b) close-up view; (c) top view; (d) side view. ....	77
Figure 3.32 Experimental setup of heater test. ....	79
Figure 3.33 Close-up view of the experimental setup. ....	79
Figure 3.34 Temperature evolution at six temperature monitoring points in heater test (#CM-TM). ....	81
Figure 3.35 Cumulative absolute energy, absolute energy rate and heater temperature in heater test (#CM-TM). ....	82
Figure 3.36 AE source locations in heater test (#CM-TM). ....	82
Figure 3.37 Close-view of the circular opening after heater test (#CM-TM). ....	83

Figure 3.38 Temperature evolution at six monitoring points in heater test (#CM-M-TM).....	85
Figure 3.39 Cumulative absolute energy, absolute energy rate and heater temperature in heater test (#CM-M-TM). .....	86
Figure 3.40 Fractures were initiated on the surface of the circular opening ..	86
Figure 3.41 Fractures coalescence with the pre-existing failed zone .....	87
Figure 3.42 AE source locations in heat test (#CM-M-TM). .....	87
Figure 4.1 Stress-strain curve of cement mortar from uniaxial compression test and numerical simulation.....	97
Figure 4.2 Comparison of damage pattern between test result (left) and simulation result (right) under uniaxial compression test. ....	97
Figure 4.3 Geometry of numerical specimen and boundary condition. ....	98
Figure 4.4 Simulation results of the damaged zone (distribution of Young's modulus) around circular opening under biaxial compression loading condition: (a) step 20; (b) step 30; (c) step 50; (d) step 60. (Unit: Pa).....	100
Figure 4.5 Coordinates of the triangular mesh. (Unit: m) .....	101
Figure 4.6 Test samples for thermal conductivity and specific heat measurements.....	105
Figure 4.7 Test specimen for coefficient of thermal expansion measurement. .....	106

Figure 4.8 Thermal conductivity and specific heat of cement mortar: (a) thermal conductivity; (b) specific heat; (c) coefficient of thermal expansion.....	106
Figure 4.9 Schematic view of the method for calculating the temperature at the surface of the circular opening (#CM-TM).....	109
Figure 4.10 Schematic view of hollow cylinder.....	110
Figure 4.11 The calculated temperature evolution curve at the surface of the circular opening (#CM-TM).....	111
Figure 4.12 Schematic view of test condition of heater test (#CM-TM). ....	112
Figure 4.13 Comparison of simulation results and test results at different temperature monitoring points: (a) TC#1, TC#2, TC#3; (b) TC#4, TC#5, TC#6 (#CM-TM).....	114
Figure 4.14 Simulated damaged zone around the circular opening. (Unit: Pa) .....	115
Figure 4.15 Schematic view of the test condition of heater test (#CM-M-TM). .....	116
Figure 4.16 Schematic view of the method for calculating the temperature at the surface of the circular opening (#CM-M-TM). .....	117
Figure 4.17 The calculated temperature evolution curve at the surface of the circular opening ( $T_a$ ).....	117
Figure 4.18 Comparison of simulation results and test results at different temperature monitoring points: (a) TC#1, TC#2, TC#3; (b) TC#4, TC#5, TC#6 (#CM-M-TM).....	119

Figure 4.19 Simulated damaged zone around circular opening: (a) before heating; (b) after heating (#CM-M-TM). (Unit: Pa) .....	120
Figure 4.20 Orientation of the APSE tunnel in relation to the direction of major principal stress (Andersson, 2007).....	123
Figure 4.21 General layout and theoretical section of the APSE tunnel (Andersson, 2007). .....	123
Figure 4.22 Model geometry for 3D simulation.....	124
Figure 4.23 Simulation results after the final excavation stage: (a) cross-section at top of the borehole (x-z plane); (b) tangential stress at the top of borehole. (Unit: MPa) .....	127
Figure 4.24 Excavation induced maximum tangential stress at the surface of borehole (Andersson, 2007). .....	128
Figure 4.25 Layout of boreholes heaters and sensors (Andersson, 2007)....	129
Figure 4.26 Heater power (Andersson, 2007). .....	129
Figure 4.27 Mesh of 2D numerical model (20m×10m). .....	131
Figure 4.28 Temperature distribution after heating 66 days. (Unit: °C).....	132
Figure 4.29 Temperature evolution at monitor point A: (a) simulation results; (b) measured results (Andersson et al., 2009). .....	132
Figure 4.30 Comparison of tangential stress: (a) 3D model (cross-section at 3.5m below the tunnel floor)) after final excavation step; (b) 2D model (initial condition). (unit: MPa) .....	134
Figure 4.31 Simulated damaged zone after heating 66 days. ....	135

Figure 4.32 Simulated damaged zone: after heating (a) 10 days; (b) 20 days;  
(c) 46 days; (d) 66 days. (Unit: Pa) ..... 135

Figure 4.33 Photographs of failure pattern on rock pillar in APSE (Andersson,  
2007). ..... 137

Figure 4.34 Failure depths simulated by different numerical codes: ..... 137

# **1. Introduction**

## **1.1 Motivation**

The thermo-mechanical response of rock is a critical research issue in many fields such as geological sequestration of CO<sub>2</sub> (Shiu et al., 2011; Rutqvist, 2012), compressed air energy storage (Mohanto et al., 2014), enhanced geothermal systems (Ghassemi, 2012; Rutqvist et al., 2015), underground coal gasification (Otto and Kempka, 2015) and nuclear waste repository (NWR) (Hudson et al., 2009; Tsang et al., 2012) which are usually subject to complex thermo-mechanical conditions. It is vitally important to study the thermo-mechanical behavior of rock mass which may be subjected to elevated temperatures.

The permanent disposal of high-level waste (HLW) is one of the major technical hurdles that must be addressed. The main challenge is that the waste must be effectively isolated from the biosphere for hundreds of thousands of years (Birkholzer et al., 2012). Deep geological disposal is considered to be the most practical and effective method for isolating HLW (IAEA, 2009). Extensive researches have been carried out at the underground research laboratories (URLs) for the long-term performance assessment of the NWR.

One of the concepts for deep geological disposal of HLW which proposed by Swedish Nuclear Fuel and Waste Management Company (SKB) is the KBS-3V method as shown in Figure 1.1. In this method, the HLW will be encapsulated in copper canisters and deposited in vertical deposition holes, then canisters are embedded in a buffer consisting of compacted bentonite clay, and above all, the deposition galleries should be excavated at about 500 m depth in crystalline rock.

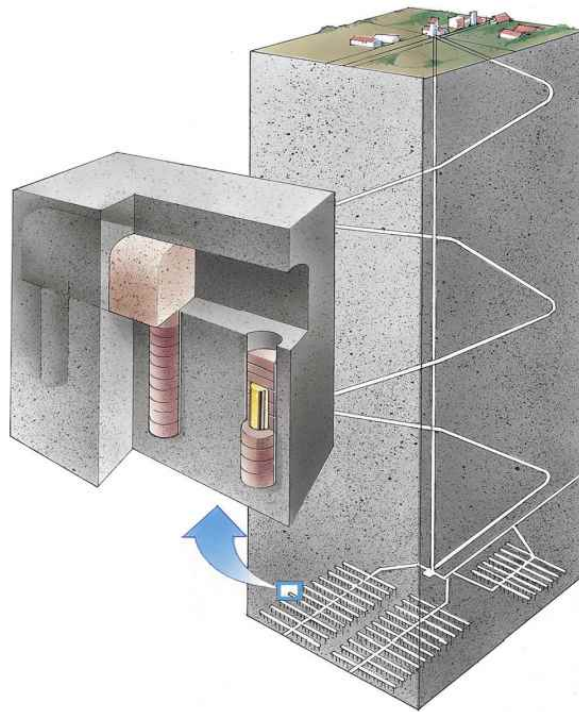


Figure 1.1 Schematic illustration of KBS-3V repository (SKB, 2004).

In the process of excavating underground openings, the excavation induced disturbance and damage to the rock mass adjacent to the opening is inevitable. In particular, under high in-situ stresses condition, the excavation induced responses in brittle hard rock would be severe, brittle failure (or spalling) is commonly found at deep sparsely fractured rock mass (Martin, 1997; Bäckblom and Martin, 1999; Martino and Chandler, 2004; Read, 2004). An example of spalling in the sidewalls of a vertical raise bored shaft in an underground mine was shown in Figure 1.2. Martin and Christiansson (2009) pointed out that spalling around the underground opening is a significant issue in repository design (Figure 1.3).



Figure 1.2 Spalling in a vertical raise bored shaft in an underground mine (Hoek and Martin, 2014).

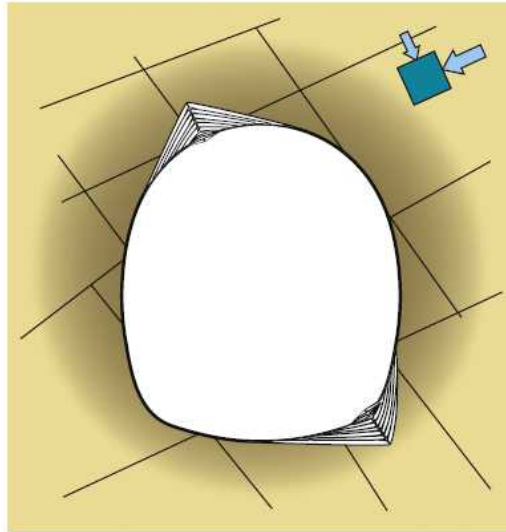


Figure 1.3 Illustration of the brittle failure (spalling) (Martin and Christiansson, 2009).

In order to investigate the brittle failure process and the formation of spalling, extensive laboratory experiments on rock or rock-like materials have been carried out (Ewy and Cook, 1990; Carter et al., 1991; Fakhimi et al., 2002). Experimental observations suggest that one of the mechanisms of spalling is the compressive failure near free surface caused by tensile fractures propagating parallel to the major principal compressive stress direction and the resulting failed zone is commonly referred to as breakout or v-shaped notch as noted by Martin, (1997).

One of key issues when assessing the performance of the NWR is related to the effects of the temperature elevation due to the heat emitted from placement canister (Pusch, 2008).

The elevated temperature can cause expansion of rock mass, the resulting thermal stress will be concentrated around the boundary of deposition tunnels and deposition holes and cause an increase in the tangential stresses. If the tangential stresses exceed the spalling strength of the rock mass, the openings may become unstable (Martin and Christiansson, 2009). Hudson et al. (2009) emphasized that the thermal stresses can have high magnitudes and extensive damage in the EDZ will be resulted. Backers et al. (2014) provided review comments on SKB's post-closure safety analysis and concluded that spalling is an issue during the excavation phase and spalling is potentially severe during the thermal phase. And more than 90% of the deposition holes during the thermal phase, spalling can be expected. Stephansson and Gipper (2015) reviewed SKB's post-closure safety analysis and mentioned that SKB has an incomplete understanding of the combined effect of EDZ, stress induced rock failure (spalling) and thermal driven process. They recommend SKB to conduct laboratory testing of thermal properties on dry specimens, for the scenario in which rock, buffer and backfill are dry.

The international cooperative project DECOVALEX-2011 (DEvelopment of COupled models and their VALidation against EXperiments) Task B selected the Äspö Pillar Stability Experiment (APSE, Figure 1.4) at SKB's Hard Rock Laboratory (HRL) as research target for validation and comparison of different numerical models in reference to the numerical modelling of the failure process and the spalling phenomena (Figure 1.5) in crystalline rock under coupled thermo-mechanical loading condition (Andersson, 2007).

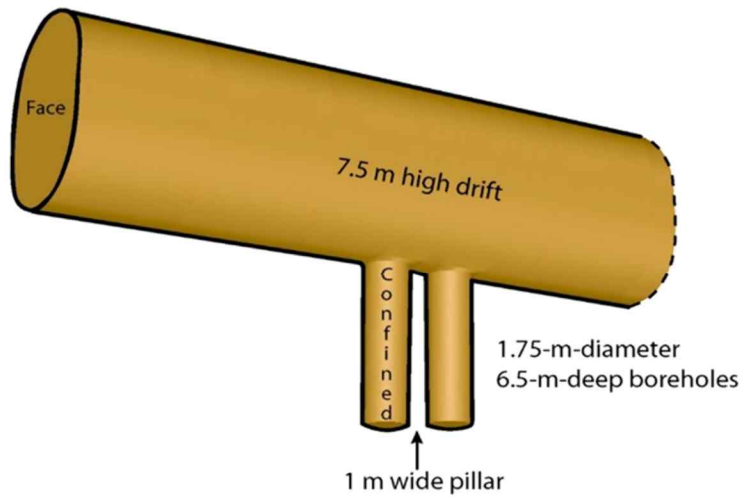
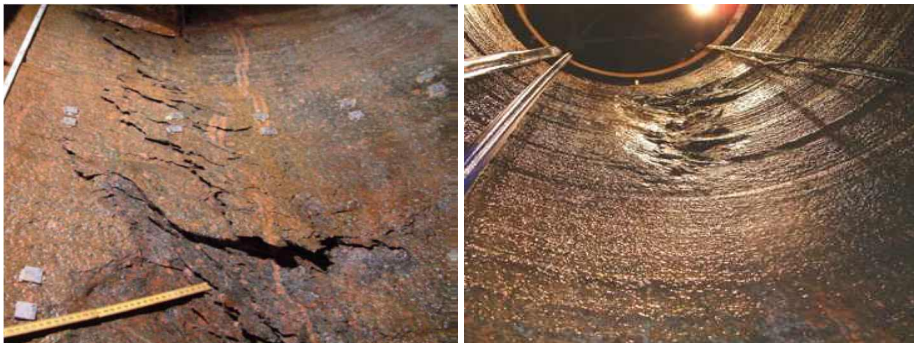


Figure 1.4 Äspö Pillar Stability Experiment (APSE) at the experiment tunnel (Andersson, 2007).



(a) v-shaped notch

(b) spalling slabs

Figure 1.5 Spalling observed at APSE pillar: (a) v-shaped notch; (b) spalling slab (Andersson, 2007).

The conclusions from this experiment suggest that for crystalline rocks, the damage processes in laboratory experiments and in situ appear to be very similar. The field findings infer that heterogeneity play an important role in the evolution of the damage (Andersson et al., 2009; Lan et al., 2013).

Other international cooperative research such as European research project TIMODAZ (Thermal IMPact On the Damaged Zone), focused on the potential effect of the thermal impact on the EDZ in the near field of clay host rocks. The main results of this research project indicate that because of the favorable properties of the clay host rock result in a good self-sealing capacity which guarantee the effectiveness of the safety functions of the repository system, the EDZ would not be considered as a critical issue in the long-term safety of NWR in clay formations (Delage 2013; Li et al., 2014).

Numerical simulation of brittle failure has been carried out by many researchers using different numerical methods. In case of the finite element method (FEM), Hajiabdolmajid et al. (2002) proposed the cohesion weakening friction strengthening (CWFS) constitutive model and implemented using FLAC to simulate the brittle failure observed in Atomic Energy of Canada Limited (AECL)'s Mine-By Experiment (MBE) tunnel. Diederichs (2007) applied Damage Initiation Spalling Limit (DISL) model to predict the spalling depths around the MBE tunnel using the FEM code Phase2.

Cundall (2001) made an overview of the application of discrete element method (DEM) in rock mechanics and explained this method is well suited for the simulation of realistic fracturing in rocks. Fakhimi et al. (2002) used PFC2D

to simulate the spalling observed during a biaxial compression test on a sandstone specimen with a circular opening. Potyondy and Cundall (2004) simulated the excavation induced spalling observed at the MBE tunnel using PFC-FLAC model. Shin et al. (2007) applied the grain-based model using UDEC successfully simulated the spalling damage around MBE tunnel. Garza-Cruz et al. (2014) used 3DEC to investigate spalling of massive to moderately jointed rock masses.

Hybrid methods such as the Finite/Discrete Element Method (FDEM) method combine aspects of both FEM and DEM can model rock fracturing behaviour (Sun et al. 2016). Klerck (2000) applied ELFEN which is based on FDEM to model rock failure under compressive loads. Barla and Antolini (2014) illustrated the use of the FDEM to model the rock spalling behaviour in deep tunnels. Lisjak et al. (2015) applied FDEM to investigate the formation process of the EDZ around a test tunnel at the Mont Terri rock laboratory which embedded in Opalinus clay formation.

Hsiung et al. (2005) simulated coupled thermo-mechanical processes which expected to occur at the potential repository at Yucca Mountain using FLAC. Kwon and Cho (2008) studied the influence of EDZ on the thermo-mechanical behaviors of an underground excavation using FLAC3D. The coupled thermo-mechanical analysis of the far-field impact of thermal loading on the NWR have been carried out by Min et al. 2005; Klubertanz et al. 2008. It was found that the thermal impact leads to vertical heaving and horizontal

tensile displacement above the repository. Wanne and Young (2008) used PFC2D to simulate thermal cracking around a circular opening in Lac du Bonnet granite cylinder specimen which was heated under unconfined condition and found that cracks increased slowly until the temperature reached a critical value, after which cracks increase more rapidly. Koyama et al. (2013) simulated coupled thermo-mechanical processes and spalling phenomena in APSE using self-developed DEM code. However, the generated cracks were few and spalling phenomena observed at site could not be captured sufficiently.

Although, the above numerical approaches have their own advantages in numerical simulations. However, the heterogeneity of rock is not considered in these previous works. It is generally known that rock is a heterogeneous material containing different natural defects (Hudson and Harrison, 1997). Laouafa et al. (2016) pointed out that thermo-mechanical response of a medium is highly dependent on its heterogeneity. Thus, it is necessary to take into consideration of the heterogeneity of rock in the coupled thermo-mechanical simulation.

In terms of laboratory scale heater tests, Carlson et al. (1993) conducted a heater test using Lac du Bonnet granite cylinder specimen (300mm in diameter and 220mm in length) to study thermally- induced cracking processes. A cartridge heater was placed into central hole to heat the cylinder specimen until 245°C (Figure 1.6). The test results shown that a macrocrack formed and initiated from the outer surface of the specimen.

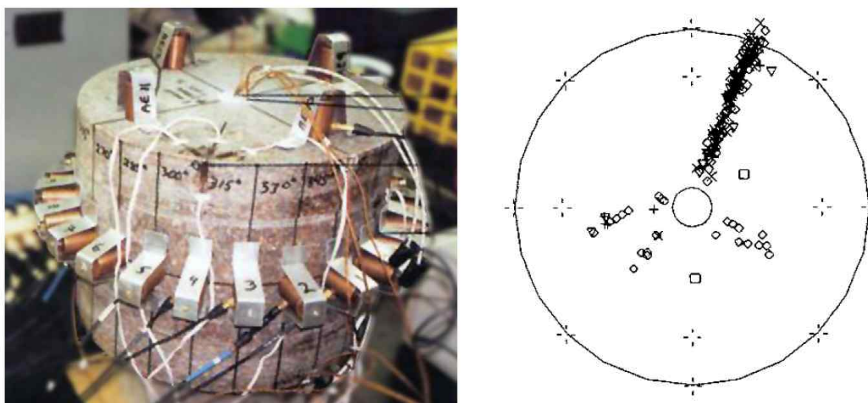


Figure 1.6 The Lac du Bonnet granite specimen during the heated experiment and recorded AE source locations (Wanne and Young, 2008).

Jansen et al. (1993) and Ishida et al. (2004) carried out similar laboratory heater tests using cubic granite specimen. They found similar tests results as Carlson. However, it should be noted that the above laboratory scale heater tests were carried out under unconfined condition which is not the realistic underground conditions. Wai et al. (1982) pointed out that for the evaluation of rock stability under thermal conditions in design problems the case of stability under confined heating should be considered. Chernis and Robertson (1993) investigated the thermal cracking in Lac du Bonnet granite during slow heating to 205°C and found the confining pressure will reduce the effects of temperature. Wang et al. (2013) investigated thermal cracking behavior of the La Peyratte granite up to 700°C and concluded that the confining pressure played an important role in thermal cracking which need to be thoroughly investigated. Therefore, it is necessary to carried out laboratory heater test under confined condition.

## **1.2 Research objectives**

The main objectives of this research are as follows:

- (1) To investigate the brittle failure around a circular opening under biaxial compression condition.
- (2) To study the effect of temperature elevation on the evolution of damaged zone and the temperature distribution around the damaged zone.
- (3) To simulate the brittle failure around the circular opening and the temperature distribution around the damaged zone through numerical analysis using FEM code (COMSOL Multiphysics).
- (4) To verify the applicability of the proposed numerical model.

### **1.3 Outline of dissertation**

Chapter 1 gives an introduction of the motivations and objectives of this research. In Chapter 2, a literature review of the in-situ investigation of the EDZ and three in-situ heater tests which have been performed in crystalline rock are presented. The temperature dependent properties and thermal cracking behavior of rock were also introduced. In Chapter 3, the laboratory experimental apparatus and procedures of laboratory biaxial compression test and heater test are introduced. The test results are presented and discussed. In Chapter 4, the numerical models were validated by comparing simulation results with the experimental results. A case study is also presented in this Chapter. Chapter 5 draws the main conclusions of this research and the limitations of this research are also discussed.

## **2. Literature review**

In this Chapter, brief review of the in-situ EDZ researches will be given which places emphasis on the in-situ heater tests related to the underground nuclear waste disposal. In the second part of this Chapter, the previous laboratory experimental studies on the thermo-mechanical behavior of rocks will be given in two aspects: temperature-dependent properties of rock (including mechanical and thermal properties) and the thermal cracking behavior of rock.

### **2.1 Excavation Damaged/Disturbed Zone (EDZ)**

#### **2.1.1 In situ investigation of EDZ**

The concept of excavation induced damage zone has been studied since the early 1980s and the first field study in relation to nuclear waste disposal were performed at the Stripa mine experiments in Sweden (Kelsall et al., 1984).

Various definitions of this zone have been given since it has been studied in different types of rock or under different geological environments (Bäckblom, 2008). It is necessary to have a clear interpretation of the definition at the beginning of this research. The terminology “disturbed zone” was applied in Pusch and Stanfors (1992). Fairhurst and Damjanac (1996) used the terms

“Excavation Damaged Zone (EDZ) and Disturbed Rock Zone (DRZ)” to describe the region which has been significantly damaged or disturbed due to the redistribution of in situ stresses. Emsley et al. (1997) defined the EDZ as “a damaged zone closest to the drift wall dominated by changes in material properties which are mainly irreversible” and the Excavation Disturbed Zone (EdZ) as “a disturbed zone outside the damaged zone dominated by changes in stress state and hydraulic head and where changes in rock properties are small and mainly reversible and it is considered that there are no, or insignificant, material property changes”. Bäckblom and Martin (1999) defined the excavation disturbed zone including the damaged and failed zone as shown in Figure 2.1. In the failed zone, rock slabs are detached completely from the rock mass as a result of spalling, therefore, the failed zone is also referred to as spalling zone. “Damaged zone” is a zone closest to the underground opening that has suffered irreversible deformation. “Disturbed zone” is a zone where the changes in rock mass properties are insignificant or reversible.

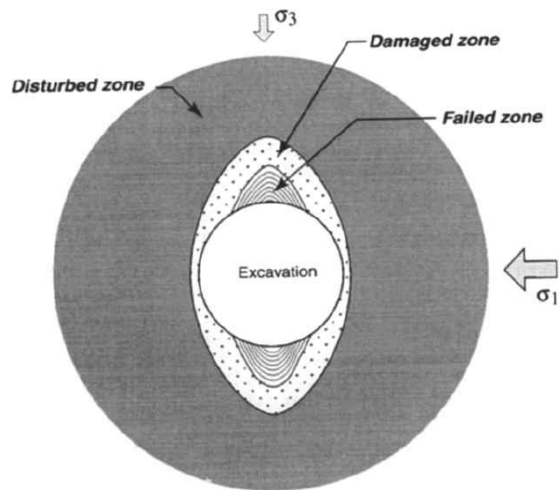


Figure 2.1 Sketch of failed, the damaged and the disturbed zone (Bäckblom and Martin, 1999).

Many studies related to EDZ have been carried out with different focuses, for instance, formation and long-term processes (Blümling et al., 2007), depth of damage (Bäckblom, 2008), and changes in permeability (Ababou et al., 2011). In a recent overview, Tsang et al. (2005) summarized key processes, parameters and technical issues for the EDZ in different rock types including crystalline rocks, clays (indurated clays, plastic clays) and rock salt which are the most commonly considered rock types for nuclear waste storage.

In this section, the review will focus on the study of the EDZ in crystalline rock type. Studies related to other rock types are beyond the scope of this research, which can be referred to relevant literatures in the case of clays (Martin et al., 2003; Bossart et al., 2004; Labiouse and Vietor, 2014) and rock salt (Hou, 2003; Pudewills, 2006).

The EDZ in crystalline rock have been investigated in the URLs by worldwide nuclear agencies. In situ experiments at URLs have provided valuable knowledge for calibrating models and the development of site investigation techniques. NEA (2013) gave a systematic summarization of the main URLs in the world that were constructed in different geological media. Among them, the most well documented investigations of the EDZ, at full scale in hard rock, are summarized by Bäckblom and Martin (1999), including the research projects such as the Stripa project (Fairhurst et al., 1993) at Stripa mine and ZEDEX (Zone of Excavation Disturbance Experiment) project (Emsley et al., 1997) at Äspö HRL in Sweden and the Mine-by Experiment (MBE) (Read and Martin, 1996) at URL in Canada were initiated specifically to investigate the EDZ.

The extent of EDZ is one of the main concern for the design of nuclear waste repositories. In general, the extent of EDZ is affected by factors such as: in-situ stress conditions, excavated opening shape and its orientation relative to the maximum stress, excavation method (Martino and Chandler, 2004).

For hard brittle crystalline rock, the excavation activity could induce significant damage, depending on the excavation method used. For example, in the ZEDEX project, Emsley et al (1997) found the extent of the damaged zone is significantly greater in the drift excavated by blasting compared to the drift excavated by TBM.

The EDZ characterisation methods were systematically summarized by Hudson et al. (2009) as shown in Figure 2.2. Bäckblom (2008) made an overview of the field experiments conducted related to the EDZ research and summarized the main findings of the field experiments as shown in Table 2.1.

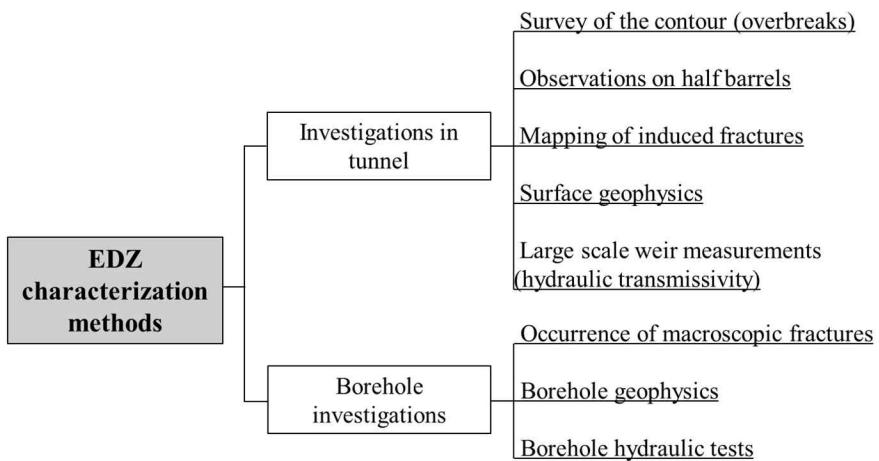


Figure 2.2 Summary of the EDZ characterisation methods (modified from Hudson et al., 2009)

Table 2.1 Overview of measured results of excavation-induced damage from major experiments (Bäckblom, 2008).

Experiment	Excavation method	Equivalent Test Scale [m]	Mode	Mechanically defined extension of damage [m]	Hydraulic parameter results
Stripa – Rock Sealing Experiment	Drill and Blast,	~ 10–15 m The test covers approximately four rounds	Excavation-induced	0–0.8 m	Hydraulic conductivity 1·10 <sup>-8</sup> m/s but 2·10 <sup>-8</sup> m/s in the floor. The hydraulic conductivity of the most shallow 1–2 dm rock is probably 5·10 <sup>-8</sup> –1·10 <sup>-7</sup> m/s.
AECL – Room 209 Connected Permeability Test	Drill and Blast	~ 0–5 m for connected permeability tests ~ 0.03 m for borehole permeability tests. The test covers 1–2 rounds	Excavation-induced	0.3 m in the floor	Hydraulic conductivity "increased 1 to 2 orders" (i.e. around 10 <sup>-12</sup> –10 <sup>-11</sup> m/s) for the 0.3 m closest to the periphery based on permeability tests and transient pulse tests. However, the hydraulic conductivity based on flow measurement was estimated to be approximately 10 <sup>-9</sup> m/s.
AECL – Mine-by Tunnel Connected Permeability Test.	Mechanical excavation using line-drilling	~ 0–5 m for connected permeability tests	Stress-induced with spalling	"Process zone" due to spalling of width 0.2 m (extending beyond the break-out notch 0.3 m below the design level of the floor)	Hydraulic conductivity 10 <sup>-6</sup> m/s based on flow measurements and 0.7·10 <sup>-8</sup> m/s based on tracer tests. Transport porosity 3.3% and longitudinal dispersivity of 0.6 m.
AECL – Tunnel Sealing Experiment	Drill and Blast	~ 0–5 m The test covers 1–2 rounds	Excavation-induced	< 1 m. The blast-induced damage is 0.3 m as concluded by AECL	Hydraulic conductivity of 2·10 <sup>-8</sup> m/s.
AECL – Blast Damage Assessment Project	Drill and Blast	~ 0–5 m The test covers 1–2 rounds	Excavation-induced	< 0.6 m	Hydraulic conductivity in the order of 2·10 <sup>-8</sup> m/s to 8·10 <sup>-7</sup> m/s.
SKB – ZEDEX	Drill and Blast	~ 1 m The test covers 11 rounds	Excavation-induced	0.3 m in walls and 0.8 m in the floor	Permeability of approximately 10 <sup>-16</sup> m <sup>2</sup> for a few measured sections (corresponding to a hydraulic conductivity of 10 <sup>-6</sup> m/s).
	Tunnel Boring Machine	~ 1 m	Excavation-induced	0.03 m	Hydraulic conductivity in the range of 2·10 <sup>-9</sup> to 5·10 <sup>-12</sup> m/s from the tunnel wall to 4.5 mm depth. 5·10 <sup>-12</sup> to 5·10 <sup>-13</sup> m/s from 4.5 to 10 mm depth. The undisturbed rock matrix was estimated to be about 5·10 <sup>-13</sup> m/s. (Data from the Äspö HRL TBM tunnel).
SKB – APSE	Drill and Blast	~ 0–5 m	–	–	–
SKB – Prototype repository	Tunnel Boring Machine	~ 1 m	Excavation-induced	10 mm	Hydraulic conductivity of 1–2.5·10 <sup>-10</sup> m/s.
Posiva – Olkiluoto	Mechanical excavation of deposition holes	<< 1 m	Excavation-induced	< 21 mm	Hydraulic conductivity of 7·10 <sup>-13</sup> m/s.
Nagra – Near-Field Tunnel Programme	Drill and blast and mechanical excavation using Tunnel Boring Machine	0–3 m	Excavation-induced and possibly stress-induced	0–2 m	Matrix permeability of 3·10 <sup>-18</sup> m <sup>2</sup> and effective permeability of 2.2·10 <sup>-15</sup> m <sup>2</sup> (corresponding to a hydraulic conductivity of 2.2·10 <sup>-8</sup> m/s).
ENRESA – FEBEX	Mechanical excavation using Tunnel Boring Machine	<< 0.01 m	Excavation-induced	< 3 mm	–
JAEA; EDZ II	Drill and Blast	~ 0–5 m	Excavation-induced and stress-induced	1 m. Damage possibly due to spalling and blasting damage	Hydraulic conductivity in the order of 10 <sup>-5</sup> m/s.

### **2.1.2 In situ heater tests in crystalline rock**

To understand the complex coupling phenomenon in the NWR, in situ heater tests have been implemented world widely at the URLs. A summarization of the main in situ heater tests can be found in Kwon et al. (2013). Among these tests, in situ heater tests have been conducted in hard crystalline rock, such as AECL's Heated Failure Test (HFT) in Canada, SKB's Äspö Pillar Stability Experiment (APSE) in Sweden, POSIVA's Olkiluoto Spalling Experiment (POSE) in Finland and KAERI's borehole heater test (BHT) in Korea.

#### **AECL's Heated Failure Test (HFT), Canada**

The Mine-By Experiment (MBE) was carried out in a test tunnel (Figure 2.3) at 420 m depth in the AECL's URL which seated in highly stressed Lac du Bonnet granite (Read, 2004). Spalling were found in the roof and floor of the test tunnel as shown in Figure 2.4.

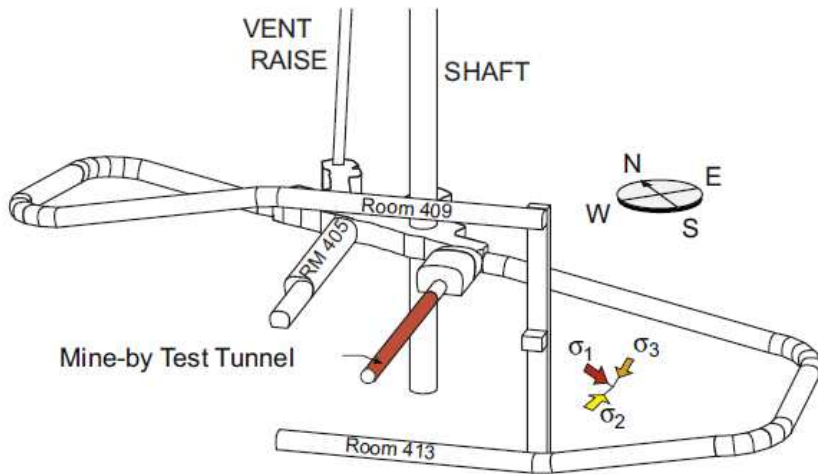


Figure 2.3 Location of AECL's Mine-by test tunnel and in-situ stress orientation (Martin and Christiansson, 2009).



Figure 2.4 Spalling in the roof and floor at AECL's Mine-by test tunnel (Read and Martin, 1996).

As the first in situ large scale heater test, HFT (1993-1996) was implemented in the same area as the MBE test tunnel. The main objective of HFT was to investigate the thermal effects on excavation damage development around the opening. The HFT were executed at the tunnel floor in four stages for the purpose of assessing the effects of drilling/heating sequence, borehole interaction and internal confining pressure on the development of excavation damage. Two 600mm diameter holes were bored for making the pillar between them. Four electrical heaters located about 1 meter from the hole walls were used to heat the pillar up to 85 °C in 20 days (Read et al., 1997). The observed spalling at stage 1 of the HFT where heating commenced after completion of drilling is shown in Figure 2.5. The observed spalling in the borehole was a radial extent of 45 mm. The experiment results shown that spalling initiated through localized damage. The combination of stress localization due to the developing spalling geometry and increasing tangential stress due to heating caused the spalling to extend into relatively undamaged rock (Read, 2004).

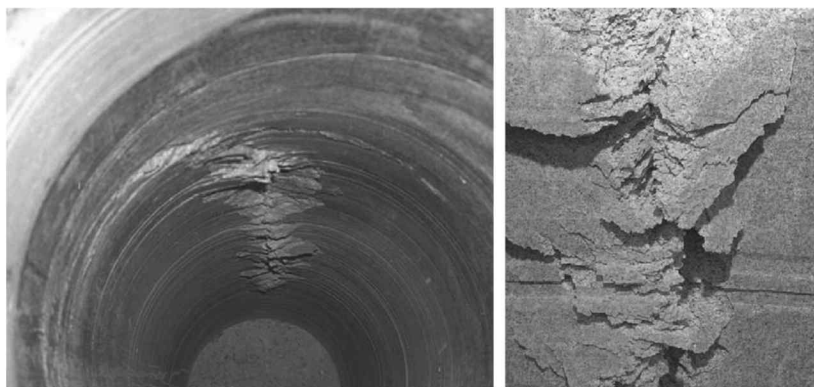


Figure 2.5 Spalling developed in stage 1 of the HFT: view from top of borehole HFT and close-up view of breakout (Read, 2004).

## SKB's Äspö Pillar Stability Experiment (APSE), Sweden

The APSE (2003-2004) was performed in an experimental tunnel which was excavated perpendicular to the maximum principal stress and located at a depth of 450 m in the Äspö HRL of SKB (Figure 2.6). The main objective of APSE is to investigate the formation and growth of the EDZ and spalling mechanism under excavation and heating processes in a crystalline rock.

The major difference between the HFT and APSE is that HFT was performed in an almost unfractured rock mass whereas the APSE located in fractured rock mass (Andersson, 2003). The APSE used the confining pressure of 1000 kPa compared to the 100 kPa used at HFT. Spalling developed close to center of the pillar (Figure 1.5) where the tangential stresses were the highest (Andersson, 2007). More detailed description about the field condition of the APSE and experimental results was given in section 4.4.

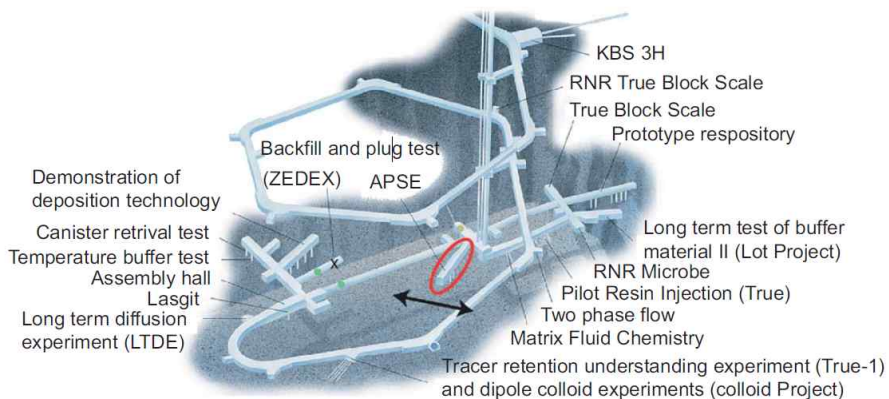


Figure 2.6 Location of the Äspö pillar stability experiment (Andersson and Martin, 2009).

## POSIVA's Olkiluoto Spalling Experiment (POSE), Finland

POSIVA had plans for the disposal of HLW which are based on the SKB's KBS-3 concept. The rock mass at Olkiluoto consists of migmatitic gneiss with pegmatitic granites. Because the gneissic rocks can behave differently from the granitic rock in the HFT test and APSE experiment, the Posiva's Olkiluoto Spalling Experiment (POSE) was designed and carried out in the ONKALO URL at depth of 345m as shown in Figure 2.7 (POSIVA, 2009).

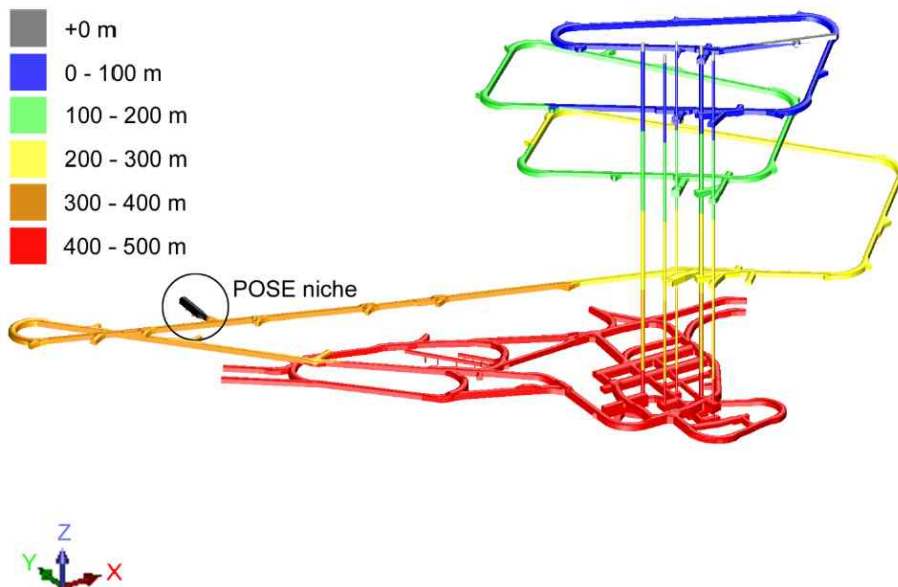


Figure 2.7 Layout of ONKALO URL and the POSE-niche (Valli et al., 2013).

The POSE experiment (2011-2013) consisted of three phases (Figure 2.8) as follows:

In the first phase (or Pillar damage test), a pillar was made between two experimental holes ( $\Phi 1.524$  m) through boring of two experimental boreholes (ONK-EH1 & ONK-EH2). No spalling or surface type damage except minor damage was detected. More details can be found in Johansson et al. (2014).

In the second phase (or pillar heating damage test), the test scheme is similar with the ASPE. A small area (20 cm x 20 cm) of spalling was found in the open borehole. More damage was found in the confined borehole due to low confining pressure about 4-60 kPa (Johansson et al., 2014).

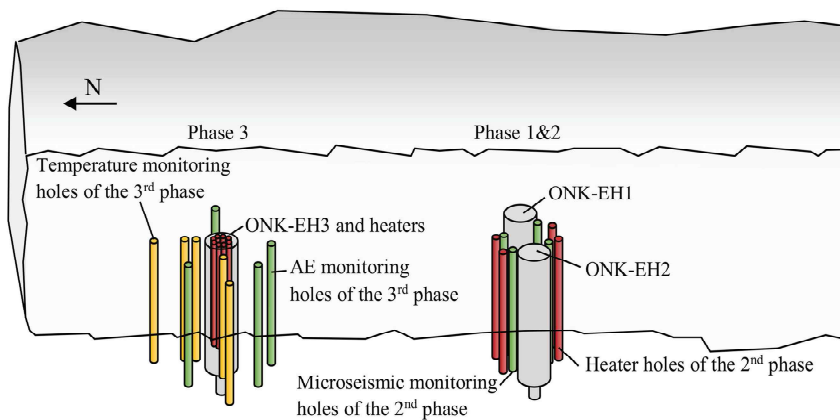


Figure 2.8 Schematic representation of the experimental area in the ONKALO underground facility (Siren et al., 2015).

In the third phase (or single hole heating damage test), experimental borehole (ONK-EH3) was filled with sand and heated to about 85°C from the inside for about three months. Spalling is not observed in the hole. Only few fractures were propagated further and minor new fractures initiated as shown in Figure 2.9.

For the purpose of monitoring the heating damage, Ground Penetrating Radar (GPR) EDZ technique was applied to the wall of experimental borehole ONK-EH3. The monitoring results of GPR responses at borehole ONK-EH3 before and after heating are shown in Figure 2.10. It can be seen that the damage around the wall of borehole got deeper and became more continuous after heating. The increase of damage depth was from 60–120 mm (before heating) to 120–180 mm (after heating) (Valli et al., 2013).

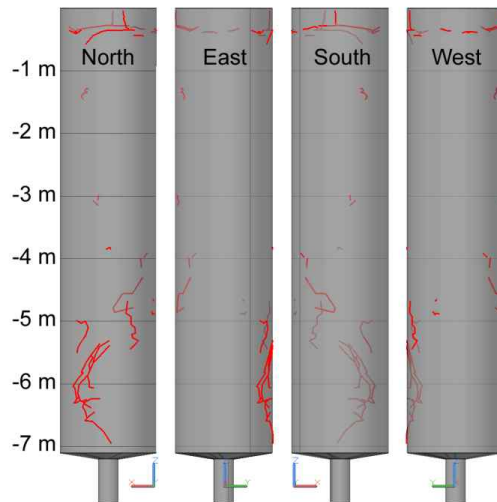
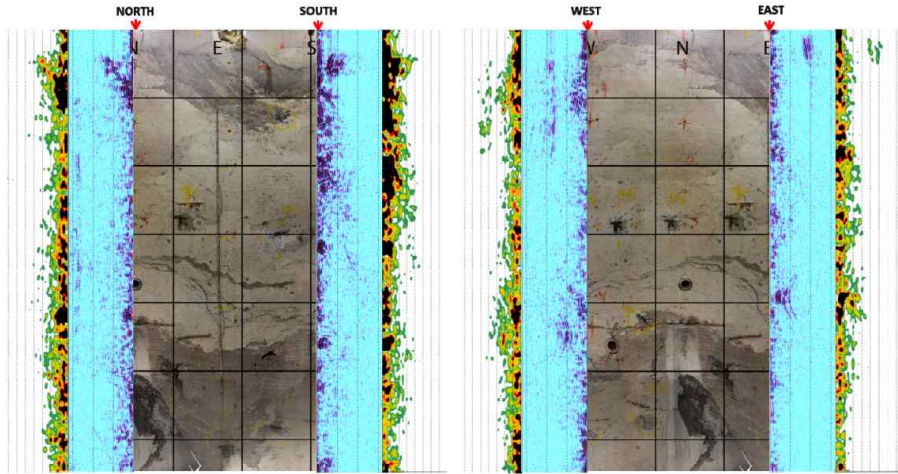
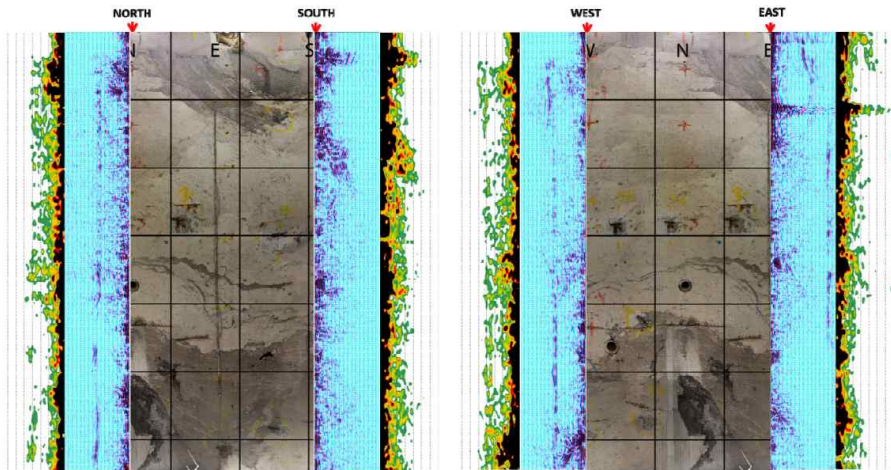


Figure 2.9 Post-experiment fractures on the wall of experimental borehole ONK-EH3 (Valli et al., 2013).



(a) before heating



(b) after heating

Figure 2.10 GPR responses (black areas represent the damaged volume) at experimental borehole ONK-EH3: (a) before heating; (b) after heating (Valli et al., 2013).

The main finding of this experiment is that only EDZ type damage was observed as proved by GPR results. This is largely due to the behaviour of the rock which seems to be governed mostly by heterogeneous features. (Valli, et al., 2013)

### **KAERI's Borehole Heater Test (BHT), Korea (2007-2011)**

In 2005-2006, KURT (KAREI Underground Research Tunnel) was constructed to validate the nuclear waste disposal system in Daejeon, Korea. KURT is located at a granite body with a maximum depth about 90m, it includes a 180 m long access tunnel with two research modules. The layout of KURT and the location of the BHT is shown in Figure 2.11. The new extension projects which started in 2015 is in progress.

The BHT focuses on the mechanical and thermal behavior and research module I was selected for the reason of relatively dry condition of rock mass. The test area (12 m long, 6.3 m high and 6.9 m wide) which contains countable joints (Figure 2.12) was isolated from the ventilation system with a fabricated wall. It would be possible to examine the effect of a single fracture or simple fracture network on the thermal-and mechanical behavior (Kwon et al., 2013).

A 3.2 m long horizontal heater hole was drilled with a diameter of 110 mm. Heater (2m in length) with a maximum power of 5 kW was designed and manufactured with aluminum. Totally fifteen observations holes (38 mm in diameter) were drilled around the heater hole as shown in Figure 2.13.

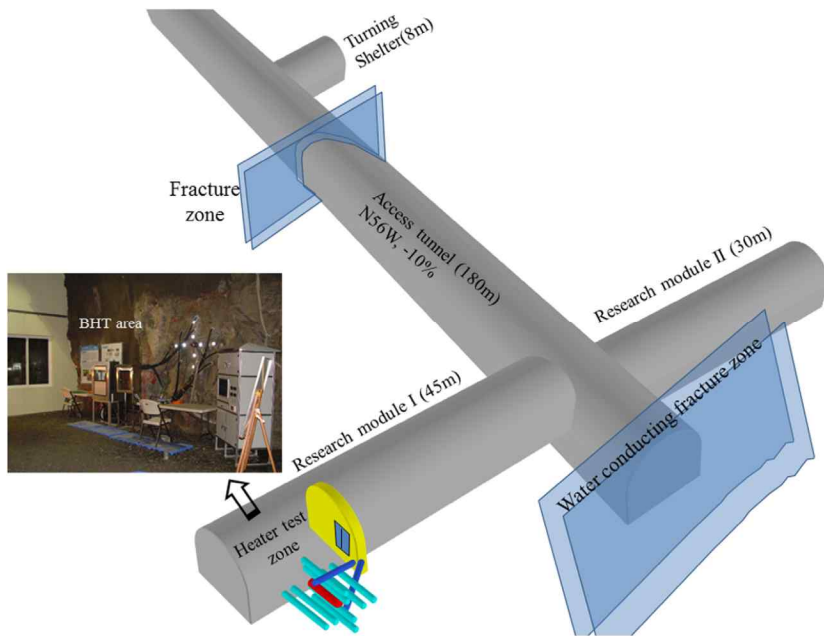


Figure 2.11 Layout of the KURT and location of the BHT area (Kwon et al., 2013).



Figure 2.12 Rock joints at BHT area (Kwon et al., 2013).

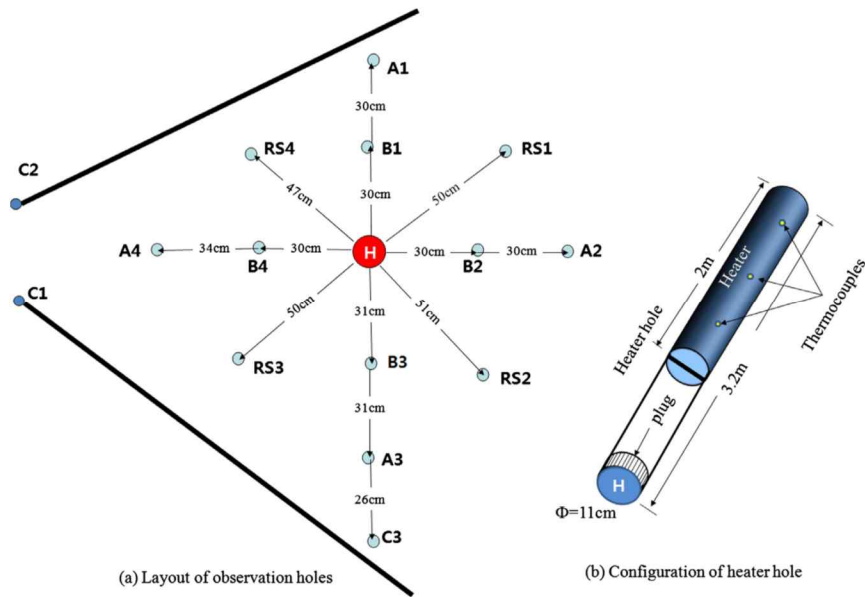


Figure 2.13 Layout of the boreholes drilled for the BHT (Kwon et al., 2013).

The heater temperature was increased steadily to the target temperature of 90°C and maintained for about 2 years. Then the heater temperature was increased to 118°C to examine the response of the rock under abnormal overheating conditions about 1 year, the peak temperatures at the observation holes located at 0.3 m and 0.6 m away from the heater hole was about 50 °C and 37 °C, respectively.

The main finding from the BHT is as follows: the mean rock temperatures and average joint spacing changed similarly with the distance from the tunnel wall. For example, the lower rock temperature measured at about 3-3.5m from the tunnel wall could be explained by the effect of groundwater flowing through the joints located in that area.

## **2.2 Thermo-mechanical behavior of rock**

The effect of temperature on rocks has been studied widely through laboratory-scale experiments using rock core samples. These experiments were generally conducted with two main purposes: one is to investigate the effect of temperature on rock properties and the other one is to study the thermal cracking behavior of rock (Homand-Etienne and Houpert, 1989; Miao et al., 2014).

### **2.2.1 Temperature-dependent properties of rock**

#### **Temperature-dependent mechanical properties of rock**

The knowledge of the variation of mechanical and thermal properties of rock under elevated temperature is important to understand and model coupled processes in the NWR. Laboratory experimental studies have been widely conducted to investigate effect of temperature on the mechanical properties of different rock types.

The test results show that the elastic modulus and strength of rocks generally decrease with the increase of temperature due to the thermally-induced cracks (Heuze, 1983; Araujo et al., 1997; Ferrero and Marini, 2001; Keshavarz et al., 2010).

By contrast, some test results showed that these properties may not decrease monotonically with the increase of temperature as found by Ranjith et al. (2012) and Zhang et al. (2014).

### **Temperature-dependent thermal properties of rock**

The thermal properties of rock in the near-field of the repository are considered as key parameters for the design and long-term safety assessment of NWR (Cho and Kwon, 2010). Most researches on temperature-dependent thermal properties of rocks focus on three topics: thermal conductivity, specific heat and thermal expansion coefficient.

#### **Thermal conductivity ( $\lambda$ )**

Thermal conductivity is the intrinsic property of a material which defines its ability to transfer heat. In SI unit, thermal conductivity is measured in  $W/(m \cdot K)$ .

Thermal conductivity is one of the key parameters in the design of the NWR because it was directly related to the evaluation of the necessary repository volume and the optimization of the repository layout (Sundberg and Hellström, 2009). For example, in KBS-3 concept, the limit of the maximum temperature for bentonite buffer is 100 °C, the spacing between canisters was determined by the thermal conductivity of the host rock.

The canisters cannot be deposited too close to each other, to prevent the potential high temperature. Conversely, larger spacing between canisters will be inefficient and uneconomic. (Hökmark et al., 2009).

Thermal conductivity widely ranges for different rock types. For low porosity rocks, temperature has a major effect on variation of thermal conductivity, generally, thermal conductivity of rock decreases with the increase of temperature. For high porosity rocks such as sandstone, the overall thermal conductivity usually decrease with increasing porosity, because of pore filled with fluids and gases which have lower value of thermal conductivity (Poelchau et al. 1997).

Many laboratory tests have been conducted to measure the thermal conductivity of rocks. It should be noted that there are much discrepancies among the test results. One reasonable explanation for these discrepancies is the different degrees of saturation in the test specimens. Schärli and Rybach (1984) measured the thermal conductivities of five granitic rocks and found the thermal conductivity of water-saturated specimens is about 30% higher than dry specimens.

In case of dry rocks, Barry-Macaulay et al. (2013) found increase in thermal conductivity with an increase in density based on the tests results of siltstone, sandstone and basalt dry samples.

### **Specific heat capacity ( $C_p$ )**

The specific heat (also noted as “specific heat capacity”) of a material is the amount of heat per unit mass required to raise the temperature by one degree. The SI unit of specific heat is (J/(kg·K)).

Specific heat of rocks plays an important role in controlling heat flow when rocks are heating up or cooling down quickly (Waples and Waples, 2004). Kukkonen and Lindberg (1998) summarized the previous experimental data and concluded that the specific heat of low-porosity crystalline rocks is controlled by the specific heat of the individual minerals and their relative amounts in the rock. In addition, the specific heat of rocks is temperature dependent and it increases with increasing temperature.

### **Thermal expansion coefficient ( $\alpha$ )**

The thermal expansion coefficient,  $\alpha$ , characterizes the ability of the material to contract or expand because of temperature variations. The linear thermal expansion coefficient in SI unit is (K)<sup>-1</sup>.

The knowledge of thermal expansion coefficient is needed, because the surrounding rock mass in the NWR will expand due to the elevated temperature. The thermally-induced stress may make the strength of rock mass be exceeded. And the differences in thermal expansion properties among different rock formations may cause cracks and spalling (Johansson and Rautakorpi, 2000).

Huotari and Kukkonen (2004) made a literature survey of the thermal expansion properties of rocks and concluded that thermal expansion properties of rocks increase with the increase in the temperature. More recently, Plevova et al. (2016) measured the thermal expansion coefficient of five different type of granite rocks and also found this tendency.

### **2.2.2 Thermal cracking behavior of rock**

There are two types of thermal cracking in rocks (Zhang, 2016). One is called intergranular cracking which is caused by the mismatch of thermal expansion coefficients between adjacent minerals which lead to grain boundary cracking. The other one is known as intragranular cracking, which means cracking occurs within a grain due to the thermal expansion anisotropy of mineral.

Handin et al. (1977) studied the thermal cracking of Sioux quartzite during slow thermal cycling and found that a confining pressure of 50 MPa reduced the effects of thermal cracking at 400°C by 50%. Friedman et al. (1979) measured the failure strength of granodiorite after heated to 1000°C and found the heated specimen was as strong as the unheated specimen under confining pressure 50 MPa. However, in unconfined tests, the strength of the heated specimen was dramatically reduced.

Previous studies in crystalline rocks have shown that there is a threshold temperature below which there is no microcracking due to elevated temperature. For example, the threshold temperature of Charcoal granodiorite is about 75°C (Bauer and Johnson, 1979) and threshold temperature of Westerly granite is in the range from 60 to 70°C (Yong and Wang, 1980). Chernis and Robertson (1993) observed the thermal cracking behavior in Lac du Bonnet granite with slow heating to 205° C and found the confining pressure reduces the effects of temperature, but its effect on threshold temperature is not precisely known. David et al. (1999) summarized the previous laboratory test results which show that thermal cracking can dramatically change elastic modulus and mechanical strength of rocks.

### **3. Laboratory experimental study**

In this laboratory experimental study, biaxial compression tests were carried out to investigate the brittle failure around a circular opening using cubic cement mortar specimen with a central circular opening.

Laboratory heater tests were conducted using both intact (undamaged) and damaged cement mortar specimen under confined condition. The influence of elevated temperature on the damaged zone and the effect of damaged zone on temperature distribution were investigated. The experimental scheme in this experimental study is shown in Table 3.1. The schematic diagram of the experimental scheme is shown in Figure 3.1. Specimen #CM-M1 to #CM-M4 were split into half by splitter after biaxial compression test, for measuring the depth and extent of failed zone using 3D laser profiler. Specimen #CM-M-TM was firstly damaged through biaxial compression test, then it was used in heater test under confined condition. Specimen #CM-TM was used directly in heater test under confined condition.

Table 3.1 Experimental scheme of the experimental study.

Groups	Specimen No.	Biaxial compression test	Heater test
#1	# CM-M1	Yes	No
	# CM-M2		
	# CM-M3		
	# CM-M4		
#2	# CM-M-TM	Yes	Yes
	# CM-TM	No	Yes

CM: cement mortar; M: biaxial compression test; TM: heater test under thermo-mechanical loading condition (i.e. confined condition).

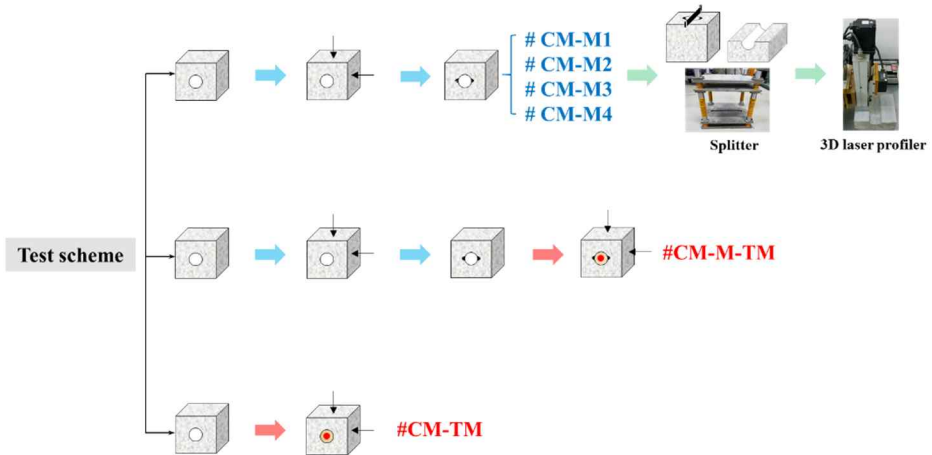


Figure 3.1 Schematic diagram of the experimental scheme.

### 3.1 Description of model test

#### 3.1.1 Specimen and its properties

Laboratory tests of rock-like material have been widely carried out as an effective research method (Cao et al., 2016). Cement mortar has been used as the rock-like material because its brittle feature, in addition, it can be made to desired shape and size with low cost for reproduction. In this research, the cubic cement mortar specimens (170mm in side length) with a central circular opening (50mm in diameter) were casted as shown in Figure 3.2. The dimension of the specimen is decided base on the size of the existing biaxial loading frame.

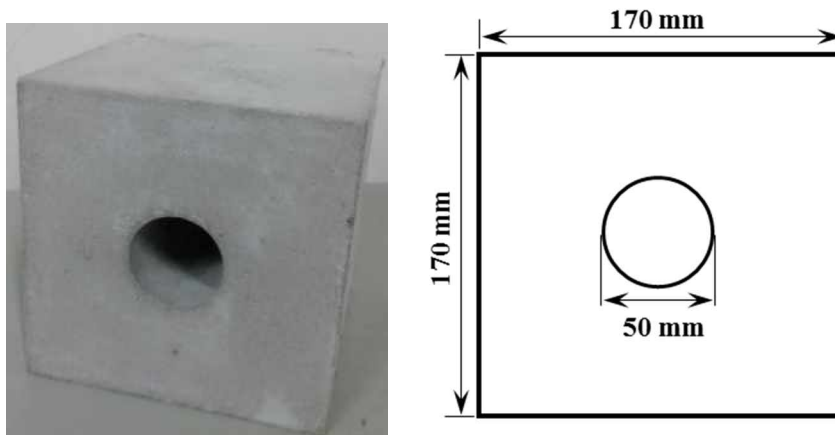


Figure 3.2 Cubic cement mortar specimen with a central circular opening and front view of the specimen.

Ultra rapid hardening cement (UNION Grout JM type) was used to make cement mortar specimens. Cement mortar specimen was casted with aluminum model frame and the pre-existing circular opening was created by inserting a PVC cylinder. The mixing ratio of cement to water as 2:1 by weight. After casting, specimens were kept in the molds and covered with plastic sheet for the purpose of preventing evaporation for 24 hours, then specimens were demolded and cured in the water tank. On the curing age of day-7, specimen was removed from the tank and placed in drying oven, dried under 105°C for about four days and a constant weight was obtained. It should be noted that the complete dried condition of specimens is vitally important to the consistency and reproducibility of biaxial compression tests and heater tests results.

Cylinder specimens (100mm in height and 50mm in diameter) were casted for determining the physical and mechanical properties of cement mortar through performing standard laboratory tests. The material testing system (MTS) was employed for the uniaxial compression tests. The end surfaces of cylinder specimens were ground using grinding machine to make sure parallelism and smoothness of the surfaces. Two appropriate size steel platens were used to ensure the axial load can be evenly transmitted to the specimen. Biaxial strain gage (Tokyo Sokki, FCA-5-11) was used for the strain measurements. The stress-strain curve of cement mortar obtained from uniaxial compression test is shown in Figure 3.3. Shear strength parameters of mortar were obtained from triaxial compression tests using a Hoek cell under different confining pressures.

The Mohr's failure envelope obtained from triaxial tests and typical failure pattern of cement mortar specimen after triaxial test are shown in Figure 3.4. The physical and mechanical properties of the cement mortar were summarized in Table 3.2.

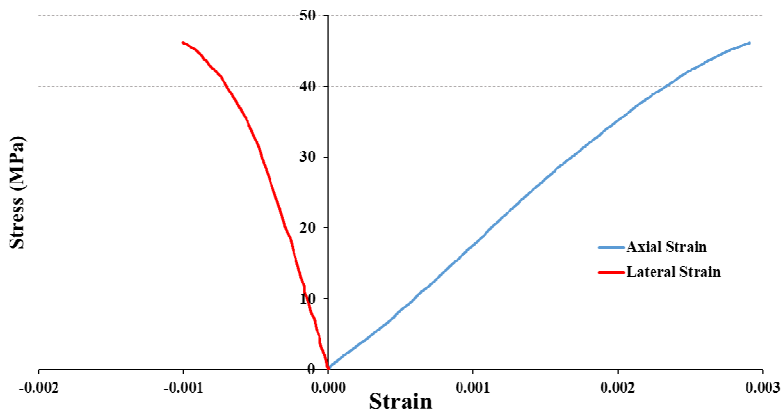


Figure 3.3 Stress-strain curve of cement mortar obtained from uniaxial compression test.

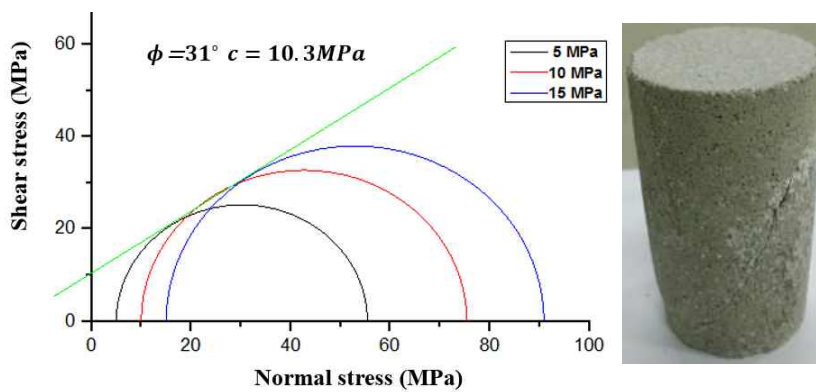


Figure 3.4 Mohr's failure envelope obtained from triaxial tests and typical failure pattern of cement mortar specimen after triaxial test.

Table 3.2 Physical and mechanical properties of cement mortar.

<b>Properties</b>	<b>Value</b>	<b>Unit</b>
Uniaxial compression strength, $\sigma_c$	46.2	MPa
Brazilian tensile strength, $\sigma_t$	4.1	MPa
Young's modulus, E	18.2	GPa
Poisson's ratio, $\nu$	0.28	-
Friction angle, $\phi$	31	°
Cohesion, c	10.3	MPa
Density, $\rho$	1,950	kg/m <sup>3</sup>
Porosity	11	%
P-wave velocity, $V_p$	4010	m/s
S-wave velocity, $V_s$	2105	m/s

Brittleness index is commonly used to quantify brittleness of rocks and rock-like materials. In order to confirm the brittleness of the cement mortar used in this research, brittleness index of the cement mortar are calculated and compared with two rocks including Hudong granite and Paldang gneiss (Jung, 2010).

Various indices of brittleness have been proposed to quantify the brittleness of rocks (Hucka and Das, 1974; Goktan and Yilmaz 2005). The most widely applied five equations for indirectly quantify the brittleness were summarized by Tiryaki (2006) as follows:

$$B_1 = \frac{\sigma_c}{\sigma_t} \quad (3.1)$$

$$B_2 = \frac{\sigma_c - \sigma_t}{\sigma_c + \sigma_t} \quad (3.2)$$

$$B_3 = \frac{\sigma_c \times \sigma_t}{2} \quad (3.3)$$

$$B_4 = \frac{\sigma_c + \sigma_t}{2} \quad (3.4)$$

$$B_5 = \frac{2(\sigma_c \times \sigma_t)}{(\sigma_c + \sigma_t)} \quad (3.5)$$

where  $\sigma_c$  is uniaxial compressive strength (UCS) and  $\sigma_t$  is Brazilian tensile strength.

Because of the UCS of rocks are much larger than the UCS of cement mortar, the calculated values from B<sub>3</sub>, B<sub>4</sub>, B<sub>5</sub> of rocks are much larger than the cement mortar. Therefore, B<sub>1</sub> and B<sub>2</sub> are applicable to compare the brittleness between cement mortar and rocks.

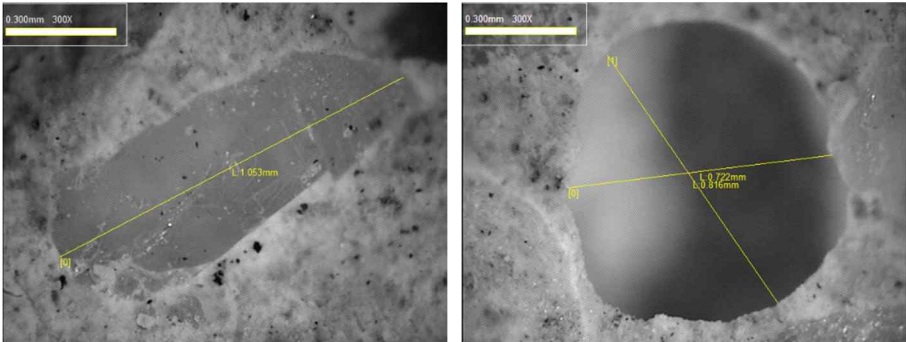
The brittleness index B<sub>1</sub> and B<sub>2</sub> of cement mortar and two kinds of rocks (Hudong granite and Paldang gneiss) are in the same range as shown in Table 3.3, thus the cement mortar used in this research is considered as brittle material.

Table 3.3 Brittleness index of cement mortar and two kinds of rocks.

Material	Brittleness index				
	B1	B2	B3	B4	B5
Cement mortar	11.27	0.84	94.7	25.2	7.5
Hudong granite*	9.06	0.8	459.6	50.7	18.1
Paldang gneiss*	11.02	0.83	694.9	67.5	20.6

\*test results from Jung (2010).

Cement mortar material can be considered as a composite consisting of silica sand (in this research, grain size, about 1~2 mm), cement paste, unhydrated cement and void space, with each phase having its own distinct characteristics, that is, with different strengths and deformability. The microscopy observation of cement mortar material was carried out using video microscope (ICAMSCOPE). The silica sand and void space associated with the inherent structure of cement mortar material are shown in Figure 3.5, the heterogeneity and complex geometry of the voids are apparent.



Silica sand

Void space

Figure 3.5 Microscopy image of cement mortar material (300X)

### 3.1.2 AE measurement system

AE is a phenomenon of a transient stress waves resulting from a sudden release of elastic energy, caused by mechanical deformations, initiation and propagation of microcracks and other irreversible changes in material (ASTM, 2006). AE technique have been widely applied for characterizing and evaluating the failure process of rock or rock-like materials (Michlmayr et al., 2012; Liu et al., 2015; Gholizadeh et al., 2015).

The AE measurement system used in this research was manufactured by Physical Acoustic Corporation (PAC) which is composed of four PCI-2 boards with a total of eight AE channels. AE signals were detected through six PICO sensors (PAC, 2011a). The small size of the sensor guarantees precise sensor coordinates for localization purposes. The main specifications of PICO sensor are listed in Table 3.4. AE signals were amplified by six PAC-1220A preamplifiers with 60 dB gain due to the high attenuation of signal transmission in mortar material. Using appropriate couplant is crucial to the sensor sensitivity and accuracy of AE measurement. High vacuum silicone grease (Shin-Etsu Chemical, HIVAC-G) was used as couplant, it exhibits excellent thermal stability, can be used in a temperature up to 200°C and quite suitable for laboratory heater tests.

Table 3.4 Specifications of PICO sensor (PAC, 2011a).

<b>Specification</b>	<b>Value</b>	<b>Unit</b>
Dimension (diameter× height)	5 × 4	mm
Weight	<1	g
Operating temperature range	-65 to 177	°C
Operating frequency range	200 - 750	kHz
Resonant frequency	250	kHz

AE wave velocity is one of the key input parameters of the AE measurement system and needs to be determined prior to the test by conducting pencil lead break (PLB) test which generates repeatable acoustic signals and has been widely accepted as a standard technique to simulate the natural AE source (ASTM, 2015). Beattie (2013) emphasized that because the acoustic properties vary with both material and geometry, it is advisable to measure the wave velocities in the actual test specimen directly.

In this research, the AE wave velocity was determined experimentally through the PLB tests on actual test mortar specimens following the ASTM E976-15 (2015) using 2H mechanical pencil lead with 0.5 mm in diameter and  $3 \pm 0.5$  mm in length, by pressing it with a 30 degree inclination against the specimen surface. Two AE sensors were used in the measurement. Three lead break points were selected on the straight line between the sensors and three lead breaks were conducted at each point.

The difference in time of arrival was calculated using the first peak of the signal received at two sensors (Godin et al., 2011; Sinaga et al., 2011). AE wave velocity was calculated from the distance of the sensors divided by the time difference of arrival. The mean value of AE wave velocity of mortar specimen was calculated to be 1960 m/s and was used as setup parameter for the AE measurement system.

Three AE sensors were attached to the front surface and back surface of the specimen, respectively. All sensors were attached to the left side of the specimen, based on two main concerns. Firstly, thermocouples will be installed at the right side of the specimen. Secondly, in heater test, specimen will be heated for several hours, keeping good sensor-specimen coupling under moderate temperatures during long periods of time (several hours) is difficult due to the small size of sensors ( $5 \times 4$  mm). Therefore, two sensor holders were designed and applied to insure the adequate and stable coupling between the sensor and the specimen.

Pencil lead tests were carried out on the specimen surface at known positions, the estimated source location was compared with the real locations. By trial and error, different sensor layouts were tested and the best sensor layout which has the lowest error was selected as shown in Figure 3.6. The coordinates of AE sensor are shown in Table 3.5.

Before performing the AE measurement, the attached points of AE sensors on the specimen surfaces were carefully polished using fine sand paper to eliminate all irregularity and cleaned carefully to remove the powder, then a

thin layer of the high vacuum silicon grease was applied to ensure the good sensor-specimen coupling.

AE sensors were placed into the sensor holders, then sensor holders were fixed on the biaxial loading frame using magnets to ascertain close contact between sensor holder and specimen surface. The springs were used behind the sensors in order to apply constant pressure on the sensor back to keep them in contact with the specimen surface at all times. Three-view drawings of two sensor holders are shown in Figure 3.7.

Table 3.5 Coordinates of AE sensors.

Sensor No.	AE sensors coordinates (mm)		
	x	y	z
#1	30	130	170
#2	50	85	170
#3	30	40	170
#4	40	145	0
#5	30	85	0
#6	40	25	0

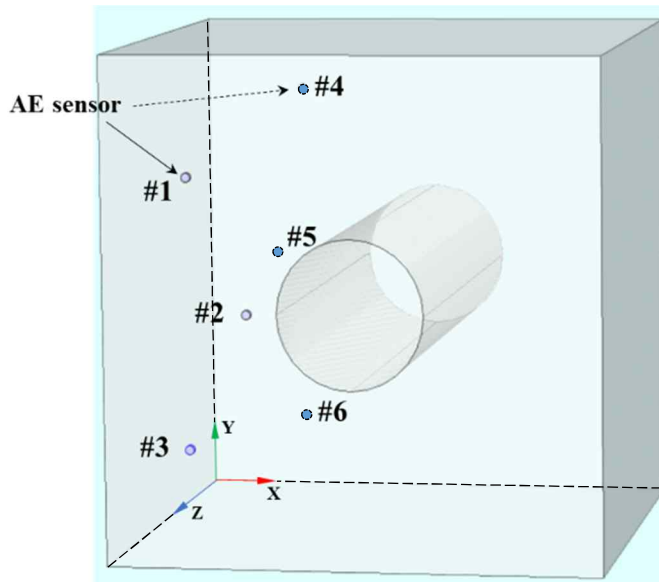


Figure 3.6 Schematic layout of AE sensors.

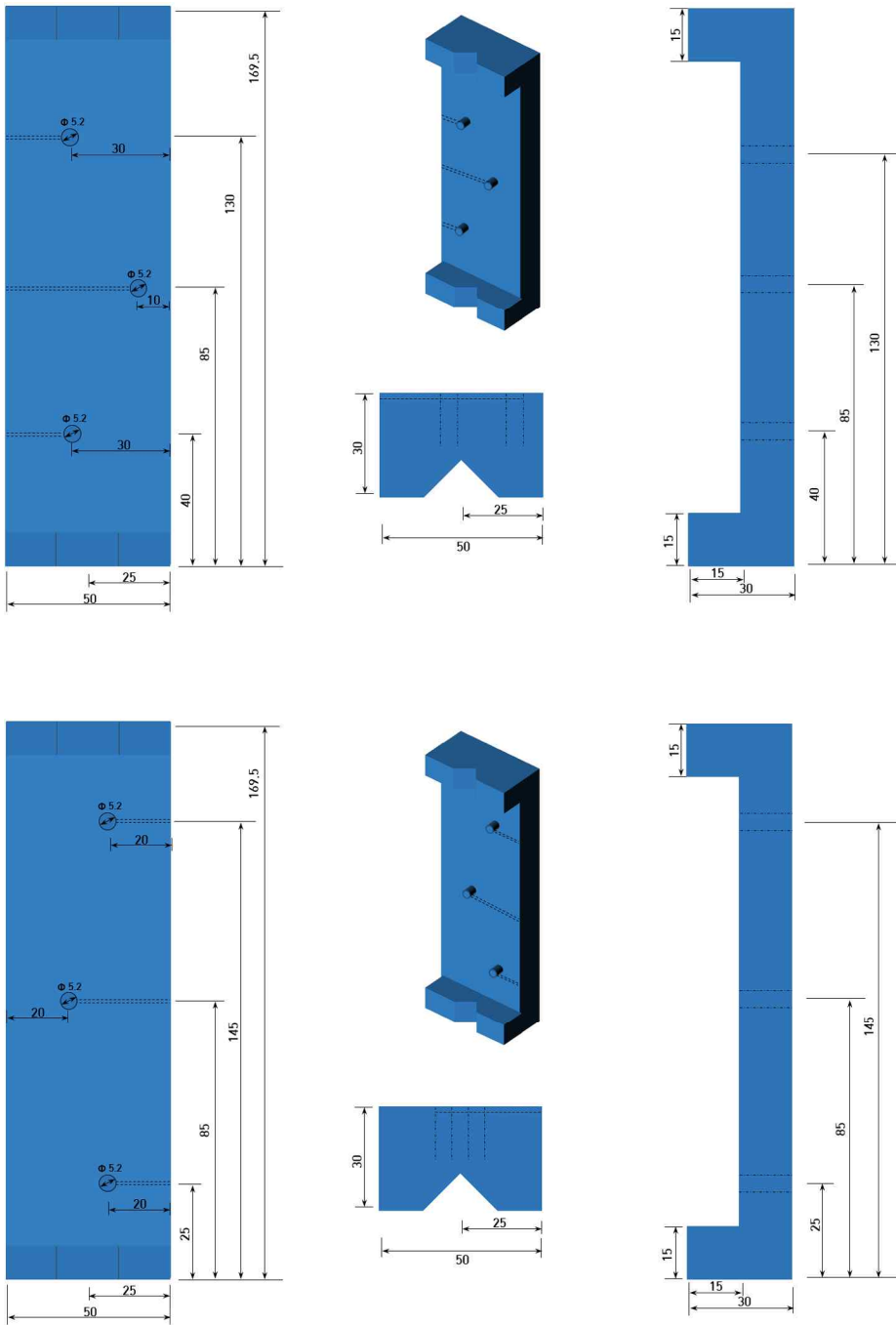


Figure 3.7 Three-view drawings of two sensor holders (mm).

## **AE measurement system settings**

To conduct a successful AE monitoring, certain parameters of the AE measurement system need to be set according to the material being tested. AE data acquisition of the recorded AE waveform depend mainly on the choice of the parameters, such as peak definition time (PDT), hit definition time (HDT) and hit lockout time (HLT) which are classified as system timing parameter. These three parameters are mainly intended to address the interference of reflections. In brief, a proper setting of the PDT ensures correct determination of the time of the true peak of the AE waveform. PDT should be as short as possible. HDT defines the end of the waveform. It must be long enough to span over the time interval which is closely related to the quantity of waveform data. Generally, HDT should be at least twice as long as PDT (PAC, 2007). HLT which starts at the end of the waveform during which the system does not respond to threshold crossing, used to inhibit the interference of the reflections. HLT should be at least 300  $\mu$ /sec for meaningful AE data. (Kolgaonkar, 2005; PAC, 2007) In consideration of the recommended values from PAC (2007) and the experimental material, the timing parameters PDT, HDT and HLT are set as 100  $\mu$ /sec, 200  $\mu$ /sec, and 300  $\mu$ /sec respectively.

The threshold value was used to eliminate the background noise and provide as much information as possible. It was determined by placing the specimen in the loading frame which contact with the load platens and switching on the loading machine.

At this unloading state, no AE signals should be recorded by the AE measurement system. The set-up parameters are summarized in Table 3.6. It should be noted that the AE sensor layout and the set-up parameters for AE measurement system are used in both biaxial compression test and heater test.

Table 3.6 Summary of set-up parameters for AE measurement system.

<b>Parameters</b>		<b>Value</b>	<b>Unit</b>
<b>Threshold</b>		35	dB
<b>Analog filter</b>	Lower	40	kHz
	Upper	1000	kHz
<b>Timing parameters</b>	PDT	100	$\mu$ s
	HDT	200	$\mu$ s
	HLT	300	$\mu$ s
	Max duration	1024	$\mu$ s
<b>Waveform setup</b>	Sample rate	5	MSPS
	Pre-trigger	200	$\mu$ s
	Length	1024	words

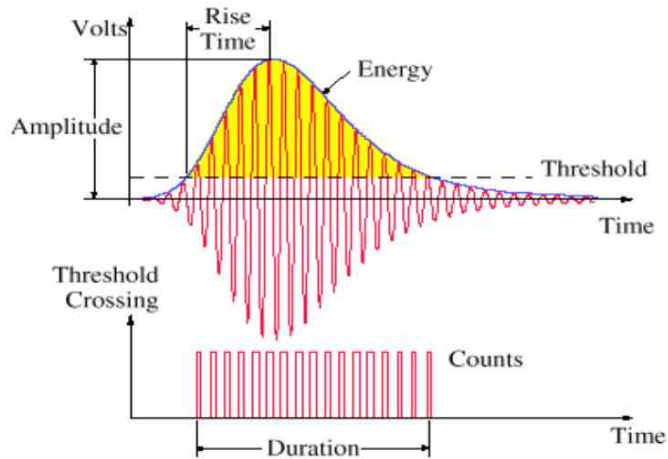


Figure 3.8 Main parameters of AE waveform (Huang et al., 1998).

An idealized AE waveform is shown in Figure 3.8. The detailed explanation of the terminology of the AE waveform parameters can be found in ASTM (2006). AEwin software (PAC, 2011b) was used to record the AE data during test and for data post processing. The software has all the acquisition, graphing and analysis capabilities.

Since the outputs from AEwin will be used for analyses in the following sections, it is necessary to describe what the recorded energy by AEwin signify. It should be noted that AE energy can be measured using two different methods, including MARSE (Measured Area under the Rectified Signal Envelope) method and absolute energy method (PAC, 2007).

In the MARSE method, AE energy (also referred to as PAC-energy) is the measured area (yellow area part) under the rectified signal envelope as shown in Figure 3.8. It is sensitive to amplitude as well as duration.

The MARSE energy is not a true measure of the energy, but a relative value proportional to the true energy. On the other hand, according to PAC (2007), absolute energy is the true energy measure of AE hits and it is derived from the integrals of the squared voltage signal divided by the reference resistance (10kΩ) over the duration of the AE waveform. The absolute energy is expressed in attoJoule (aJ=10<sup>-18</sup>J).

Pollock (2013) indicated the absolute energy is a good feature to deal with larger signals resulting from burst type emissions and defined the absolute energy as shown in equation (3.6).

$$U = \frac{1}{R} \sum_{FTC}^{PDT} V_i^2 \cdot \Delta t \quad (3.6)$$

where R is equal to 10 kΩ representing the input impedance of the preamplifier, FTC stands for “First Threshold Crossing” and PDT stands for “Peak Definition Time”.

Shahidan et al. (2016) pointed out that the shaded area (Figure 3.9) in the AE waveform illustrates the true value of the absolute energy. Shahidan et al. (2013) used absolute energy feature for damage identification and crack detection in concrete materials. Duan et al. (2014) analyzed the AE signal parameters of granite under uniaxial loading and concluded that absolute energy can describe rock damage perfectly. Khazaei et al. (2015) analyzed the damage of intact rocks during uniaxial compression tests using absolute energy feature. It should be noted that the AE energy analysis in the following sections of this research is referred particular to the analysis of absolute AE energy.

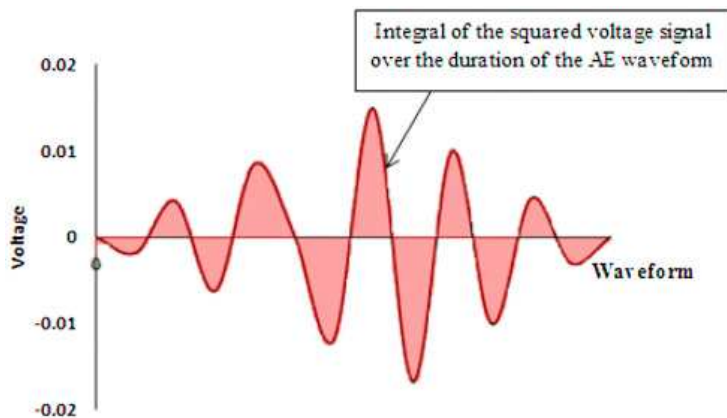


Figure 3.9 Absolute energy features (Shahidan et al., 2016).

## 3.2 Biaxial compression test

### 3.2.1 Experimental set-up and procedure

A schematic view of the test system of biaxial compression test is shown in Figure 3.10. The experimental apparatus is primarily composed of loading system with data acquisition (DAQ) system, hydraulic pump unit and AE monitoring system. The Shimadzu loading machine with a capacity up to 200 ton was used to apply the vertical load. The overall view and close-up view of the experimental set-up of biaxial compression test are shown in Figure 3.11 and Figure 3.12, respectively.

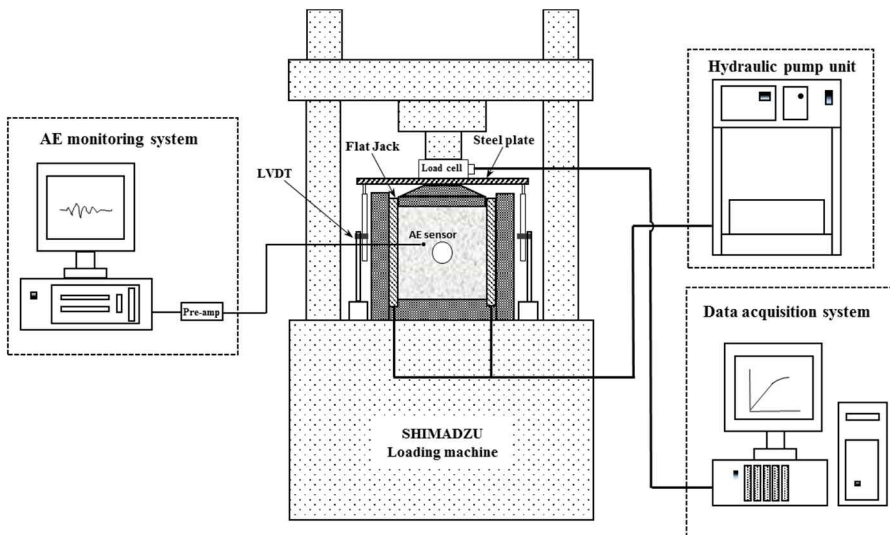


Figure 3.10 Schematic view of the test system of biaxial compression test.

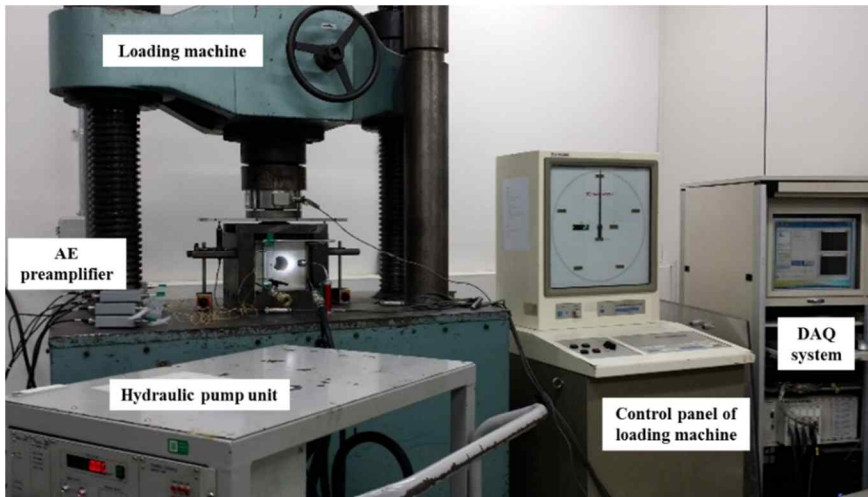


Figure 3.11 Experimental setup of biaxial compression test.

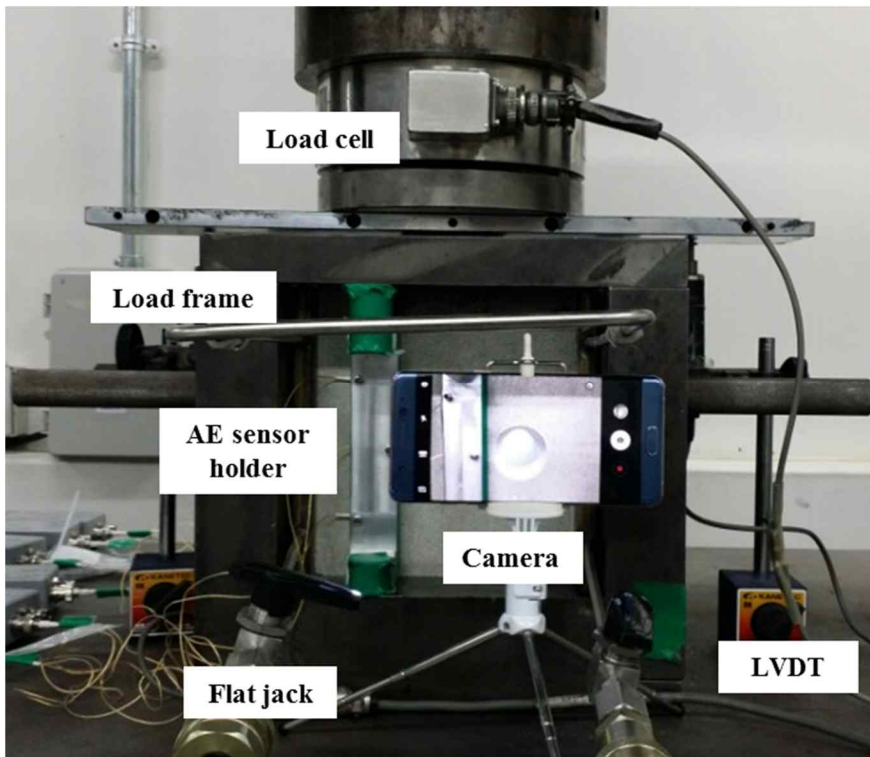


Figure 3.12 Close-up view of experimental setup.

The vertical load was measured using a load cell. In addition, the vertical deformation of the specimen was measured by two linear variable differential transducers (LVDT, CDP-10 type). All these measured data was recorded in the DAQ system. The confining pressure was given by hydraulic pump unit through a pair of flat jacks in horizontal direction.

The loading mode of biaxial compression test is presented in Figure 3.13. The biaxial compression test consisted of two loading phases. Firstly, specimen was loaded by vertical stress ( $\sigma_1$ ) and confining stress ( $\sigma_2$ ) until 5 MPa under hydrostatic loading condition. Then confining stress ( $\sigma_2$ ) was maintained at 5 MPa, vertical stress was monotonically applied until heavy spalling happened and subsequently specimen was unloaded before it reaches the completely failure state for the purpose of maintain the integrity of the specimen which will be used in the following heater test.

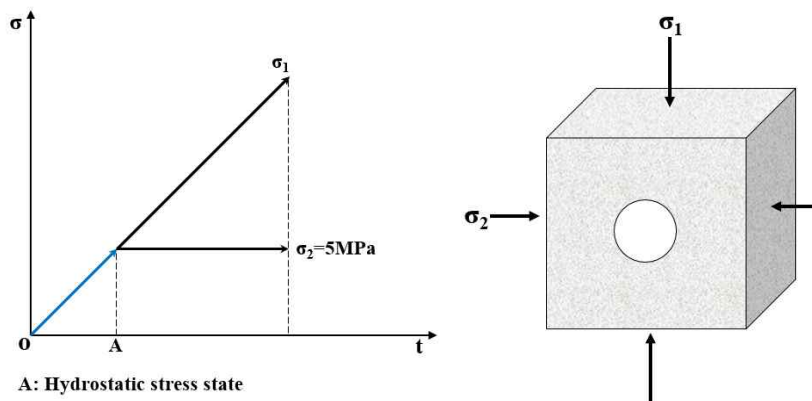


Figure 3.13 Loading mode used in the biaxial compression test.

### 3.2.2 Results of biaxial compression tests

A typical example (#CM-M1) of the brittle failure process around a circular opening under biaxial compression loading condition is shown in Figure 3.14.

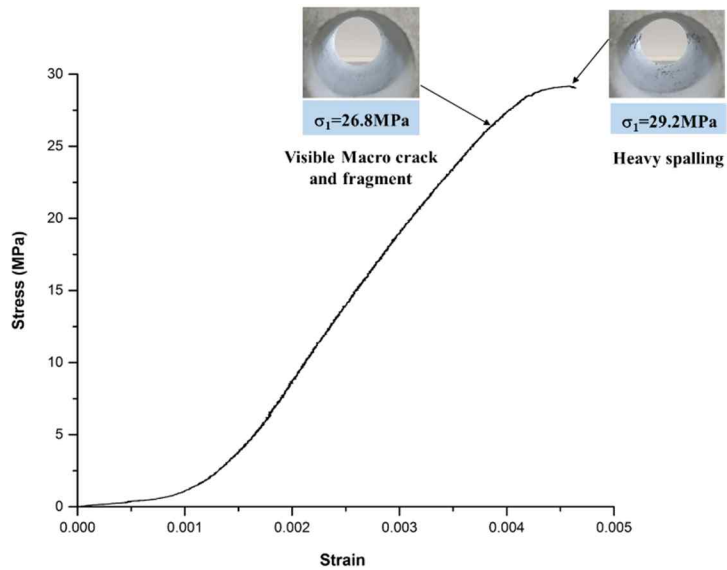


Figure 3.14 Brittle failure process around a circular opening.

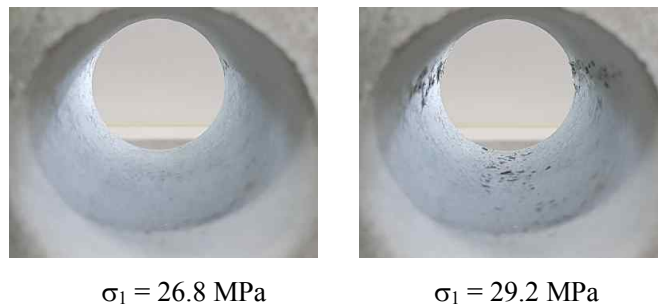


Figure 3.15 Close-up view of the brittle failure.

The macrocracks and fragments were observed when  $\sigma_1$  reached about 26.8 MPa. Then spalling was progressively formed at the sidewall of the opening. Heavy spalling was observed when  $\sigma_1$  approach 29.2 MPa as shown in Figure 3.15. Finally, v-shaped failed zone was formed in the direction of the minor principal stress ( $\sigma_2$ ).

Many attempts have been made to correlate the observed AE activity with the stress level or failure process in rock and rock-like materials. Bae (2005) classified the failure severity around a circular opening into three grades (namely Grade A, Grade B, Grade C) through visual inspection as follows: If no visible cracks was observed, it was inferred as failure Grade A. In failure Grade B, visible macrocracks and fragments start to show up. And when heavy spalling happens, it was defined as failure Grade C. Cheon (2006) applied the method which proposed by Lee and Haimson (1993) to classify the failure grades. In this method, the AE rate was used to determine borehole breakout initiation stress at the point when AE rate severely increased. This method is adopted in this research.

The cumulative AE counts, count rate and stress versus time from biaxial compression test on specimen #CM-M1 were shown in Figure 3.16. The AE counts were gradually increased from the beginning of loading until a drastically rising happens around 27.6MPa ( $\sigma_1/\sigma_c = 0.6$ ).

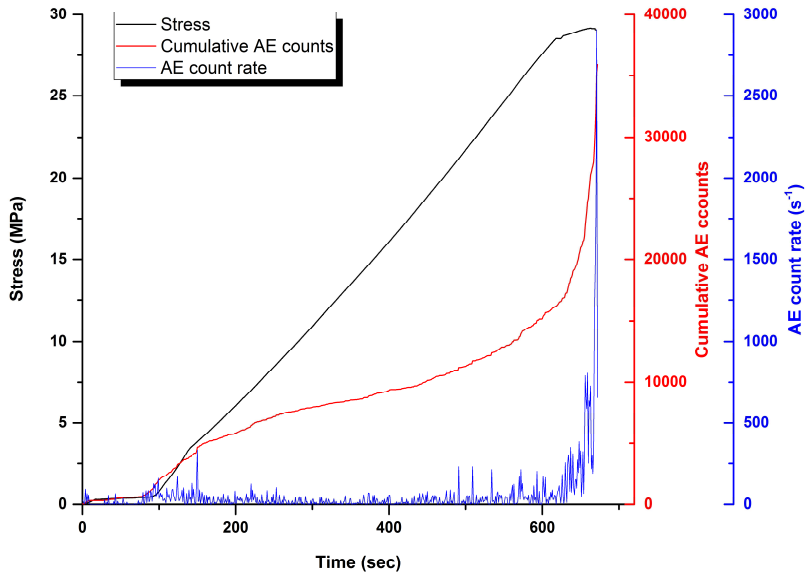


Figure 3.16 Cumulative AE counts and count rate (#CM-M1).

The cumulative absolute energy, energy rate and stress versus time of specimen #CM-M1 were presented in Figure 3.17. At the initial loading period, the energy rate was quite low until vertical stress ( $\sigma_1$ ) close to about 26.6 MPa ( $\sigma_1/\sigma_c=0.58$ ), a big rising of energy rate was distinguishable. From the cumulative absolute energy curve, it can be found a rapid increasing tendency also. Then absolute energy rate rises up significantly when  $\sigma_1$  is around 28.9 MPa ( $\sigma_1/\sigma_c=0.63$ ), the dramatically increases of cumulative energy was also found.

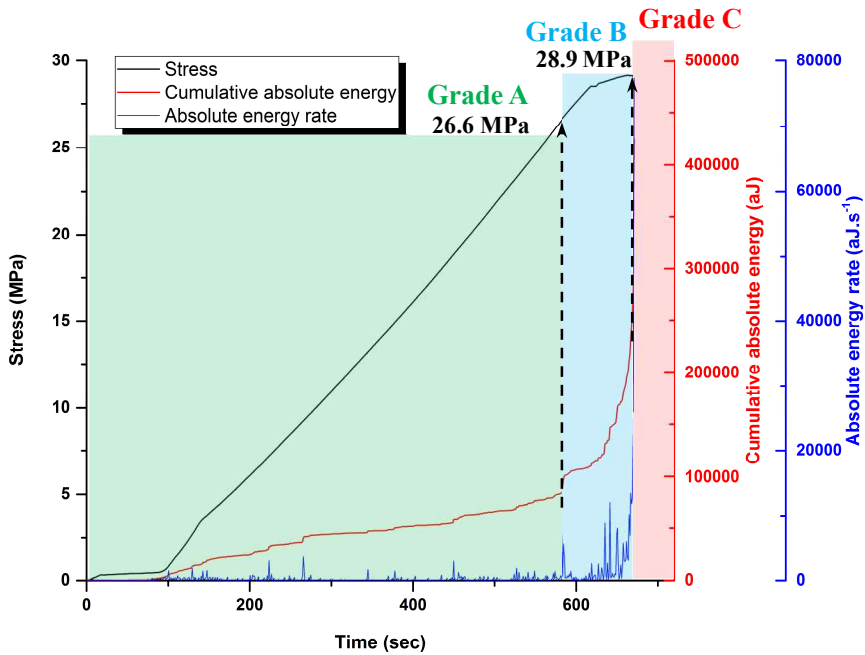


Figure 3.17 Cumulative absolute energy and absolute energy rate (#CM-M1).

By comparing the AE count and AE energy results as shown in Figure 3.16 and Figure 3.17. It was found that the AE counts results gave indefinable information at the initial loading stage and AE count rate also gave ambiguous tendency during the loading process. It is quite difficult to distinguish failure grades based on AE counts results. By contrast, the increasing tendency of absolute energy rate was relatively much more obvious. It is more effective to classify the failure grades by absolute energy results than AE counts results. Zhou et al. (2004) obtained the basic law of the cumulative number of AE events and energy rate through a large number of experiments and proved that

it is more accurate to use the energy rate to determine the stage of deformation and failure of rock.

Keshavarz et al. (2009) compared the absolute energy rate and count rate for prediction of rock failure process and concluded that the absolute energy was more appropriate to monitor crack propagation and to predict the failure of specimen than conventional AE counts.

Therefore, three failure grades (i.e. Grade A, Grade B and Grade C) in the brittle failure process were determined on the basis of the combination of cumulative absolute energy and absolute energy rate results as shown in Figure 3.17 which identified with different color as light green, light blue and light red, respectively. The stress level of visible macro cracks and heavy spalling from four biaxial compression tests are summarized in Table 3.7.

Table 3.7 The stress level of visible macro cracks and heavy spalling from four biaxial compression tests.

<b>Test No.</b>	<b>visible macro cracks</b>		<b>heavy spalling</b>	
	$\sigma_1$ (MPa)	$\sigma_1/\sigma_c$	$\sigma_1$ (MPa)	$\sigma_1/\sigma_c$
#CM-M1	26.6	0.58	28.9	0.63
#CM-M2	25.2	0.55	28.2	0.61
#CM-M3	27.4	0.59	31.2	0.68
#CM-M4	26.3	0.57	27.9	0.60
Ave.	26.4	0.57	29.1	0.63

The three-dimensional view of AE source locations which generated in the biaxial compression test was presented in Figure 3.18. The AE sources are shown in different colors including blue, green, black and red which indicate the sources occurred in different time periods. And the different amplitude of the sources were depicted with different ball size, the higher of source amplitude and the larger of ball size. The projections of AE source locations are displayed in a top view (i.e. projection to the xz-plane) of the specimen as shown in Figure 3.19.

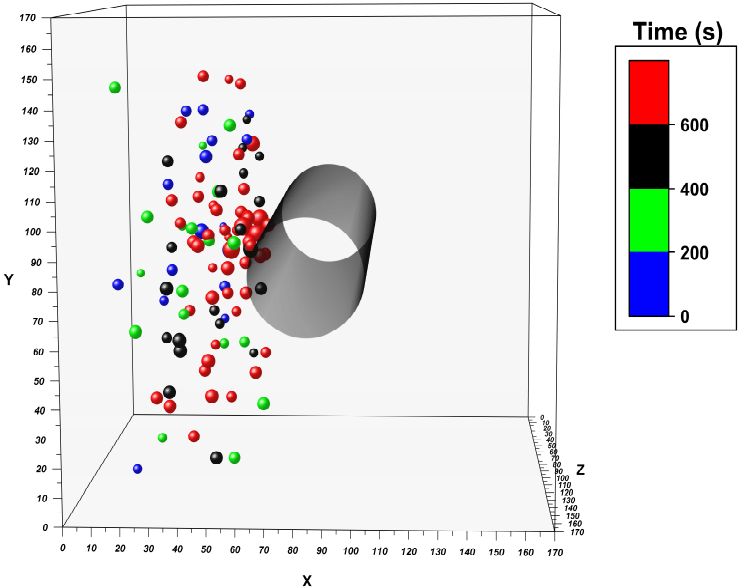
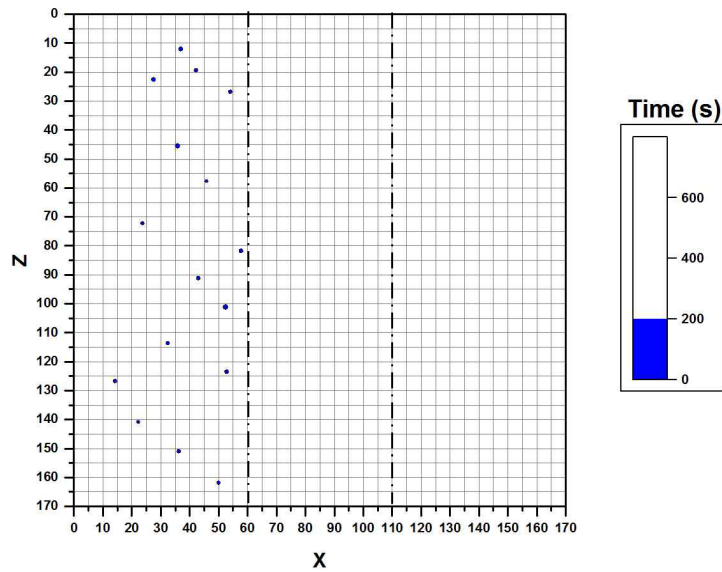


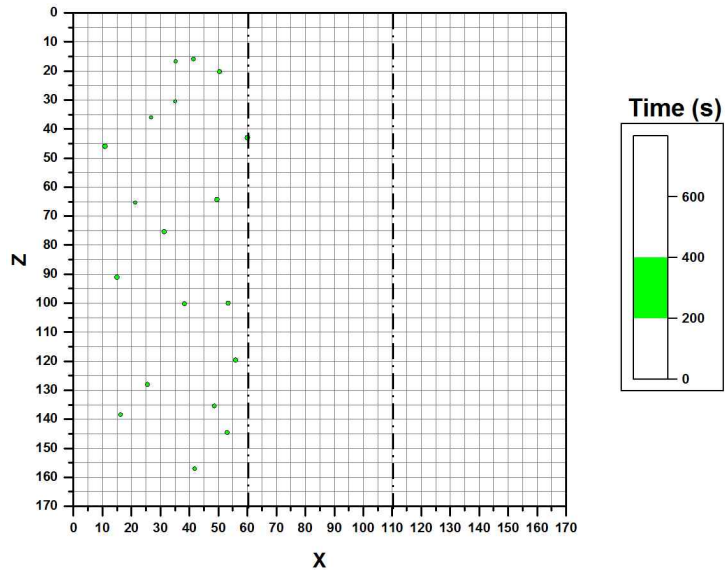
Figure 3.18 AE source locations in three-dimensional view (#CM-M1).

The results were plot with a time interval of 200 second. The AE sources were randomly distributed around the specimen at the first 200 seconds (Figure 3.19 (a)). In the time period from 200 to 600 seconds, the number of AE sources began to increase as shown in Figure 3.19 (b) and (c). When time exceed 600 seconds, it is observed that AE sources getting more concentrated around the sidewall of the circular opening where is the expected failure region (Figure 3.19 (d)). The AE source locations in the whole time period is shown in Figure 3.19 (e).

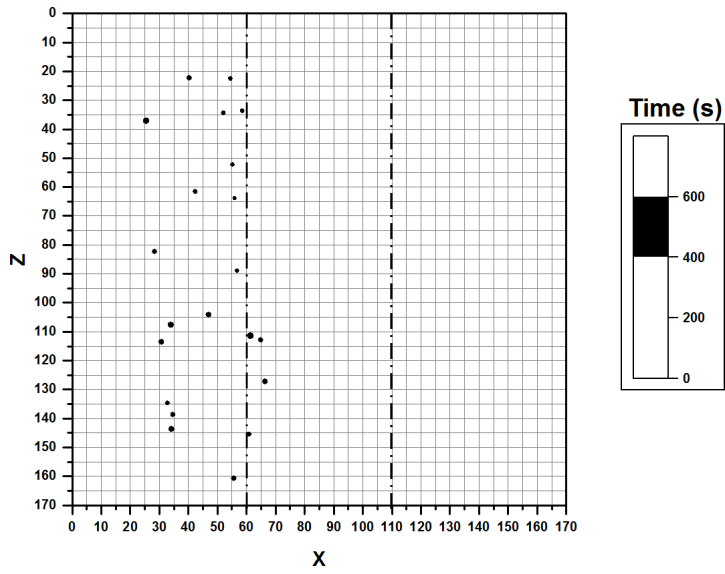


(a) 0~200 seconds

Figure 3.19 Projection of AE sources localizations on xz-plane in each time interval: (a) 0~200 seconds; (b) 200~400 seconds; (c) 400~600 seconds; (d) 600~688 seconds and (e) 0~688 seconds (#CM-M1).

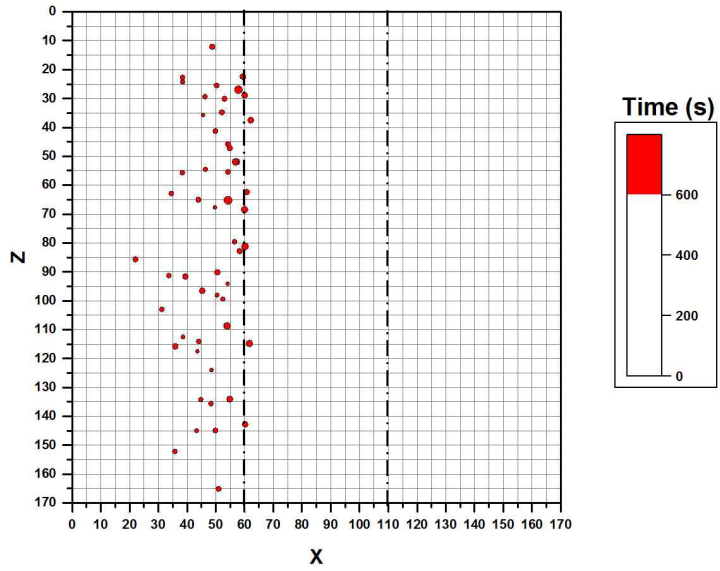


(b) 200~400 seconds

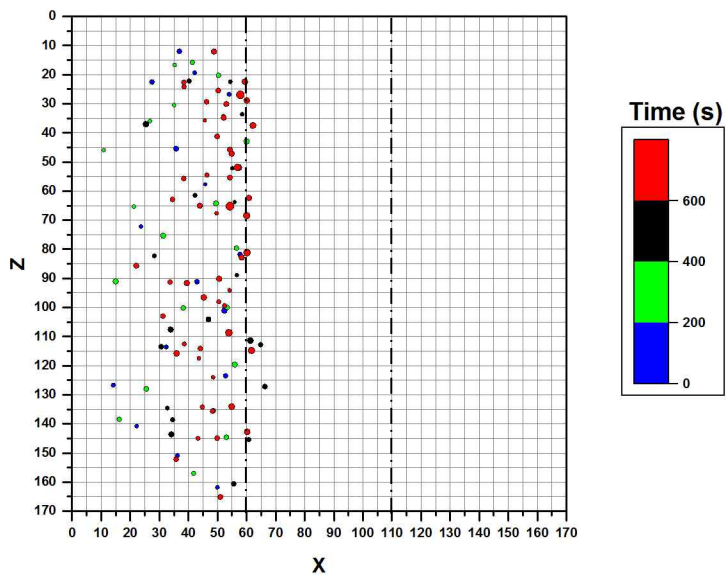


(c) 400~600 seconds

Figure 3.19 continued.



(d) 600~688 seconds



(e) 0~688 seconds

Figure 3.19 continued.

As shown in Figure 3.19, the source location is generally agree with the location of the failed zone around the circular opening. The scatter distribution of the AE sources may be explained by the presence of the preexisting opening in the specimen which causes the reflection of the AE wave. Similar phenomenon were also found in previous studies by Bae (2005); Golshani et al. (2005); Cheon (2006) and Zhao et al. (2014).

### **Characterization of depth and extent of failed zone**

Martin et al. (1999) suggested an empirical linear relationship between depth of failure and the stress magnitude based on case studies from excavated tunnels around the world. The schematic view of a D-shaped tunnel with an effective tunnel radius ( $a$ ) and the depth of failure ( $R_f$ ) is shown in Figure 3.20. The linear relationship between the depth of failure normalized to the tunnel radius ( $R_f/a$ ) and the stress level  $\sigma_{\max}/\sigma_c$  was given in equation (3.7) as:

$$\frac{R_f}{a} = 1.25 \frac{\sigma_{\max}}{\sigma_c} + 0.49(\pm 0.1) \quad (3.7)$$

where  $R_f$  is the depth of failure;  $a$  is the tunnel radius;  $\sigma_c$ : uniaxial compressive strength;  $\sigma_{\max}$  is the maximum tangential stress at the boundary of a circular opening,  $\sigma_{\max} = 3\sigma_1 - \sigma_3$  where  $\sigma_1$  and  $\sigma_3$  are the maximum and minimum principal stresses, respectively.

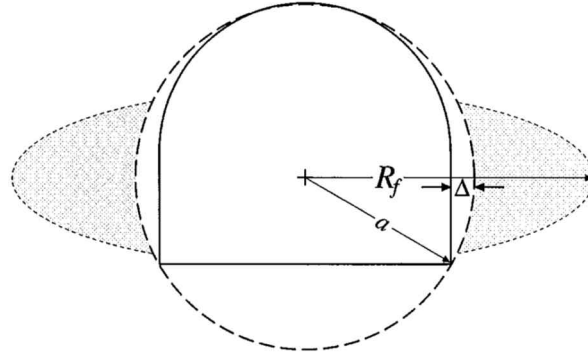


Figure 3.20 Illustration of the D-shaped tunnel with an effective tunnel radius (a) and the depth of failure ( $R_f$ ). (Martin et al., 1999).

For the purpose of measuring the depth and extent of the failed zone, the tested specimen was split into half using splitter after biaxial compression test. The 3D laser profiler (Figure 3.21) was applied to scanning the failed zone with an accuracy of 0.1 mm in all directions (-x, -y, -z). The 3D contour of failed zone of specimen #CM-M1 is shown in Figure 3.22. A cross section view of the 3D contour of failed zone and the calculation method for the depth and extent of the failed zone is shown in Figure 3.23. The depths and extents of the failed zone were measured from ten cross-sections of the tested specimen, the mean values of failure depth and extent were summarized in Table 3.8. We believe the spalling mechanism of laboratory tests and in-situ observations are quite similar. So the general form of this equation can be used in laboratory tests, the correlation between the normalized depth of failed zone and the stress level was achieved and shown in Figure 3.24. A summary of results of four biaxial compression tests are presented in Appendix A.



Figure 3.21 3D laser profiler.

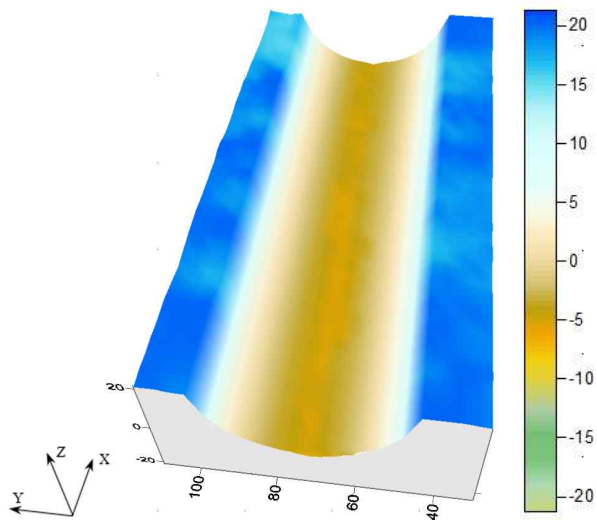


Figure 3.22 3D contour of failed zone (#CM-M1). (Unit: mm)

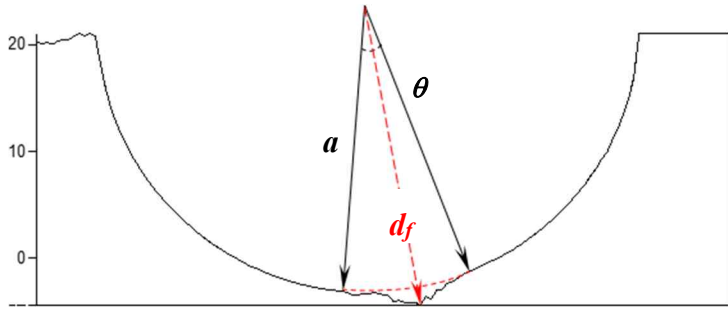


Figure 3.23 Profile of failed zone and calculation method of depth ( $d_f$ ) and extent ( $\theta$ ) of failed zone.

Table 3.8 Depths and extents of failed zone of four tested specimens.

Specimen No.	$\sigma_1$ (MPa)	$\sigma_2$ (MPa)	Failed depth ( $d_f - a$ ) (mm)	Failed extent $\theta$ (°)
CM-M1	28.9	5	2.1	27
CM-M2	28.2	5	2.0	26
CM-M3	31.2	5	2.5	31
CM-M4	27.9	5	2.1	29

A comparison of normalized depth of failed zone and the stress level between laboratory test results including both this research and Cheon (2006) and field observations (Martin, 1999 and Martin, 2005) is shown in Figure 3.25.

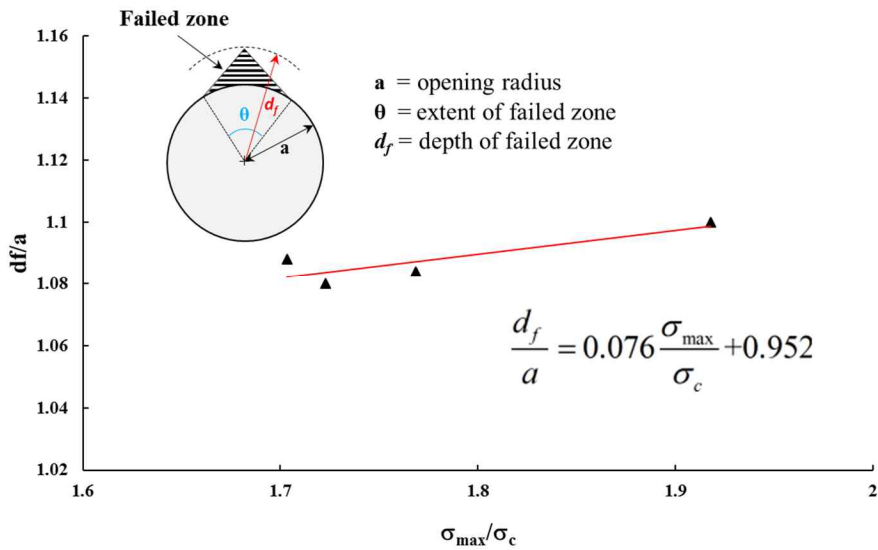


Figure 3.24 Relationship between normalized depth ( $d_f/a$ ) of failed zone and the stress level ( $\sigma_{\max}/\sigma_c$ ) in this research.

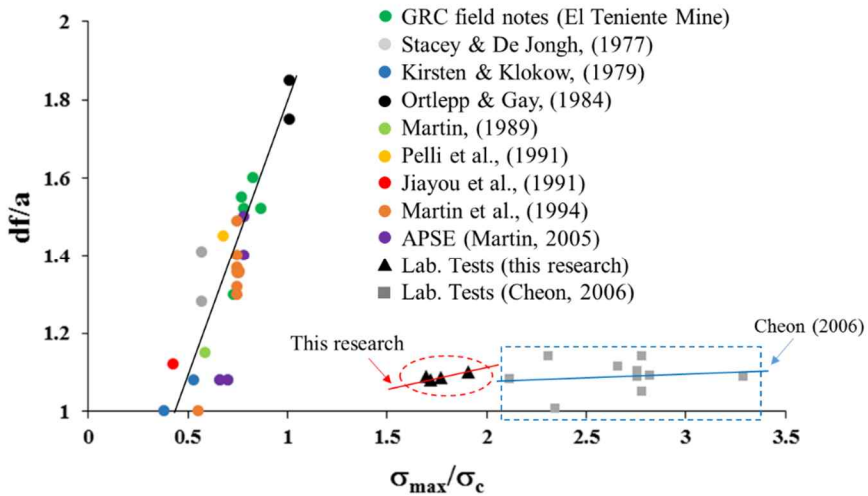


Figure 3.25 Comparison of normalized depth ( $d_f/a$ ) of failed zone and the stress level ( $\sigma_{\max}/\sigma_c$ ) between laboratory test results and field observations (modified from Martin et al., 1999 and Cheon, 2006)

Martin (1997) summarized the previous laboratory test results and showed that as the opening size increases the tangential stress approaches the uniaxial compressive strength of the material, but significant strength-scale effect was observed when openings less than 75 mm in diameter as shown in the Figure 3.26. A noticeable change in the effect of scale was found between the laboratory and in situ results as shown in Figure 3.27.

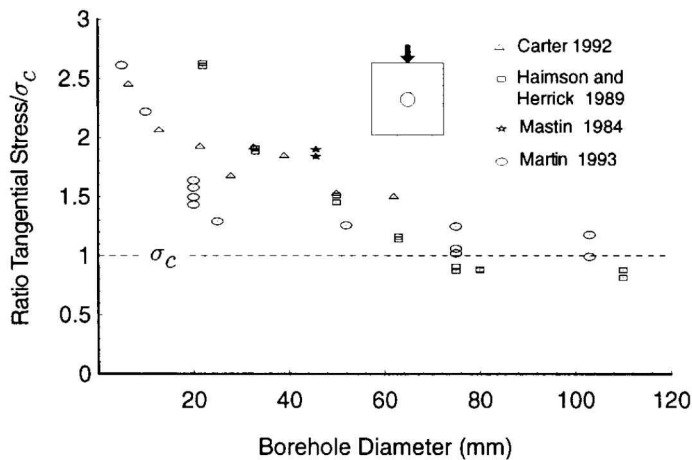


Figure 3.26 Summary of uniaxial testing of blocks containing a circular opening (Martin, 1997).

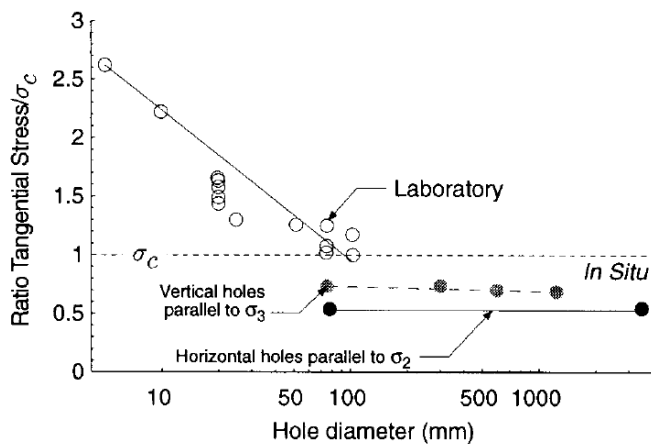


Figure 3.27 Ratio of the calculated tangential stress to  $\sigma_c$  at which breakouts initiate for various borehole diameters (Martin, 1997).

## **3.3 Heater tests**

### **3.3.1 Experimental apparatus and procedure**

The experimental apparatus for heater tests include loading system, AE monitoring system, DAQ system and the heating unit. The first three have been introduced in the biaxial compression tests. The main components of heating unit were made by WATLOW, including a cartridge heater (FIREROD type, 220V, 1000 Watts, Figure 3.28) with an internal k-type thermocouple to provide feedback for temperature control and heating control unit (Figure 3.29) which is composed of a temperature controller (EZ-ZONE PM type) works in combination with a solid state power controller (DIN-A-MITE type) to promote good performance and heater life.

K-type thermocouples (made by JooShin Industrial, Figure 3.30) were used for temperature monitoring in the heater tests, the specifications of thermocouple are listed in Table 3.9.

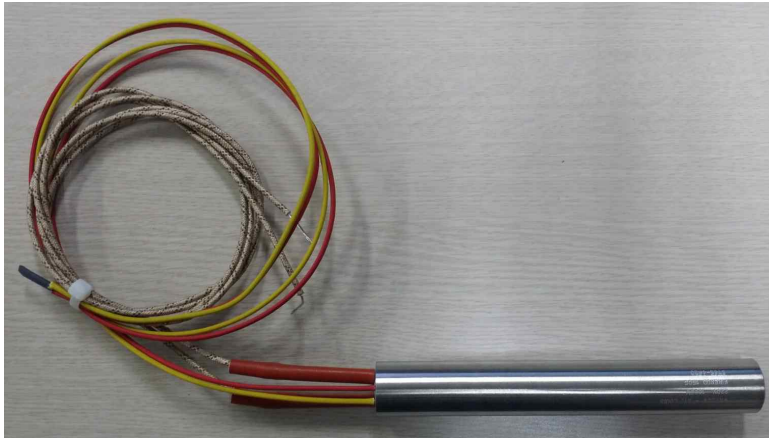


Figure 3.28 Watlow cartridge heater.



Figure 3.29 Heater control unit.

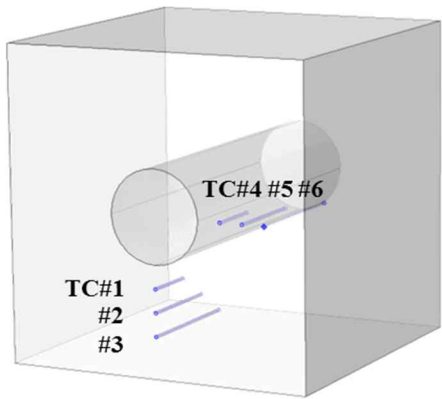


Figure 3.30 K-type thermocouple.

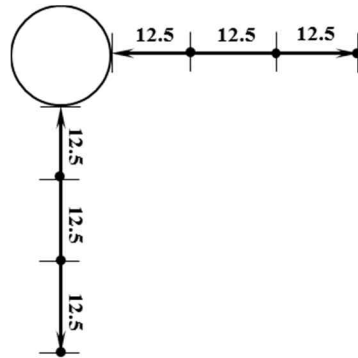
Table 3.9 Specifications of thermocouple.

Model type	Temperature range	Metallic tube	Extensile cable
K type	-200 ~ 1000 °C	L: 100 mm; $\phi$ : 1.8 mm	Thermo-shield wire, 2000 mm

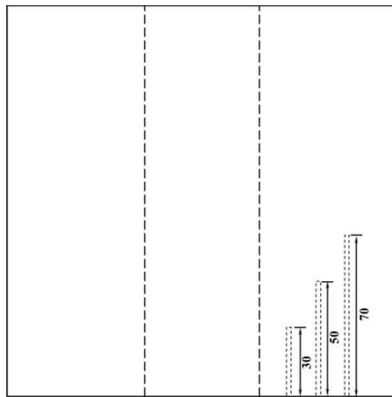
In order to measure the temperature evolution inside the mortar specimen during heater test, six thermocouples were inserted into the holes drilled using long drill bits in the direction parallel to the axis of the center opening. The schematic view of the thermocouple arrangement and the close up view of the thermocouple locations were shown in Figure 3.31.



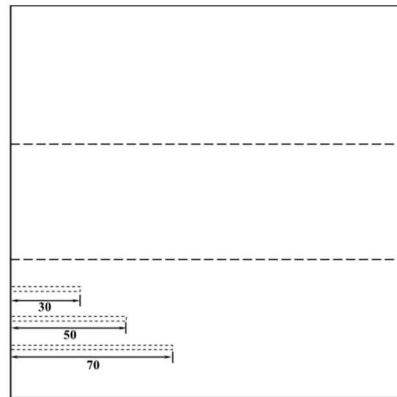
(a) 3D view



(b) close-up view



(c) top view



(d) side view

Figure 3.31 Schematic view of the thermocouple arrangement: (a) 3D view; (b) close-up view; (c) top view; (d) side view.

As shown in Figure 3.31 (a), in vertical direction, thermocouples were numbered as TC#1, TC#2 and TC#3, in horizontal direction, in the same manner, labeled as TC#4, TC#5 and TC#6. The thermocouple were installed at different depths to reduce the influence of each other. In case of TC#1, the measurement point was performed at depth of 30mm, for TC#2 and TC#3, the measuring points were at the depth of 50mm and 70mm, respectively.

Temperature information was recorded in Labview-based DAQ system which is comprised of a temperature module (SCXI-1102), a terminal block (SCXI-1303) and a data acquisition board all made by National Instruments.

Before heater test, holes were drilled on the front surface of the specimen for the installation of six thermocouples. The cartridge heater was placed into the central circular opening and the interfacial gaps between cartridge heater and the opening surface were filled with standard sand. In order to insure the heater was in the center of the opening and to prevent the leakage of the sand, a pair of ceramic rings were used to seal the ends of the opening. The details of the preparation process of heater test are presented in Appendix B. After the installment of thermocouples and AE sensors, the final experimental setup were shown in Figure 3.32 and a close-up view was given in Figure 3.33.

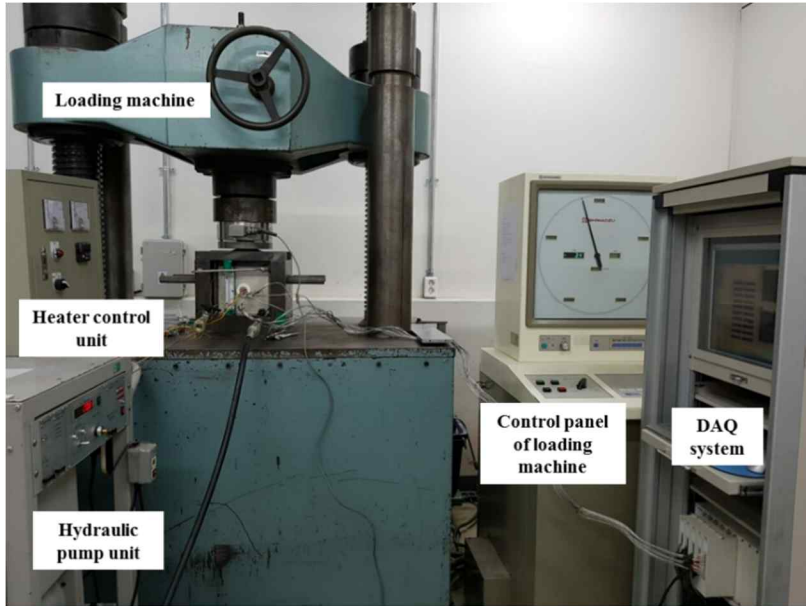


Figure 3.32 Experimental setup of heater test.



Figure 3.33 Close-up view of the experimental setup.

### **3.3.2 Results of heater tests**

#### **Heater test (#CM-TM)**

The heater test was carried out under confined condition. The confining pressure of 1 MPa were applied to the specimen by both loading machine and hydraulic pump simultaneously and kept constant during the heater tests. Then, specimen was heated from 22°C (room temperature) to the 350°C with a heating rate of in manually controlled way and keep at 350°C for two hours. The low heating rate of 3°C/min was applied in order to minimize the transient thermal effects (i.e. thermal shock) as much as possible.

The temperature evolution at six monitoring points (TC#1 ~ TC#6) during heater test (#CM-TM) was presented in Figure 3.34. Through comparison it was found that the temperature evolution of TC#1 was almost the same with TC#4 during the whole heating time, and a similar fashion was also found between TC#2 and TC#5, TC#3 and TC#6.

As the specimen was the intact one (i.e. not damaged), it was reasonable to get these results. The small temperature difference may be due to the monitoring points of thermocouples cannot be exactly at the same depths into the specimen.

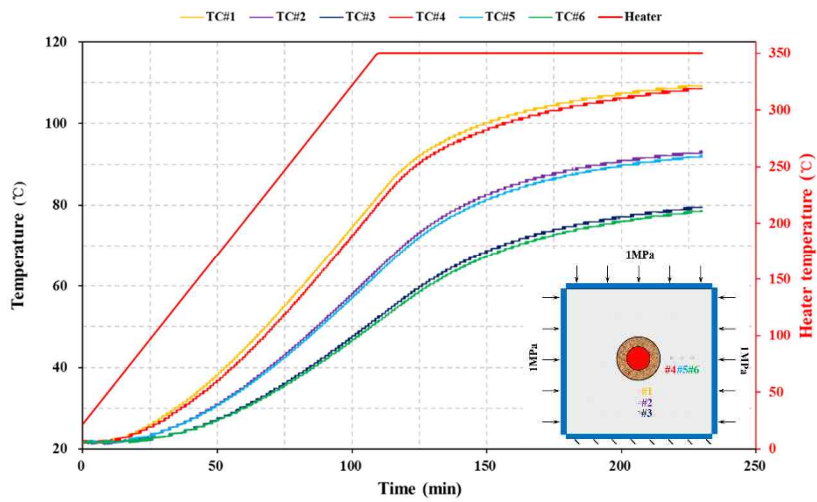


Figure 3.34 Temperature evolution at six temperature monitoring points in heater test (#CM-TM).

The absolute AE energy results are shown in Figure 3.35, heater temperature is also plotted in this figure. The cumulative absolute energy rise up gradually with increasing temperature. No significant rising of absolute energy rate was found in the tests. The AE source locations are shown in Figure 3.36. Different colors indicate the sources occurred in different time periods. The AE source locations are randomly distributed in the specimen and some sources clustered near to the sidewall of the circular opening.

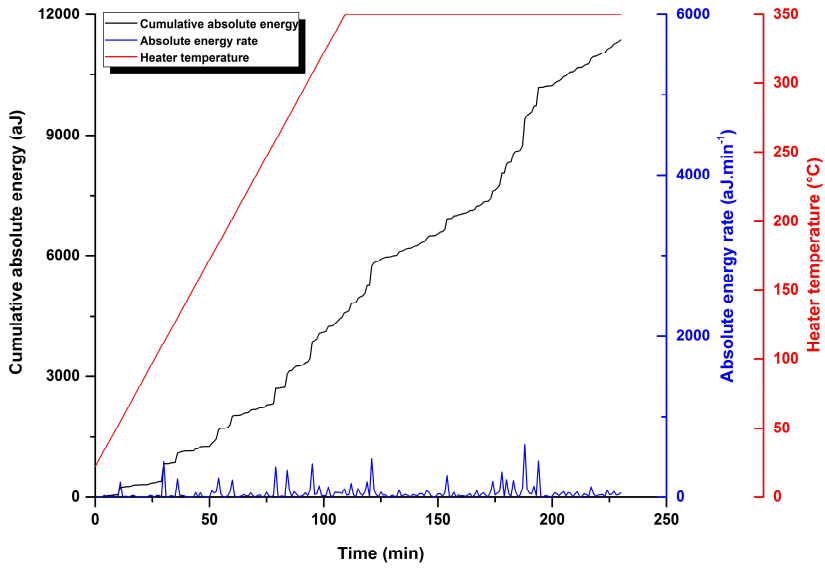


Figure 3.35 Cumulative absolute energy, absolute energy rate and heater temperature in heater test (#CM-TM).

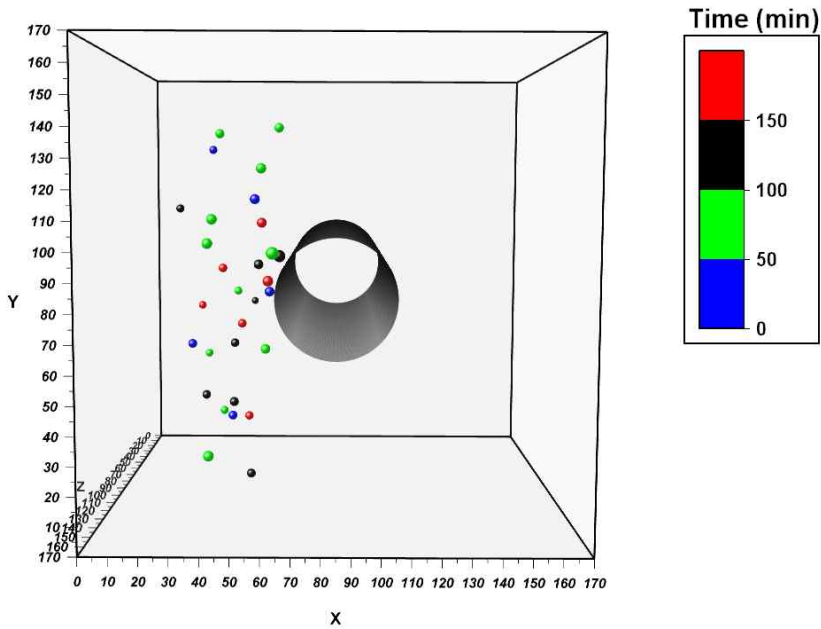


Figure 3.36 AE source locations in heater test (#CM-TM).



Figure 3.37 Close-view of the circular opening after heater test (#CM-TM).

Heater and packing sand were removed after heater test. A close observation of the circular opening is shown in Figure 3.37. No obvious macrocracks were observed on the surface of circular opening. In addition, no macrocracks were found on the outer surface of the specimen. In contrast, when specimen was heated under unconfined condition as found by Carlson et al. (1993), Jansen et al. (1993) and Ishida et al. (2004), macrocrack initiation was observed from the outer surface of the specimen as shown in Figure 1.6.

### **Test results of heater test (# CM-M-TM)**

Heater test #CM-M-TM was carried out in three stages: in the first stage, biaxial compression test was carried out to generate failed zone (spalling zone) at the sidewall the opening. Then specimen was unloaded and moved out. In the second stage, thermocouples and heater were installed, then specimen was placed back into the loading frame. In the third stage, after confining pressure was applied, heater test was started.

After the first stage, specimen was unloaded, generated cracks were closed. Before the heater test, confining pressure was applied to reopen these cracks, but additional mechanical cracking should be minimized during the reloading process when applying confining pressure. So, confining pressure of 1 MPa was applied to reopen the cracks in the pre-damaged area and prevent to make additional mechanical cracking.

The experimental procedure and boundary conditions of heater test #CM-M-TM are the same as heater test #CM-TM. The difference between the two is that the former was carried out using a damaged specimen with pre-existing failed zone at the sidewall of the circular opening which was generated by biaxial compression test, whereas the latter was carried out using intact (undamaged) specimen.

The test results of temperature evolution at six monitoring points are shown in Figure 3.38, with the increase of heater temperature, the temperature difference between TC#1 and TC#4 become more apparent and identical

tendency are also found between TC#2 and TC#5, TC#3 and TC#6. In contrast, there are almost no temperature difference in each pairs of thermocouples in heater test #CM-TM.

The temperature differences between vertical and horizontal direction can be explained by the presence of pre-existing failed zone (Figure 3.40) located at side wall of the circular opening which was generated in biaxial compression test may explain due to the low thermal conductivity of air filled cracks which were formed in this zone during the biaxial compression tests. The variation of recorded absolute energy with time is presented in Figure 3.39. It can be seen that the cumulative absolute energy rise up gradually and a sharp rising of the absolute energy rate was found around 94 minutes. The sharp rising of energy rate maybe proved by the experimental observations.

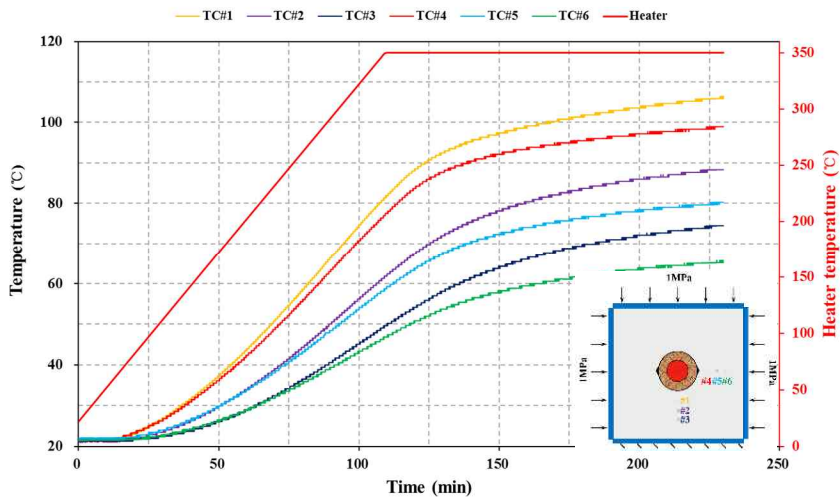


Figure 3.38 Temperature evolution at six monitoring points in heater test (#CM-M-TM).

Fractures were initiated on the surface of the circular opening (Figure 3.40) and some fractures were found to be coalescence with the pre-existing failed zone (Figure 3.41).

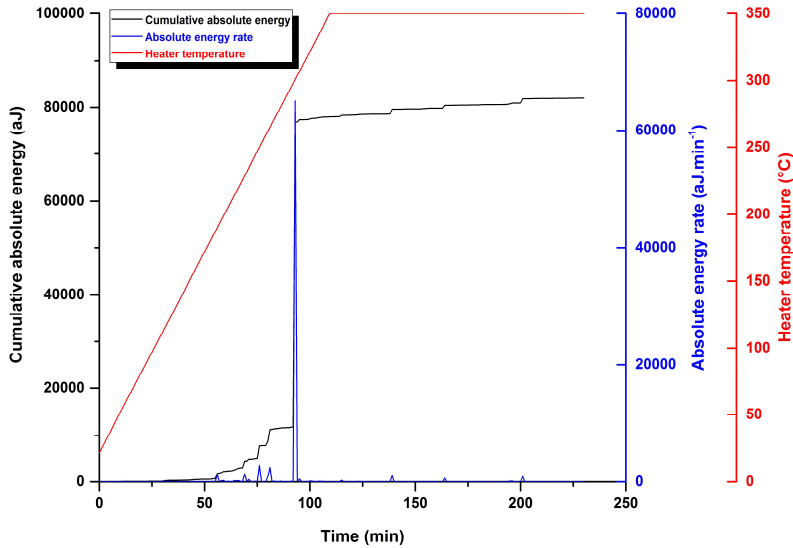


Figure 3.39 Cumulative absolute energy, absolute energy rate and heater temperature in heater test (#CM-M-TM).



Figure 3.40 Fractures were initiated on the surface of the circular opening (#CM-M-TM).

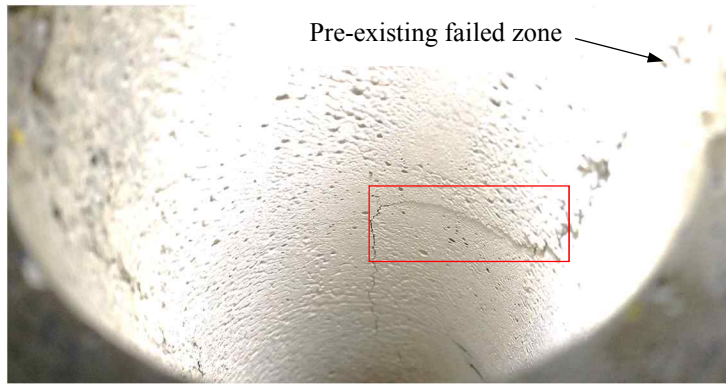


Figure 3.41 Fractures coalescence with the pre-existing failed zone (#CM-M-TM).

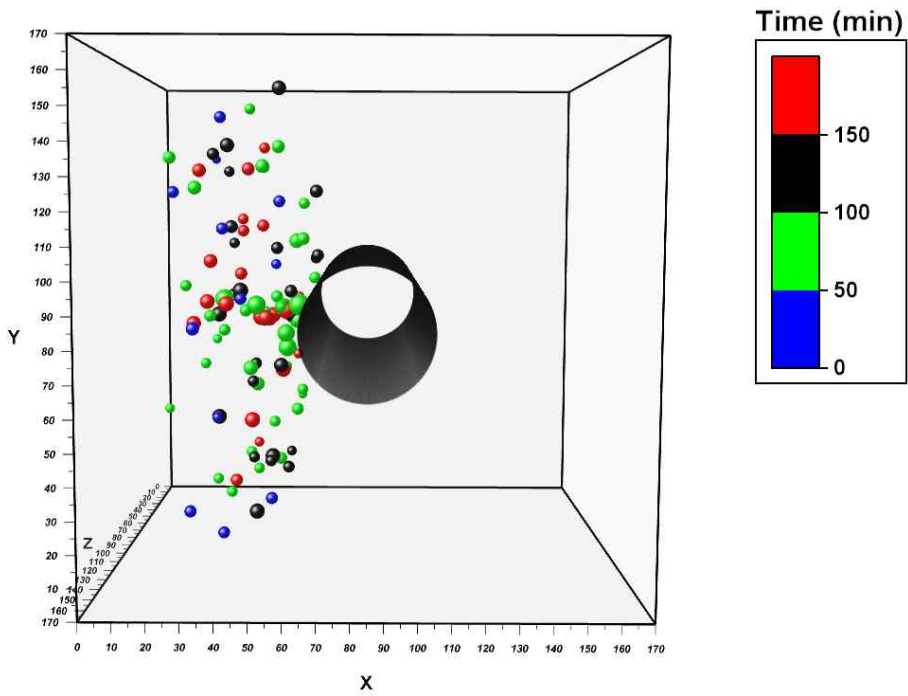


Figure 3.42 AE source locations in heat test (#CM-M-TM).

The result of AE source locations is shown in Figure 3.42. Some sources were clustered close to the sidewall of the circular opening which are relatively comparable to the experimental observations of the heater test, that is, fractures initiated on the surface of the circular opening and some fractures developed and coalescence with the pre-existing failed zone.

The number of AE sensors are very important for improving the effectiveness of AE measurements (Grosse and Ohtsu, 2008). For instance, Carlson et al. (1993) applied 24 AE sensors in their heater test for AE monitoring. Because of the test was under unconfined condition, AE sensors were installed surround the outer surfaces of cylinder rock specimen (Figure 1.6) and relatively better result of AE source locations was achieved.

In contrast, only six AE sensors were used in this research. In addition, heater tests were carried out under confined condition which limited the arrangement of AE sensors, only front and back surface of the specimen are available for the attachment of AE sensors. For these reasons, the results of AE source locations were affected to some extent.

## **4. Numerical simulation**

### **4.1 Numerical model**

#### **4.1.1 Model description**

It is generally believed that the heterogeneity of rock or rock-like material has a great influence on its macroscopic mechanical behaviors (Basista, 2003). Tang (1997) proposed that the non-linear behavior of brittle materials such as rocks and concrete materials during failure process can be simulated with brittle-elastic elements if heterogeneity is considered.

A common way of incorporating heterogeneity into numerical models is through the statistical distribution of material properties. Hudson and Fairhurst (1969) proposed that the strength of rock is not an intrinsic property but the result of a statistical chain reaction, the Weibull distribution (Weibull, 1951) is appropriate for describing the mechanical failure process. Weibull distribution has been widely applied to describe the heterogeneity characteristics by assigning the mechanical properties of rocks and rock-like materials to the elements of the numerical model (Singh and Behrendt, 1994; Tang, 1997; Fang and Harrison, 2002; Feng et al. 2006).

Liang et al. (2008) investigated the heterogeneity and the fracture process of quasi-brittle material by assigning mechanical properties to the numerical specimens following different statistical distribution functions, such as Weibull distribution and Normal distribution using RFPA<sup>3D</sup>. Numerical simulation results were compared with laboratory test results and showed that Weibull distribution is much more reasonable and efficient than other distribution functions. In this research, the formulations of the elastic damage model are based on the approach proposed by Zhu and Tang (2004). This approach has been applied to both laboratory scale and field scale problems for studying the failure process of heterogeneous rock or rock-like materials (Wang et al., 2009; Tang and Tang, 2011).

Some basic assumptions of this approach are listed as follows (Zhu and Tang, 2004):

- 1) Rock or rock-like material is assumed to be composed by mesoscopic elements;
- 2) The heterogeneity of material is considered by assigning the mechanical properties (Young's modulus and strength) to the elements follow Weibull distribution;
- 3) The element is assumed to be isotropic elastic, and the damage evolution of element is assumed to follow elastic damage constitutive law.

## Assignment of mechanical properties

Mechanical properties (Young's modulus or strength) of rock or rock-like material are assigned to the elements of the numerical model following Weibull distribution, as defined by the probability density function (Zhu and Tang, 2004):

$$f(u) = \frac{m}{u_0} \left( \frac{u}{u_0} \right)^{m-1} \exp \left[ - \left( \frac{u}{u_0} \right)^m \right] \quad (4.1)$$

where  $u$  is mechanical property of the element (i.e. Young's modulus and strength);  $u_0$  is related to the mean value of the elements properties;  $m$  defines the shape of the distribution function, it is known as homogeneity index which characterizes the homogeneity of the material. Larger value of  $m$  implies more homogeneous material (Zhu and Tang, 2004; Feng et al., 2006; Li et al., 2009). The typical range of  $m$  is from 2 to 6 for engineering materials (Wong et al., 2006).

## Damage evolution of the element

The elements are assumed to be isotropic elastic. The continuum damage mechanics approach is employed to model the mechanical behavior of the elements. In continuum damage mechanics, a scalar damage variable is defined to describe the change in mechanical behavior of material due to the growth of damage (Lemaitre 1992).

The Young's modulus of elements are assumed to be degraded gradually as damage evolves and the Young's modulus of the damaged element is given as (Zhu and Tang, 2004):

$$E = (1 - D)E_0 \quad (4.2)$$

where  $D$  represents the damage variable,  $E$  and  $E_0$  are the Young's modulus of the damaged and the undamaged elements, respectively. The element and its damage are assumed to be isotropic elastic; so the  $E$ ,  $E_0$  and  $D$  are all scalars. The value of damage variable  $D$  ranges from 0 to 1,  $D$  equals to 0 which correspond to the element under undamaged state. It should be noted that when  $D$  equal to 1, the Young's modulus of the damaged element will become zero, which may lead the operation problem of the finite element analysis, therefore, a small value of  $10^{-5}$  Pa was assigned to the damaged element as the Young's modulus (Zhu and Tang, 2004).

## Damage criterion for the element

When the stress state of element reaches to critical state, damage evolution will be initiated. Both tensile damage and shear damage will be considered in the damage model. Lajtai et al. (1990) suggested that damage initiation was caused by tensile cracking. Cai et al. (1998) based on the observation from the MBE at URL of AECL, addressed the tensile cracking is the dominant fracture mechanism for brittle rocks under compressive loads. Diederichs et al. (2004) analyzed the failure process of brittle rocks and concluded that during compressional loading, tensile cracking will dominate the failure process and the ultimate failure (formation of shear zone) is the result of tensile crack initiation, accumulation and interaction.

Therefore, the maximum tensile stress criterion is applied preferentially to judge whether element is damaged in tensile mode as below (Zhu and Tang, 2004),

$$F_1 \equiv \sigma_1 - f_{t0} \quad (4.3)$$

where  $f_{t0}$  is the uniaxial tensile strength of the element,  $F_1$  is the threshold function for tensile damage.

In case of the element which is not damaged in tensile mode, the shear damage condition will be checked with the Mohr-Coulomb criterion as follows:

$$F_2 \equiv \sigma_1 \frac{1 + \sin \theta}{1 - \sin \theta} - \sigma_3 - f_{c0} \quad (4.4)$$

where  $f_{c0}$  is the uniaxial compressive strength of the element,  $\theta$  is internal frictional angle and  $F_2$  is the threshold function for shear mode damage.

In case the failure criteria as equation (4.3) or (4.4) are satisfied, the damage variable  $D$  can be calculated as follows (Zhu and Wei, 2011):

$$D = \begin{cases} 0 & F_1 < 0 \text{ and } F_2 < 0 \\ 1 - \left| \frac{\varepsilon_{t0}}{\varepsilon_1} \right|^n & F_1 = 0 \text{ and } dF_1 > 0 \\ 1 - \left| \frac{\varepsilon_{c0}}{\varepsilon_3} \right|^n & F_2 = 0 \text{ and } dF_2 > 0 \end{cases} \quad (4.5)$$

where  $\varepsilon_{t0}$  and  $\varepsilon_{c0}$  are the maximum tensile principal strain and the maximum compressive principal strain when tensile or shear damage occurs, respectively;  $\varepsilon_1$  and  $\varepsilon_3$  are the major principal strain and minor principal strain, respectively;  $n$  is a constitutive coefficient and set as 2.0 (Zhu and Tang, 2004).

When  $F_1 < 0$  and  $F_2 < 0$ , there is no damage in the element. When  $F_1 = 0$  and  $dF_1 > 0$ , it means that element was damaged in tensile mode when its stress state satisfies the maximum tensile stress criterion and it is still under loading condition. When  $F_2 = 0$  and  $dF_2 > 0$ , it means that element was damaged in shear mode and it is still under loading condition. Based on equation (4.2) and (4.5) as shown above, the Young's modulus of the damaged element at different stress levels can be calculated.

In this research, the numerical simulations were carried out using finite element code COMSOL Multiphysics® (hereafter referred to as COMSOL). COMSOL is a powerful software for performing multi-physical fields coupling simulation. It provides a flexible platform for interacting with finite element multiphysics models created and has various engineering applications (COMSOL, 2016).

#### **4.1.2 Calibration of numerical model**

Experimental data obtained from the uniaxial compression test was used for this calibration work. The numerical specimen is 100mm in length and 50mm in width. Constant displacement of 0.005 mm/step was applied on the upper surface of the numerical specimen. The input parameters for simulation of uniaxial compression test are listed in Table 4.1.

The comparison of stress-strain curves between simulation and experimental results is plotted in Figure 4.1. The numerical model can generally capture the characteristic of cement mortar as shown in Figure 4.2.

Table 4.1 Input parameters for simulation of uniaxial compression test.

<b>Input parameters</b>	<b>Value</b>	<b>Unit</b>
Homogeneity index, m	5	
Compressive strength, $\sigma_0$	117.5	MPa
Ratio of compressive strength to tensile strength	11.3	
Young's modulus, $E_0$	20.5	GPa
Poisson's ratio, $\nu$	0.28	
Friction angle, $\phi$	31	°
Density, $\rho$	1,950	kg/m <sup>3</sup>

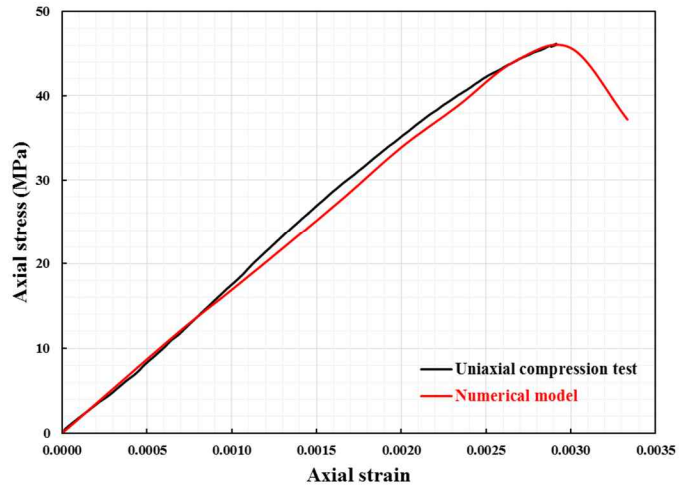


Figure 4.1 Stress-strain curve of cement mortar from uniaxial compression test and numerical simulation.



Figure 4.2 Comparison of damage pattern between test result (left) and simulation result (right) under uniaxial compression test.

## 4.2 Numerical simulation of biaxial compression test

In this section, the elastic damage model is applied to the simulation of biaxial compression test. The schematic view of the numerical specimen and the boundary condition is illustrated in Figure 4.3.

The loading mode in numerical simulation is the same as the biaxial compression test. The numerical specimen was firstly loaded by vertical stress ( $\sigma_1$ ) and confining stress ( $\sigma_2$ ) simultaneously with a loading rate of 0.5 MPa/step until 5 MPa. Then confining stress ( $\sigma_2$ ) was maintained at 5 MPa and the vertical stress ( $\sigma_1$ ) was monotonically applied until 30 MPa. The input parameters used in the simulation are listed in Table 4.1.

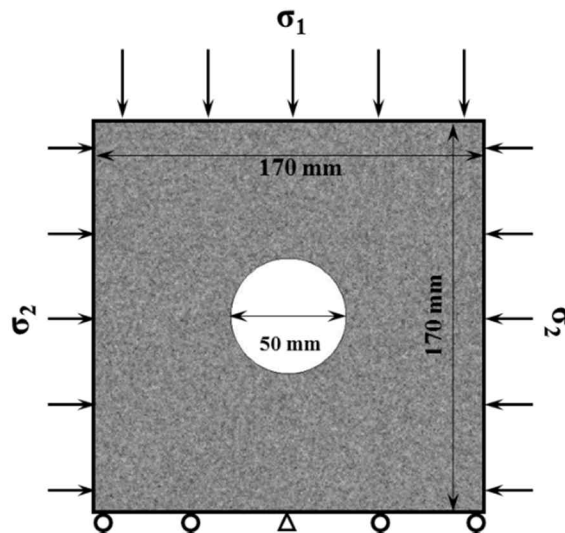


Figure 4.3 Geometry of numerical specimen and boundary condition.

## **Simulation results of biaxial compression tests**

Since the damage of elements is reflected through the degradation of their Young's modulus. Therefore, the distribution of Young's modulus is used to represent the damaged zone around the circular opening under biaxial compression (Figure 4.4). The brightness of gray indicates the magnitude of Young's modulus of the elements. The brighter the gray, the higher value of Young's modulus the element is. Conversely, the darker the gray, the lower value of Young's modulus the element is.

Damage firstly appeared at the roof of the circular opening in response to a predictable tensile stress. Then, damage start to initiate at the sidewall of the circular opening and the damaged zone expanded gradually as the increase of loading as shown in Figure 4.4. It should be noted that the simulated damaged zone is represented by the connected black area around the circular opening. The depth of the damaged zone was evaluated by the mean value of the depth of the black area in each neighboring meshes as shown in Figure 4.5.

The comparison of the depth and extent between the test results and simulation results is shown in Table 4.2. The relatively larger difference between the results can be explained as: in numerical simulation, the results are represented by the damaged zone, but the test results were achieved by measured value of the failure zone.

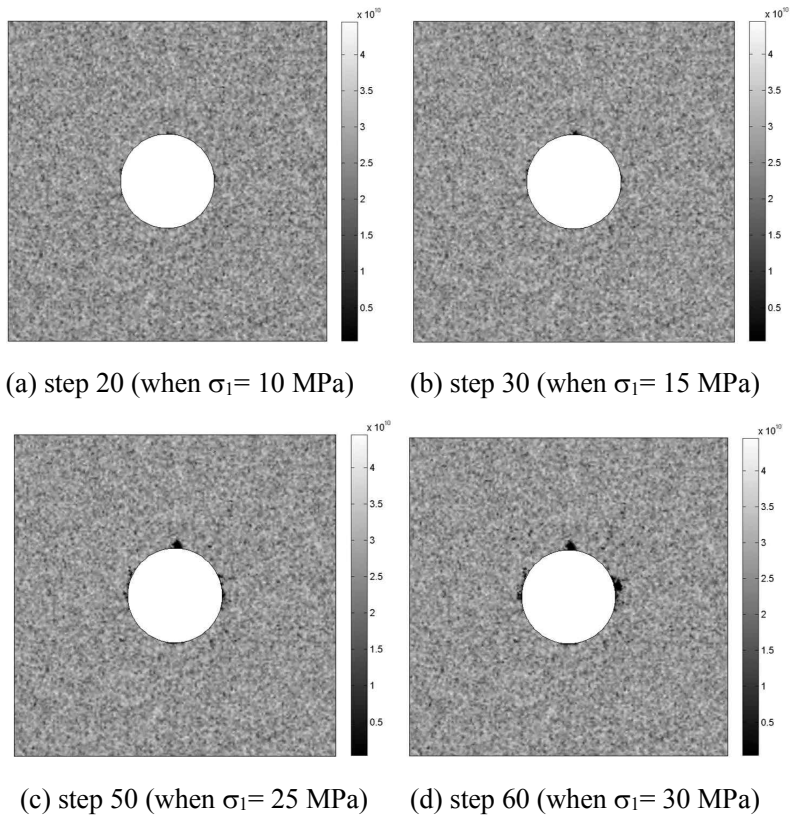


Figure 4.4 Simulation results of the damaged zone (distribution of Young's modulus) around circular opening under biaxial compression loading condition: (a) step 20 (when  $\sigma_1 = 10$  MPa); (b) step 30 (when  $\sigma_1 = 10$  MPa); (c) step 50 (when  $\sigma_1 = 10$  MPa); (d) step 60 (when  $\sigma_1 = 10$  MPa). (Unit: Pa)

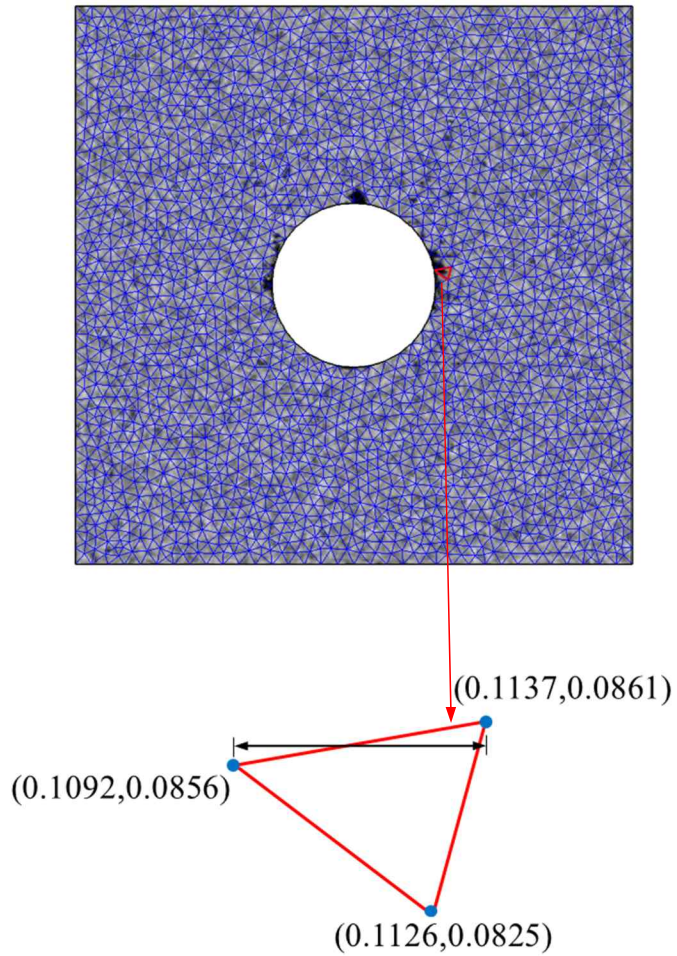


Figure 4.5 Coordinates of the triangular mesh. (Unit: m)

Table 4.2 Comparison of the depth and extent between the test results and simulation results.

	Test result	Simulation result	Difference (%)
Depth (mm)	2.2	2.9	31.8%
Extent (°)	28	36	28.6%

### **4.3 Numerical simulation of heater test**

In most of the numerical simulations that perform coupled thermo-mechanical analysis, thermo-mechanical coupling is assumed to be one-way. Because the conversion of frictional dissipation of mechanical energy into thermal energy is usually ignored. Thus, the thermal analysis provides one-way coupling to mechanical stress calculation through the thermal expansion (Jing and Stephansson, 2007).

The thermal-structural interaction interface in COMSOL has a predefined one-way coupling for the coupled thermo-mechanical problems. It combines a heat transfer module and the structural mechanics module which automatically includes the coupling feature of thermal expansion, the temperature from the heat transfer interface acts as a thermal load in the structural mechanics interface, causing thermal expansion. (COMSOL, 2008)

#### **Thermal-structural interaction governing equations**

The structural mechanics interface is based on solving Navier's equations which embody the stress equilibrium equations, the stress-strain equations and the strain-displacement identities and results such as displacements, stresses, and strains are computed.

The heat transfer interface provides features for modeling heat transfer by conduction, convection, and radiation in solid. The heat transfer in solid is governed by the general equation of heat transfer (COMSOL, 2008):

$$\rho C_p \frac{\partial T}{\partial t} - \nabla \cdot (k \nabla T) = Q + h(T_{\text{inf}} - T) \quad (4.6)$$

where T is temperature (°C),  $\rho$  is density (kg/m<sup>3</sup>),  $C_p$  is specific heat (J/(kg.°C)), k is thermal conductivity (W/(m.°C)), Q is heat source (W/m<sup>3</sup>), h is heat transfer coefficient (W/(m<sup>2</sup>.°C)),  $T_{\text{inf}}$  is ambient temperature,  $h(T_{\text{inf}} - T)$  defines convective heat transfer with the surrounding environment. It should be noted that heat transfer by radiation is not considered in this research.

Solid expand with elevated temperature, which causes thermal strains to develop in the material. The thermal strain ( $\varepsilon_T$ ) combine with the elastic strain ( $\varepsilon_{el}$ ) from mechanical loads to form the total strain:

$$\varepsilon = \varepsilon_{el} + \varepsilon_T \quad (4.7)$$

Thermal strain depends on temperature, T, the reference temperature,  $T_{\text{ref}}$  and the coefficient of thermal expansion,  $\alpha$

$$\varepsilon_T = \alpha(T - T_{\text{ref}}) \quad (4.8)$$

For linear elastic materials, the stress-strain relationship can be described by Hooke's law including the thermal effects as:

$$\sigma = S \varepsilon_{el} = S(\varepsilon - \varepsilon_T) \quad (4.9)$$

where  $\sigma$  is the stress vector,  $\varepsilon$  is the strain vector,  $S$  is the elasticity matrix. More details concerning the governing equations can be found in COMSOL (2008).

### **Thermal properties of cement mortar**

Accurate values of material properties are essential for numerical modeling. In order to determine the thermal properties of cement mortar (i.e. thermal conductivity, specific heat and coefficient of thermal expansion), test samples were made respectively (Figure 4.6). Thermal conductivity and specific heat of cement mortar were measured by laser flash method by LFA 457 (made by Netzsch group) in the temperature range from 20°C to 200°C using samples with the size of 2mm in thickness and 25.4mm in diameter. Interpolation functions can be used to describe material properties that are defined by values at discrete points in COMSOL. The temperature dependent thermal conductivity and specific heat of mortar are input to interpolation functions and plot in Figure 4.8 (a) and Figure 4.8 (b).

These temperature dependent properties are used in the numerical simulation of heater tests. The coefficient of thermal expansion was measured by TMA2940 thermomechanical analyzer (made by Mettler Toledo) using 5mm cubic samples as shown in Figure 4.7. Based on the test results, the coefficient of thermal expansion has no evidently changed in the temperature range of 25°C to 150°C (Figure 4.8 (c)), therefore a constant value of  $6.95 \times 10^{-6}/^{\circ}\text{C}$  was used in this research.



Figure 4.6 Test samples for thermal conductivity and specific heat measurements.

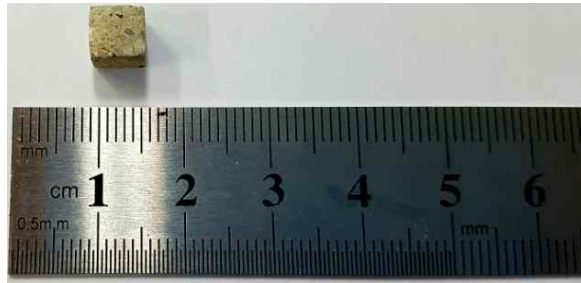
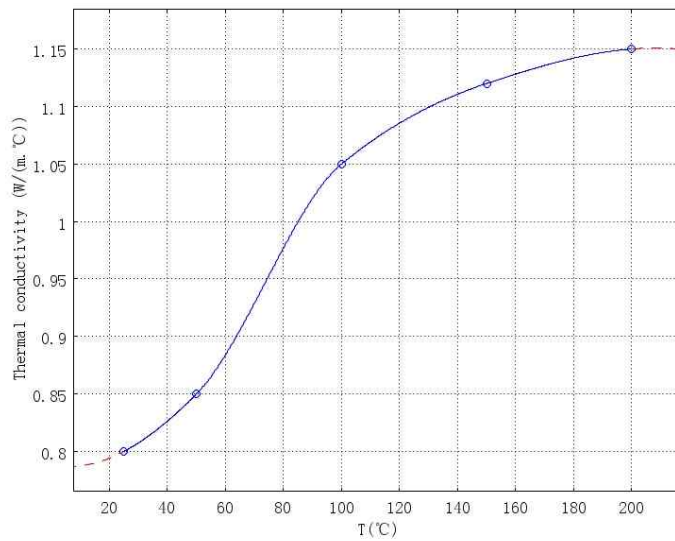
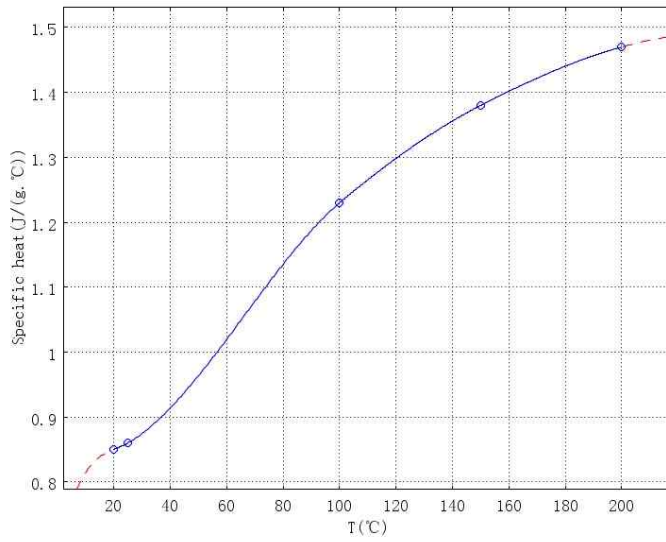


Figure 4.7 Test specimen for coefficient of thermal expansion measurement.

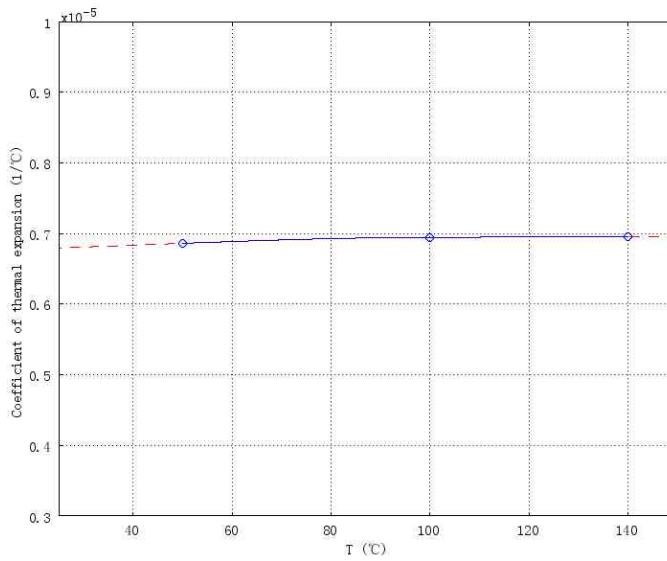


(a) thermal conductivity

Figure 4.8 Thermal conductivity and specific heat of cement mortar: (a) thermal conductivity; (b) specific heat; (c) coefficient of thermal expansion.



(b) specific heat



(c) coefficient of thermal expansion

Figure 4.8 continued.

## **Thermal conductivity variation of the element with damage**

Pribnow et al. (1996) measured the thermal conductivities of rocks under elevated temperatures and mentioned that the cracks are filled with air which causing a decrease of thermal conductivity in the dry samples. Perkowski (2008) found a decrease of thermal conductivity due to brittle damage evolution in concrete specimens which subjected to mechanical compression loading. Lee (2012) investigated the thermal properties of rock samples to estimate the extent of EDZ and found the thermal conductivity in the EDZ was decreased by about 20%.

Exponential function has been widely used to describe the damage evolution of rock properties (Liu et al., 2010; Peng et al., 2015). Picandet et al. (2001) and Zhu and Wei (2011) used exponential function to describe the influence of damage on permeability in concrete and rock material. Chang and Chang (2009) applied exponential function to describe the spatially and temperature-dependent thermal conductivity. Xu et al. (2016) described the relationship between thermal conductivity and the apparent density of concrete with an exponential function.

In this simulation, the variation of thermal conductivity resulting from the damage evolution of the element is assumed following the exponential function as:

$$\lambda = \lambda_0 \exp(-\alpha D) \quad (4.10)$$

where  $\lambda_0$  denotes the thermal conductivity of the undamaged element and  $D$  is damage variable defining the current damage level of the element,  $\alpha$  is a coefficient to reflect the effect of damage on the thermal conductivity and set as 0.75 in this simulation. In order to simulate heater tests, the temperature history at the surface of the circular opening ( $T_a$ ) should be decided firstly as shown in Figure 4.9. It was back calculated based on the temperature data recorded by thermocouples in heater test #CM-TM.

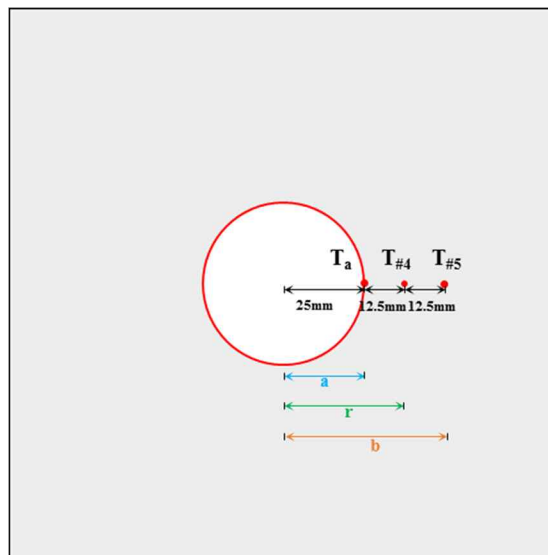


Figure 4.9 Schematic view of the method for calculating the temperature at the surface of the circular opening (#CM-TM).

The analytical solution of the classical steady state thermoelastic problem in a homogeneous isotropic hollow cylinder (Figure 4.10) subjected to thermal loads was used in this calculation.

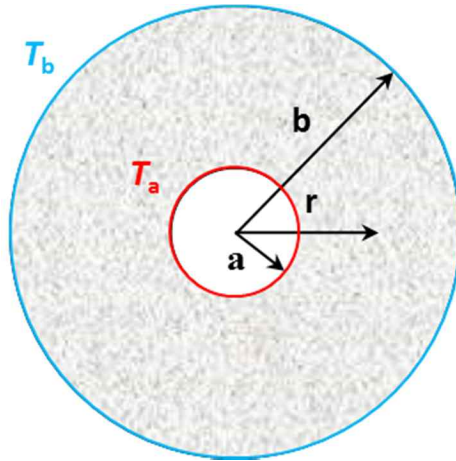


Figure 4.10 Schematic view of hollow cylinder

The temperature distributions under specific temperature gradient is given as follows (Xu, 2006):

$$T_r = T_a \frac{\ln(b/r)}{\ln(b/a)} + T_b \frac{\ln(a/r)}{\ln(a/b)} \quad (4.11)$$

where  $r$  is radial distance from the cylinder center,  $a$  is inner radius of the cylinder,  $b$  is outer radius of the cylinder,  $T_a$  is temperature at the inner surface,  $T_b$  is temperature at the outer surface.

As shown in Figure 3.34, the recorded temperature evolution curve of TC#4 and TC#5 in heater test #CM-TM are almost the same with TC#1 and TC#2 , as discussed in section 4.3.1. Thus, TC#4 and TC#5 are used in this calculation. When  $a=25\text{mm}$ ,  $r=37.5\text{mm}$ ,  $b=50\text{mm}$ ,  $T_r=T_{\#4}$  and  $T_b=T_{\#5}$ ,  $T_a$  can be calculated as follows:

$$T_a = \left[ T_{\#4} - T_{\#5} \frac{\ln(a/r)}{\ln(a/b)} \right] \times \frac{\ln(b/a)}{\ln(b/r)} \quad (4.12)$$

The calculated temperature evolution curve at the surface of the circular opening ( $T_a$ ) is shown in Figure 4.11.

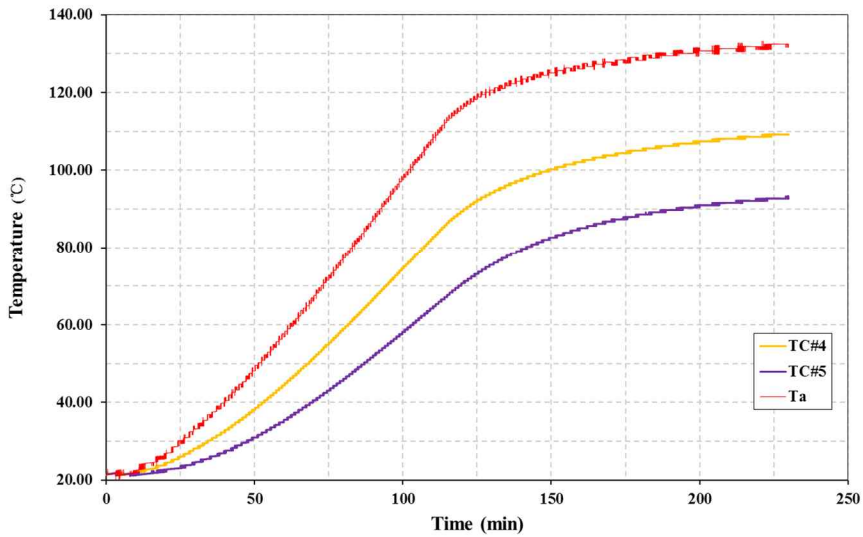


Figure 4.11 The calculated temperature evolution curve at the surface of the circular opening (#CM-TM).

## Numerical simulation of heater test # CM-TM

The schematic view of test condition of heater test # CM-TM is shown in Figure 4.12. The boundary conditions for simulation of heater test (#CM-TM) are as follows: lower boundary of the numerical specimen is fixed and other boundaries were applied with confining pressure of 1MPa. The room temperature is constant at 22 °C. The convective heat transfer is considered and the convective heat transfer coefficient of air is assumed as 13 W/(m<sup>2</sup>·°C) (<http://www.engineeringtoolbox.com>). The surface temperature of the circular opening was applied according to temperature evolution curve of T<sub>a</sub> as shown in Figure 4.11 and the time step is set as 1 min/step. The input parameters for the simulation of heater tests are listed in Table 4.3.

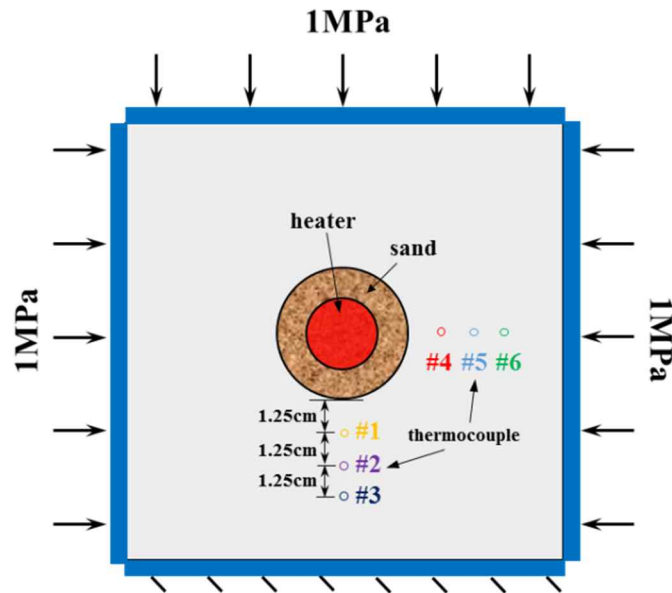


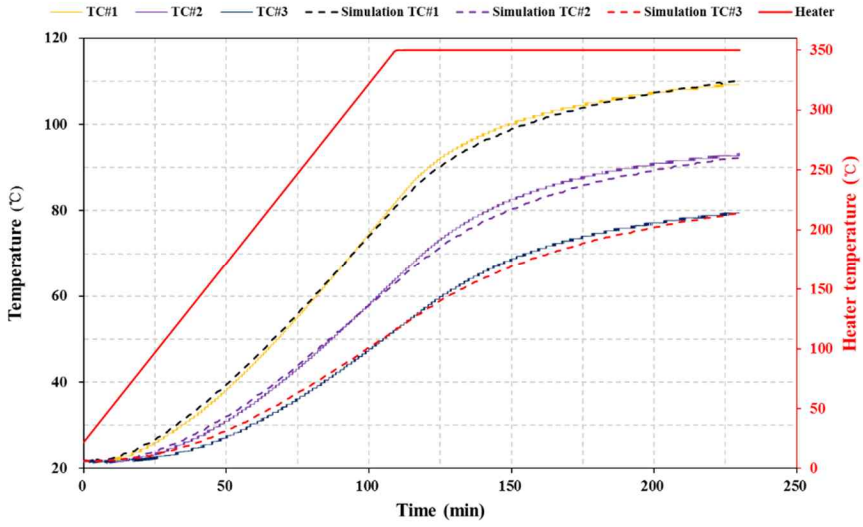
Figure 4.12 Schematic view of test condition of heater test (#CM-TM).

Table 4.3 Input parameters for simulation of heater test.

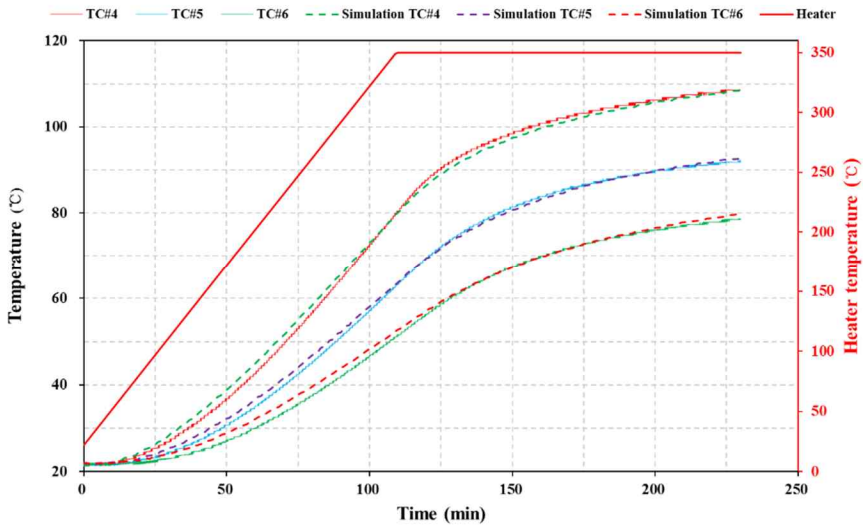
<b>Input parameters</b>	<b>Value</b>	<b>Unit</b>
Homogeneity index, m	5	-
Compressive strength, $\sigma_0$	117.5	MPa
Ratio of compressive strength to tensile strength	11.3	-
Young's modulus, $E_0$	20.5	GPa
Poisson's ratio, $\nu$	0.28	-
Friction angle, $\phi$	31	°
Density, $\rho$	1,950	kg/m <sup>3</sup>
Heat transfer coefficient	13	W/m <sup>2</sup> ·°C
Room temperature	22	°C

### **Simulation results heater test # CM-TM**

The comparison of simulation results and test results of temperature evolution at six monitoring points is shown in Figure 4.13. The simulation results (dashed line) of temperature evolution are generally agreed well with the tests results (solid line). The discrepancy may due to the two dimensional simplified boundary conditions used in the simulation.



(a) TC#1, TC#2, TC#3



(b) TC#4, TC#5, TC#6

Figure 4.13 Comparison of simulation results and test results at different temperature monitoring points: (a) TC#1, TC#2, TC#3; (b) TC#4, TC#5, TC#6 (#CM-TM).

The damaged zone (distribution of Young's modulus) around the circular opening is shown in Figure 4.14. Quite limited damage was found around the circular opening which is consistent with experimental results of heater test #CM-TM where no visible macrocracks were observed on the surface of the circular opening (Figure 3.36).

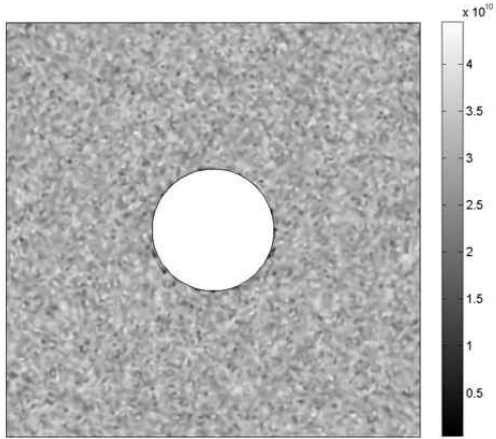


Figure 4.14 Simulated damaged zone around the circular opening. (Unit: Pa)

## Numerical simulation of heater test # CM-M-TM

The schematic view of the test condition of heater test #CM-M-TM is shown Figure 4.15. The temperature at the surface of the circular opening (i.e.  $T_a$ ) was calculated based on the temperature data recorded by thermocouples  $T_{\#1}$  and  $T_{\#2}$  in heater test #CM-M-TM as shown in Figure 4.16. Because the depth of failed zone was small (about 2 mm) as shown in Table 3.8 and the difference of thermal conductivity between cement mortar and dry sand (0.15 ~ 0.25 W/(m·°C)) was much lower than the difference between cement mortar and air (0.024 W/(m·°C)) (<http://www.engineeringtoolbox.com>), we assumed that the temperature on the circular boundary is all the same.

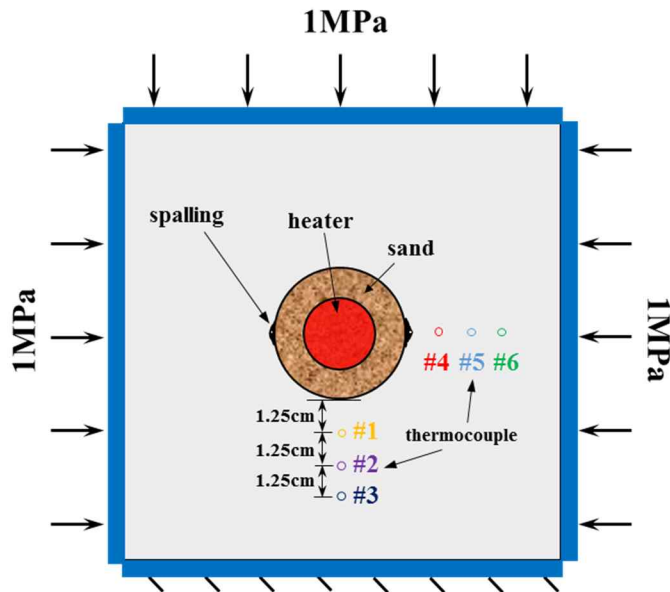


Figure 4.15 Schematic view of the test condition of heater test (#CM-M-TM).

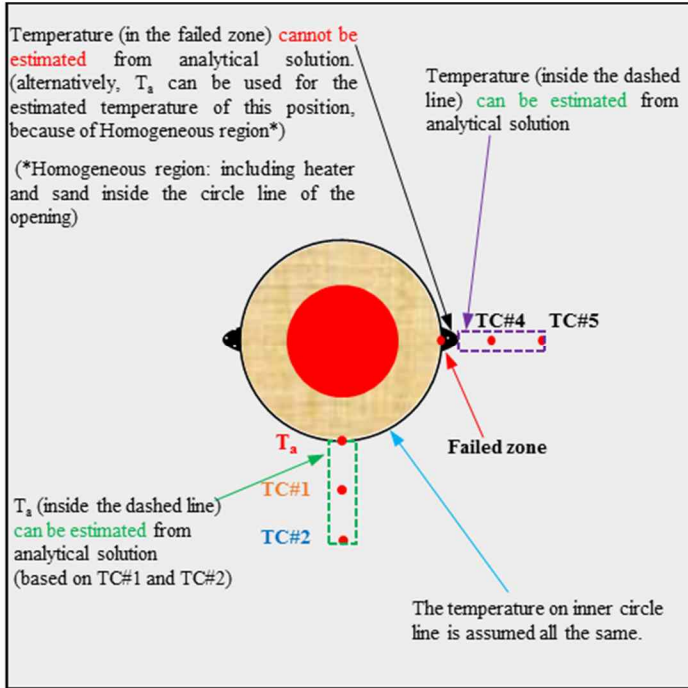


Figure 4.16 Schematic view of the method for calculating the temperature at the surface of the circular opening (#CM-M-TM).

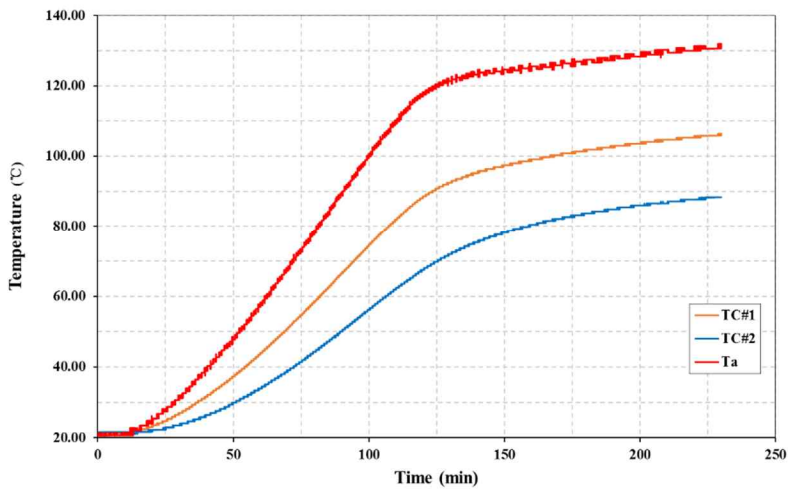
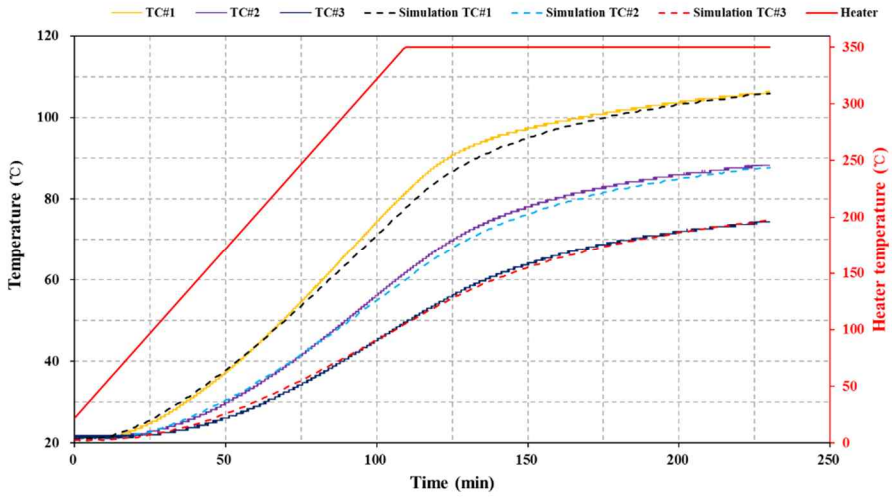


Figure 4.17 The calculated temperature evolution curve at the surface of the circular opening ( $T_a$ ).

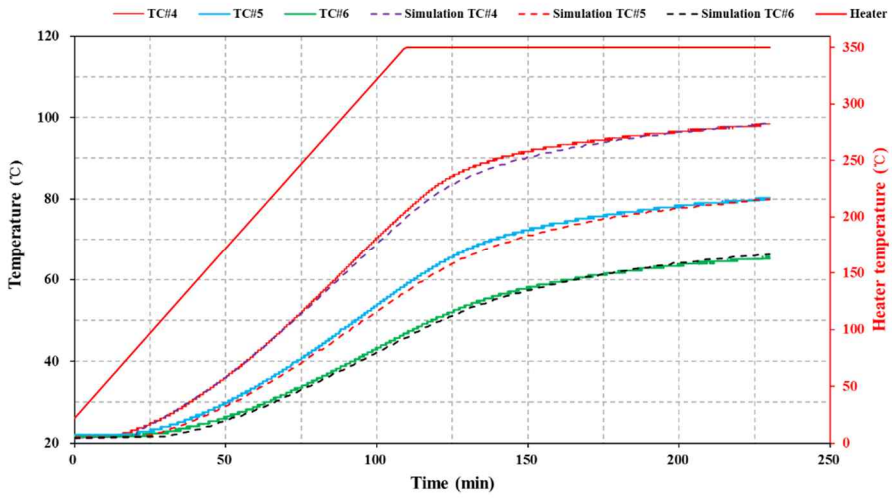
The calculated temperature evolution curve at the surface of the circular opening ( $T_a$ ) is shown in Figure 4.17. The numerical simulation for CM-M-TM was implemented in two steps: Firstly, simulation of biaxial compression test was carried out; then, heater test was simulated. The boundary condition for the first step are the same with the simulation of biaxial compression test as shown in Figure 4.3 which has been introduced in section 4.2. For the second step (i.e. simulation of heater test), the calculated temperature evolution curve of  $T_a$  (Figure 4.15) were applied to the surface of the circular opening and the time step was set as 1 min/step. The room temperature is constant at 22 °C. The convective heat exchange with air is considered and convective heat transfer coefficient is assumed as 13 W/(m<sup>2</sup>·°C). The input parameters for the simulation are shown in Table 4.3.

### **Simulation results of heater test # CM-M-TM**

The comparison of simulation results and test results of temperature evolution at six monitoring points is shown in Figure 4.18. The simulation results (dashed line) of temperature evolution are generally consistent with the tests results (solid line). The simulation results confirmed the influence of the damaged zone to the temperature distribution along the horizontal and vertical direction which have obvious differences.



(a) TC#1, TC#2, TC#3



(b) TC#4, TC#5, TC#6

Figure 4.18 Comparison of simulation results and test results at different temperature monitoring points: (a) TC#1, TC#2, TC#3; (b) TC#4, TC#5, TC#6 (#CM-M-TM).

One explanation for the temperature discrepancies between simulation results and test results is mainly because of the actual laboratory heater test was carried out under 3D condition which was simplified to a plane strain problem in 2D numerical simulation. In other words, the temperature monitoring points in the 2D numerical simulation cannot be fully matched to the actual positions temperature monitoring points (Figure 3.31). Another reason is due to the limitation of the numerical model, the actual effect of elevated temperature on the damaged zone maybe much more complicated.

From the simulation results as shown in Figure 4.19, it can be found that the damaged zone was extended only to a limited extent after heating.

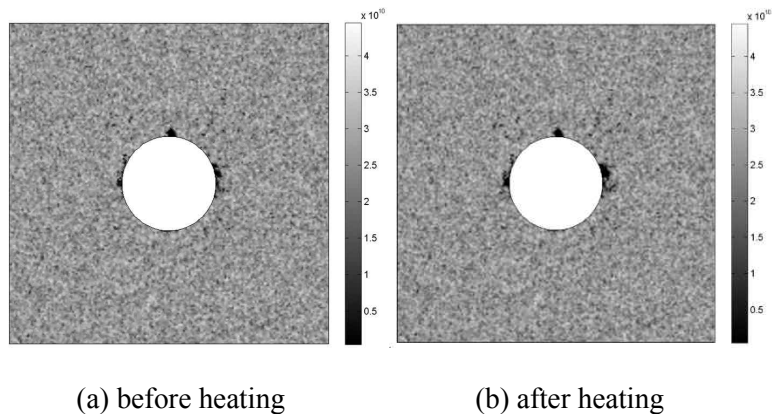


Figure 4.19 Simulated damaged zone around circular opening: (a) before heating; (b) after heating (#CM-M-TM). (Unit: Pa)

This phenomenon was partially proved by experimental observations (Figure 3.40 and Figure 3.41) where fractures initiated on the surface of the circular opening after heating and also reflected by the results of AE source locations (Figure 3.42). Furthermore, the simulation results are similar with the in situ experimental findings through GPR monitoring at borehole (ONK-EH3) in the single borehole heater test of POSE at ONKALO URL where EDZ type damage (Figure 2.10) was observed and the damage around the borehole wall got deeper after heating as aforementioned in section 2.1.2.

## **4.4 Case study - Äspö Pillar Stability Experiment (APSE)**

For the purpose of verifying the applicability of the numerical model, numerical study on coupled thermo-mechanical behavior of rock pillar in the APSE was implemented. In this case study, 2D numerical simulation was carried out at the horizontal cross-section of two deposition holes to investigate the thermo-mechanical behaviors of the rock pillar. In order to model the horizontal cross section of the deposition holes, the applied boundary stresses in the 2D numerical simulation have to be defined. Therefore, 3D numerical simulation was conducted firstly to evaluate the mechanical excavation induced stress distribution after the excavation of the test tunnel and deposition holes using elastic model. And the calculated stress values in 3D numerical simulation were used as the boundary stresses for 2D numerical simulation.

### **3D numerical simulation of the excavation stages**

The orientation of the experiment tunnel in relation to the direction of major principal stress is shown in Figure 4.20. The general layout and theoretical section of the tunnel are shown in Figure 4.21. The tunnel cross-section was shaped in such a way that the stress effect below the tunnel floor was maximized.

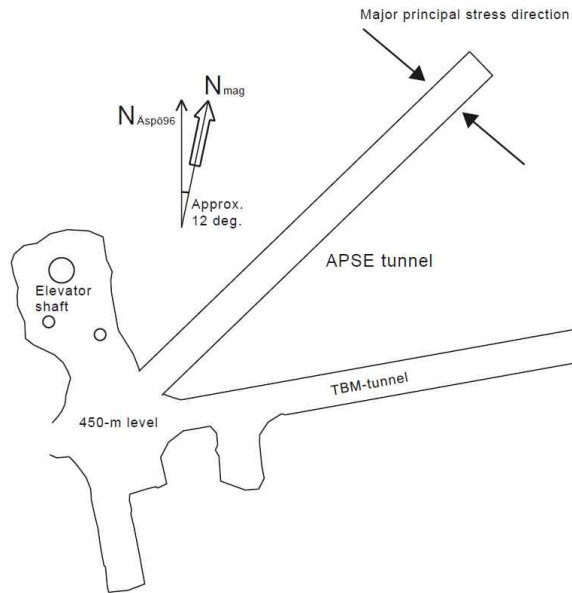


Figure 4.20 Orientation of the APSE tunnel in relation to the direction of major principal stress (Andersson, 2007).

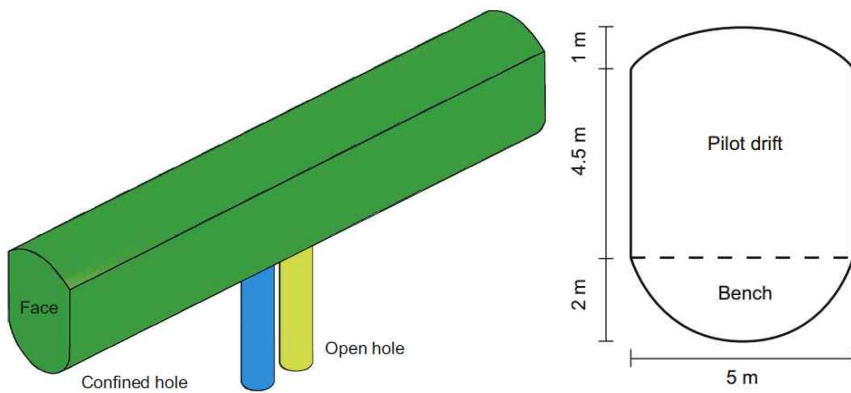


Figure 4.21 General layout and theoretical section of the APSE tunnel (Andersson, 2007).

The model geometry for 3D simulation is shown in Figure 4.22. The 3D numerical model has a side length of 50m. The domain was automatically meshed by the default settings of COMSOL (fine, tetrahedral elements) and the total number of elements was 72395. The section of the modelled tunnel is 7.5m high and 5m wide which is fully consistent with the theoretical section of the APSE tunnel as shown in Figure 4.21. Two boreholes (1.75m in diameter and 6.5m in depth) are also created in the 3D numerical model.

The initial principal stresses (in situ stresses),  $\sigma_1 = -30.0$  MPa,  $\sigma_2 = -15.0$  MPa and  $\sigma_3 = -10.0$  MPa which are based on the back calculated value from Andersson (2007) are applied (negative values represent compression) in the directions of x-, y- and z- direction, respectively.

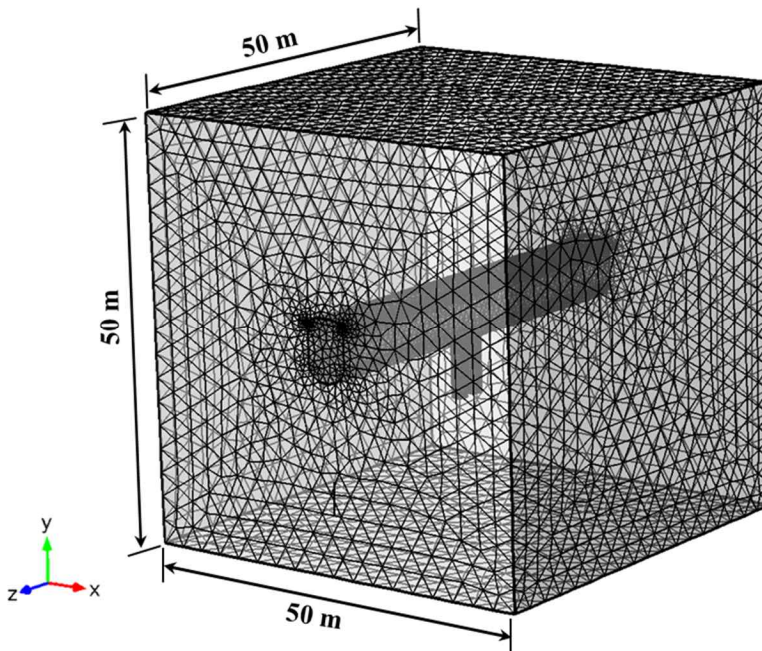


Figure 4.22 Model geometry for 3D simulation.

The properties of Äspö diorite were measured from the laboratory tests by Andersson (2007) and the thermal properties of Äspö diorite were established by Staub et al. (2004) and Kristensson and Hökmark (2007) as shown in Table 4.4.

Table 4.4 Äspö diorite properties derived from laboratory tests (Staub et al. 2004, Andersson 2007, Kristensson and Hökmark 2007).

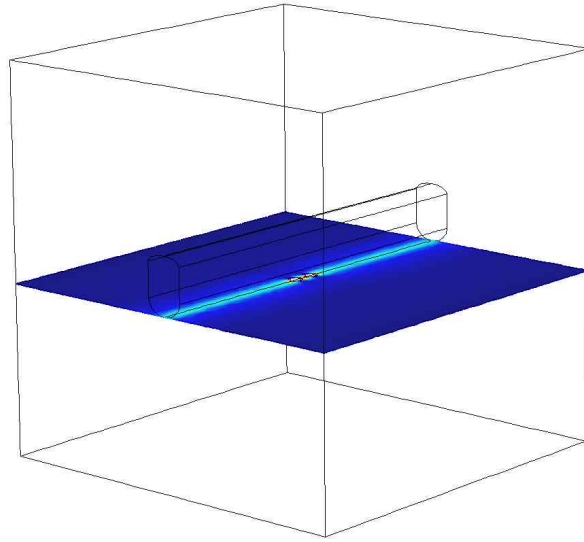
<b>Property</b>	<b>Mean value</b>	<b>Unit</b>
Uniaxial compressive strength, $\sigma_c$	211	MPa
Young's modulus, intact rock, E	76	GPa
Young's modulus, rock mass	55	GPa
Density, $\rho$	2750	kg/m <sup>3</sup>
Poisson's ratio, intact rock, $\nu$ ,	0.25	-
Tensile strength, $\sigma_t$	14.9	MPa
Friction angle, intact rock, $\phi$	49	°
Cohesion, intact rock, c	31	MPa
Initial temperature of rock mass, $T_0$	14.5	°C
Thermal conductivity, $\lambda$	2.6	W/(m.°C)
Specific heat capacity, c	770	J/(kg.°C)
Coefficient of linear expansion, $\alpha$	7	$\times 10^{-6} / ^\circ\text{C}$
Crack initiation stress, AE	MPa	121
Crack initiation stress, strain gauge	MPa	95

Table 4.5 Analysis steps of the excavation stages in the 3D simulation.

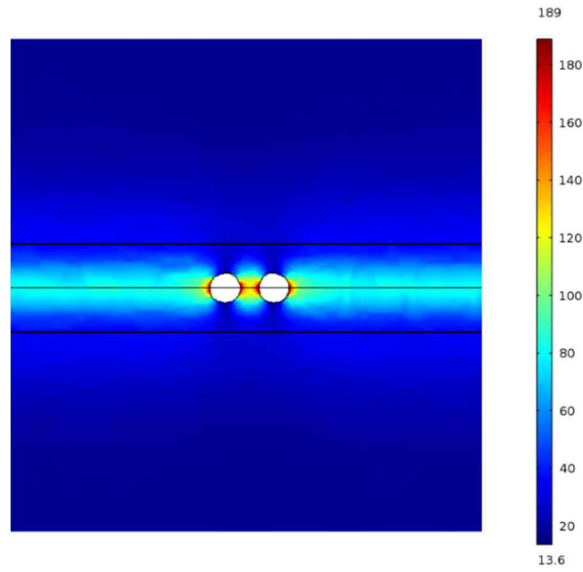
<b>Step No.</b>	<b>Excavation stages</b>
1	Excavation of test tunnel
2	Excavation of deposition hole #1
3	Confinement pressure (0.7 MPa) applied to deposition hole #1
4	Excavation of deposition hole #2

In 3D numerical simulation, in order to calculate the stress state after the excavation, five analysis steps are considered: in the first step, the stress state of the rock mass before excavating the tunnel was calculated (i.e. initial stress state). The following four analysis steps as shown in Table 4.5 which are accordance with the excavation stages, calculate the stress distribution after each excavation. It should be noted that the Young's modulus of rock mass (55GPa) was used in this simulation (Andersson et al., 2009).

The distribution of tangential stress ( $\sigma_1$ - $\sigma_3$ ) at the top of the borehole after the final excavation stage (i.e. after excavation of the second borehole) is shown in Figure 4.23. The simulation result shows good agreement with Andersson (2007) who investigated the excavation-induced maximum tangential stress at the surface of borehole using three-dimensional boundary element code Examine-3D (Rocscience Inc.) as shown in Figure 4.24.



(a) cross-section at top of the borehole (x-z plane)



(b) tangential stress at the top of borehole

Figure 4.23 Simulation results after the final excavation stage: (a) cross-section at top of the borehole (x-z plane); (b) tangential stress at the top of borehole. (Unit: MPa)

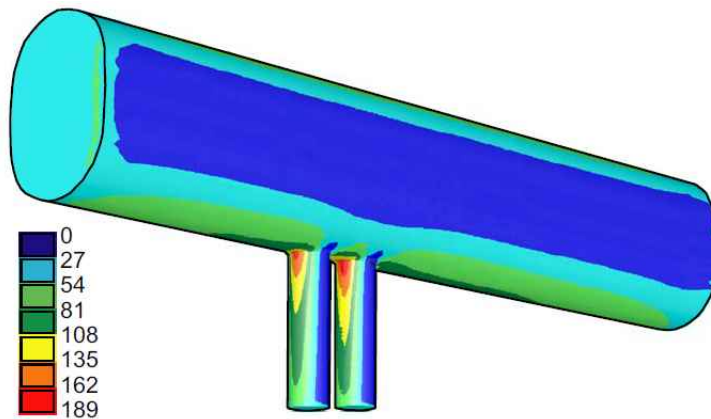


Figure 4.24 Excavation induced maximum tangential stress at the surface of borehole (Andersson, 2007).

The layout of two boreholes and the heaters locations (four red points represent the heater positions) are shown in Figure 4.25, where the right borehole (DQ0066G01) is confined with 0.7MPa pressure and temperature measuring point was locate (marked with red circle) at 3 mm into the pillar wall of left borehole (DQ0063G01). The heat power of four heaters during the heating phase of 66 days is shown in Figure 4.26.

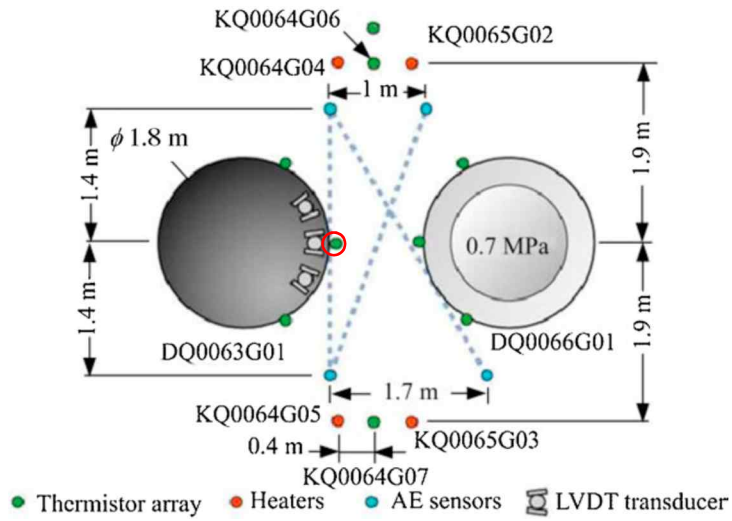


Figure 4.25 Layout of boreholes heaters and sensors (Andersson, 2007).

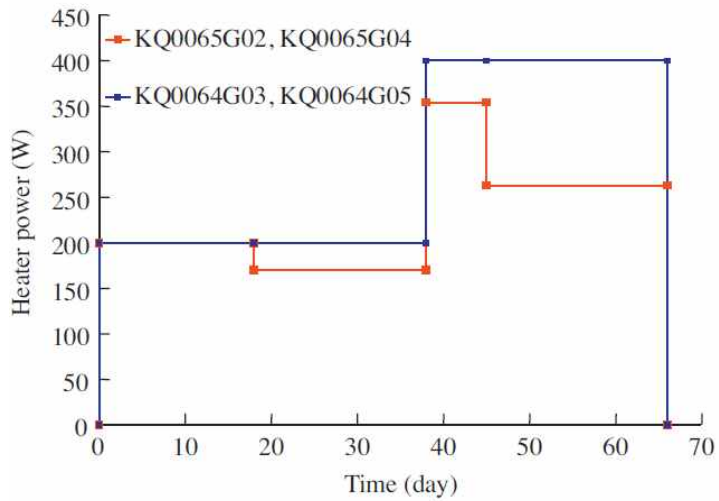


Figure 4.26 Heater power (Andersson, 2007).

Numerical simulation of uniaxial compression tests were carried out to calibrate the input parameters to match the mechanical properties of Äspö diorite. The calibrated input parameters for 2D numerical simulation are summarized in Table 4.6. The thermal properties of rock mass used in 2D simulation were also shown in the Table 4.6 which are from Staub et al. (2004) and Kristensson and Hökmark (2007).

Table 4.6 Input parameters for 2D numerical simulation.

<b>Input parameters</b>	<b>Value</b>	<b>Unit</b>
Homogeneity index, $m$	5	-
Compressive strength, $\sigma_0$	534.1	MPa
Ratio of compressive strength to tensile strength	14.2	-
Young's modulus, $E_0$	85.7	GPa
Poisson's ratio, $\nu$	0.25	-
Friction angle, $\phi$	49	°
Density, $\rho$	2750	kg/m <sup>3</sup>
Initial temperature of rock mass, $T_0$	14.5	°C
Thermal conductivity, $\lambda$	2.6	W/(m.°C)
Specific heat capacity, $c$	770	J/(kg.°C)
Coefficient of linear expansion, $\alpha$	7	$\times 10^{-6}$ /°C

In 2D numerical simulation, the horizontal cross section at 3.5m depth below the tunnel floor is modeled for the purpose comparing simulation results with previous studies. The dimension of the 2D numerical model is  $20\text{m} \times 10\text{m}$  and totally 13272 triangular elements was generated as shown in Figure 4.27.

The boundary stresses are  $-11.2\text{ MPa}$  and  $-42.1\text{ MPa}$  in x-axis and y-axis direction, respectively. These stresses are decided based on the results of 3D simulation. Confinement pressure of  $0.7\text{ MPa}$  is applied to the right borehole. For the thermal boundary condition, the outer boundaries of the numerical model were assumed to be constant at  $14.5^\circ\text{C}$  and heat convection at the surface of boreholes was considered and  $0.5\text{ W}/(\text{m}^2 \cdot ^\circ\text{C})$  was used as heat transfer coefficient (Andersson et al. 2009). The simulated temperature distribution after heating 66 days is shown in Figure 4.28.

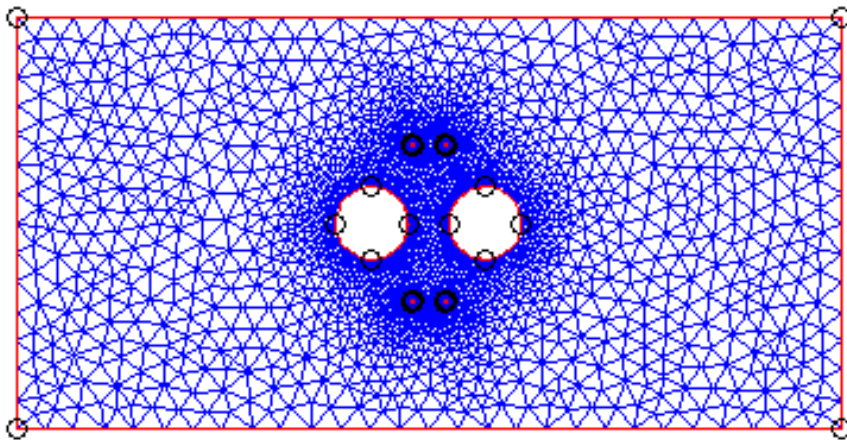


Figure 4.27 Mesh of 2D numerical model ( $20\text{m} \times 10\text{m}$ ).

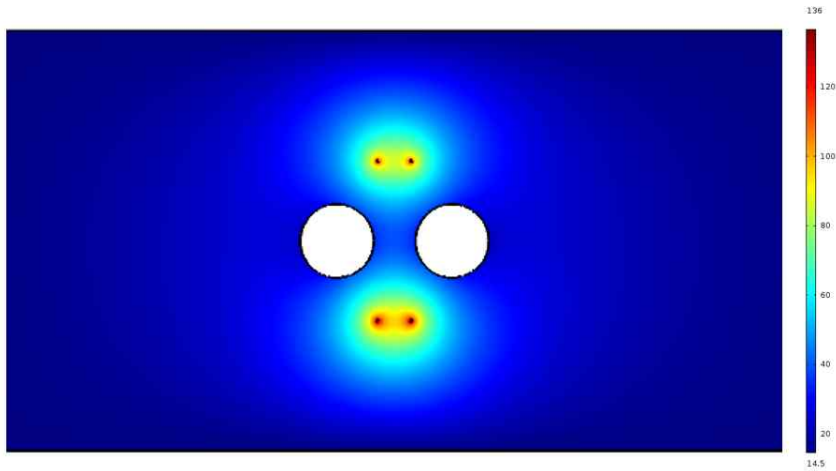


Figure 4.28 Temperature distribution after heating 66 days. (Unit: °C)

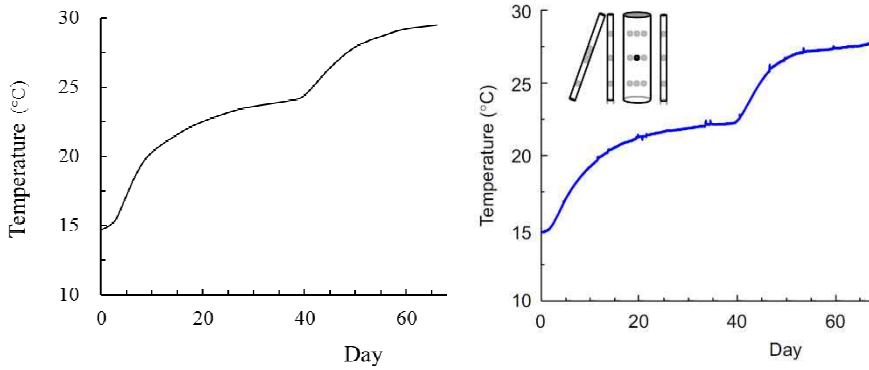
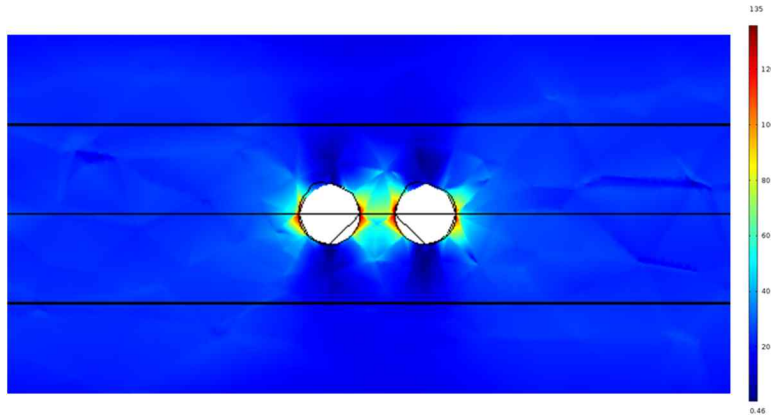


Figure 4.29 Temperature evolution at monitor point A: (a) simulation results; (b) measured results (Andersson et al., 2009).

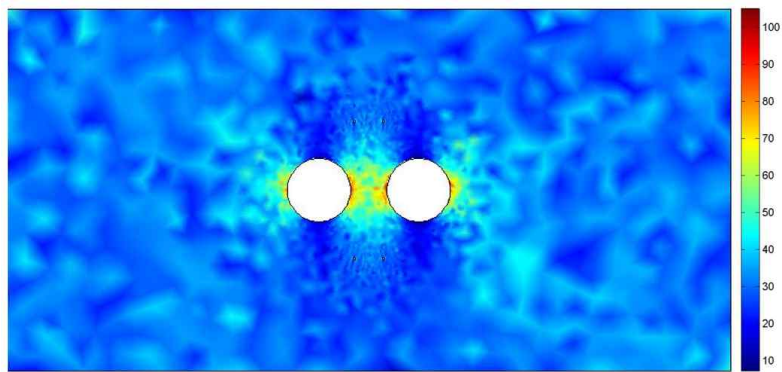
The simulation result of temperature evolution at the point A (near to the wall surface of the left borehole) during heating is plotted and compared with the measured temperature from Andersson (2007) as shown in Figure 4.29.

In general, the overall trend of the simulation result of temperature evolution at monitor point A agree with the in situ measured result. The simulated temperature at point A is about 2°C higher than the monitoring result after 66 days of heating. The temperature discrepancy maybe due to the in situ water flow in both of the boreholes found by Andersson (2007) which result in additional heat convection. In addition, in 2D numerical simulation, the heat flux along the vertical direction of the borehole is not considered and it could be another reason for the discrepancy.

Figure 4.30 shows the comparison of tangential stress distribution of the final excavation step from the 3D model (cross-section at 3.5m below the tunnel floor) and the initial condition in the 2D model. It is can be seen that the tangential stress distribution of 2D model is consistent with the 3D model.



(a) 3D model (cross-section at 3.5m below the tunnel floor) after final excavation step



(b) 2D model

Figure 4.30 Comparison of tangential stress: (a) 3D model (cross-section at 3.5m below the tunnel floor)) after final excavation step; (b) 2D model (initial condition). (unit: MPa)

The simulated damaged zone (distribution of Young's modulus) around the rock pillar during heating period is shown in Figure 4.31. The close-up view (6m×6m) of the damaged zone around the pillars after different heating days are shown in Figure 4.32.

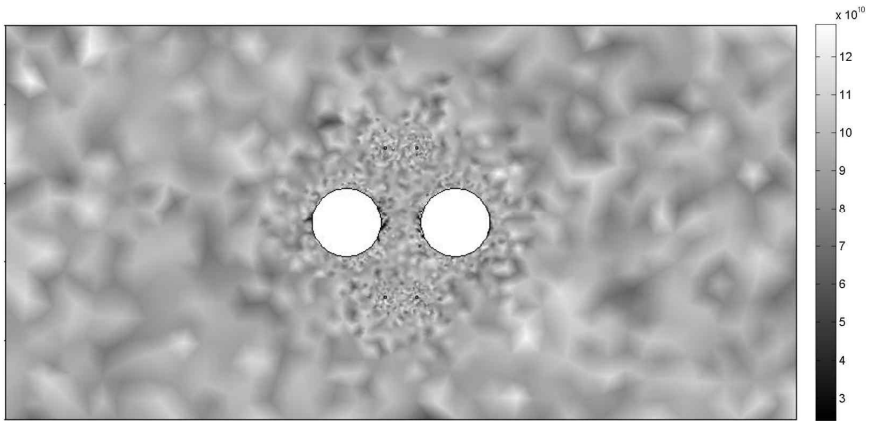


Figure 4.31 Simulated damaged zone after heating 66 days.

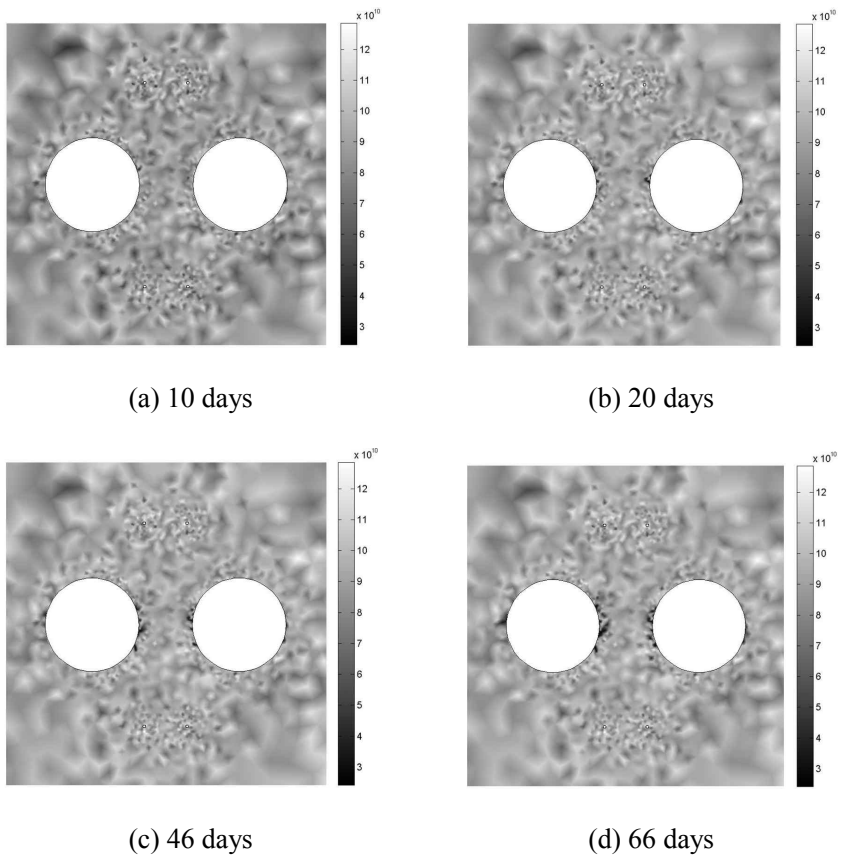


Figure 4.32 Simulated damaged zone: after heating (a) 10 days; (b) 20 days; (c) 46 days; (d) 66 days. (Unit: Pa)

After 10 days heating, very little damage was found at the left side of pillar. After 20 days of heating, damaged zone was enlarged but with quite limited area. After 46 days of heating, damage extended deeper into the left side of pillar. Finally, the damaged zone was significantly enlarged after 66 days heating and a v-shaped damaged zone was formed on the left side of the rock pillar.

The in-situ observation of the failure pattern on rock pillar can be seen in Figure 4.33. V-shaped failed zone (notch) was found at the left side of rock pillar. The confining pressure which applied on the right side borehole has clearly influence to the failure depth, the failure depth at the right side of rock pillar is obviously smaller than the left side.

The simulated damaged zone on rock pillar were compared with previous studies as shown in Figure 4.34. It was found that the simulated depths of the damaged zone in the rock pillar are generally agreed with the simulation results obtained from other numerical codes as shown in Table 4.7. The simulated depth of the damaged zone at the left side of rock pillar in COMSOL is relatively larger, however, it is more comparable to the field experimental findings at the rock pillar as shown in Figure 4.33.



Figure 4.33 Photographs of failure pattern on rock pillar in APSE (Andersson, 2007).

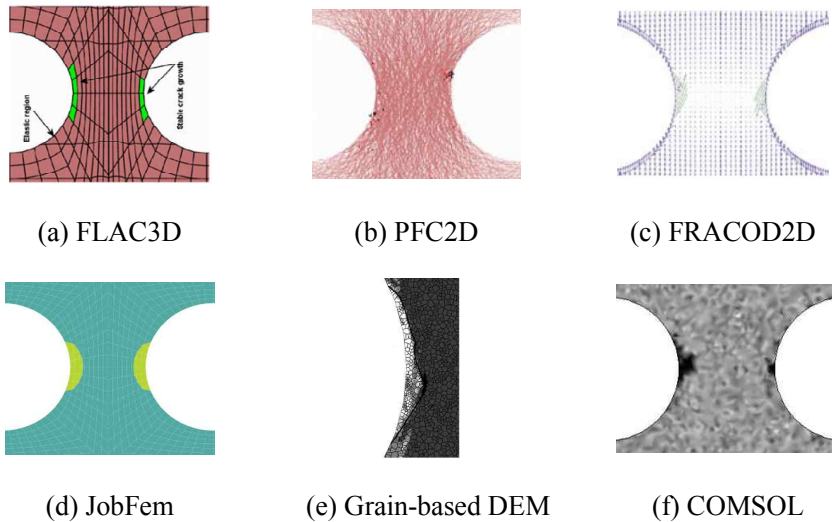


Figure 4.34 Failure depths simulated by different numerical codes:  
 (a) FLAC3D (Wanne et al., 2004); (b) PFC2D (Wanne et al., 2004);  
 (c) FRACOD2D (Rinne et al., 2004); (d) JobFem (Fredriksson et al., 2004);  
 (e) Grain-based DEM (Lan et al., 2013); (f) COMSOL (this research).

Table 4.7 Pillar failure depths obtained from different numerical codes.

Rock pillar	Numerical codes					
	FLAC3D	PFC2D	FRACOD2D	JobFem	Grain-based DEM	COMSOL
Left side	0.10m	0.11m	0.13m	0.12m	0.15m	0.16m
Right side	0.10m	0.15m	0.12m	0.12m	-	0.10m

### Conclusion of case study

Numerical simulations based on elastic damage model were conducted to simulate the coupled thermo-mechanical process of rock pillar in the APSE. Despite the limitations in this two-dimensional numerical model to simulate a three-dimensional process. The simulation results of temperature evolution curve at the monitoring point and the failure depths in the rock pillar shown generally good agreement with the in situ measured data and captured field experimental findings in the APSE. The numerical model is applicable to simulate the damage process of rock mass around a circular opening under thermo-mechanical loading condition in the context of deep geological disposal of HLW.

## 5. Conclusions and discussions

### 5.1 Conclusions

In this research, laboratory biaxial compression tests were carried out to study the characteristics of brittle failure around a circular opening using cubic cement mortar specimen. Furthermore, laboratory heater tests were conducted under confined condition with both intact (undamaged) and damaged cement mortar specimen to investigate the effect of elevated temperature on the evolution of the failed zone. The validations of the numerical model including both elastic damage model and the coupled thermo-mechanical damage model were performed by comparing the biaxial compression tests and heater test results with the simulation results. Finally, for the purpose of verifying the applicability of the numerical model, numerical study of the APSE was conducted.

The conclusions of this research are summarized as follows:

1) The experimental observations of biaxial compression tests indicate that brittle failure around a circular opening is mainly a process of progressive spalling and finally result in v-shaped failed zone.

The depths of failed zone were measured with 3D laser profiler and the relationship between the normalized depth ( $d_f/a$ ) of failed zone and the stress level ( $\sigma_{\max}/\sigma_c$ ) was evaluated with linear empirical formula.

Through comparison of absolute AE energy and AE count results, it was found that the absolute AE energy was more appropriate to classify the failure grades around the circular opening than AE counts. Thus, three failure grades and the corresponding stress levels were identified based on the absolute AE energy results.

2) The results of the heater test using an intact specimen showed that no clear damage was found on the surface of the circular opening after heating. In contrast, for the heater test using a damaged specimen, it was found that fractures initiated on the surface of the circular opening but no obvious further spalling was identified and these experimental findings are consistent with the field observations from the in situ single hole heating damage test (i.e. the third phase of the POSE experiment at the ONKALO URL).

3) The effect of damaged zone on temperature distribution was also investigated in the heater tests. In the heater test using damaged specimen, notable difference in temperature along the direction with damaged zone and without damaged zone was found based on the temperature monitoring results from six thermocouples. This can be explained by the existence of abundant cracks in the damaged zone where the thermal conductivity of the material is lower.

4) Numerical simulation of biaxial compression tests was carried out using an elastic damage model. The simulation results of the damaged zone around circular opening were coincided with the observations from the experimental results. Moreover, based on the damage model, coupled thermo-mechanical

numerical analysis were carried out to simulate the laboratory heater tests. The simulation results of temperature evolution at six monitoring points are generally consistent with the experimental results. The simulation results of the damaged zone are comparable with the laboratory experimental observations and proved by the result of AE source locations.

5) Finally, the applicability of the numerical model was verified through applying it to simulate the coupled thermo-mechanical process in the APSE. The overall trend of the simulated temperature evolution curve at monitoring point was agreed well with the in situ measured data. The simulated depths of the damaged zone in rock pillar were generally consistent with the simulation results from other numerical codes and the in-situ experimental observation. The numerical model is applicable to simulate the coupled thermo-mechanical problems.

It is believed that the results of this research can contribute to the understanding of coupled thermo-mechanical process in the damaged zone around a circular opening in the context of deep geological disposal of HLW.

## 5.2 Discussions

Future works in terms of laboratory experimental study could be performed to improve the knowledge of this research. Firstly, the use of specially designed biaxial loading frame where more AE sensors could be installed to the outer surfaces of the specimen for obtaining more satisfactory results of AE source locations was recommended. Secondly, damage characterization method using other non-destructive testing technique in laboratory-scale, such as infrared thermography technique, is a potential topic for future research. Finally, cement mortar material was used in this research, it may be of interest to perform heater test on rock material such as granite rock or clay rock in the further study.

Numerical simulations were carried out base on two-dimensional numerical model in this research. More sophisticated numerical model for coupled thermo-mechanical simulation need to be developed. In addition, three-dimensional numerical modelling is required for achieving more-realistic simulation results in the future work.

## References

Ababou, R., Valera, I.C., Poutrel, A., 2011, Macro-permeability distribution and anisotropy in a 3D fissured and fractured clay rock: excavation damaged zone around a cylindrical drift in Callovo-Oxfordian Argilite (Bure), *Physics and Chemistry of the Earth, Parts A/B/C*, Vol. 36, pp. 1932-1948.

Andersson, J.C., 2003, Feasibility study: Äspö pillar stability experiment, International Progress Report, IPR-03-01, Svensk Karnbranslehantering AB, Stockholm.

Andersson, J.C., 2007, Äspö pillar stability experiment, Rock mass response to coupled mechanical thermal loading, SKB Report TR-07-01, Svensk Karnbranslehantering AB, Stockholm.

Andersson, J.C., Martin, C.D., 2009, The Äspö pillar stability experiment: Part I – Experiment design, *International Journal of Rock Mechanics and Mining Sciences*, Vol.46, No.5, pp. 865-878.

Andersson, J.C., Martin, C.D., Stille, H., 2009, The Äspö Pillar Stability Experiment: Part II – Rock mass response to coupled excavation-induced and thermal-induced stresses, *International Journal of Rock Mechanics and Mining Sciences*, Vol. 46, No. 5, pp. 879-895.

Araujo, R.G.S., Sousa, J.L.A, Bloch, M., 1997, Experimental investigation on the influence of temperature on the mechanical properties of reservoir rocks. *International Journal of Rock Mechanics and Mining Sciences*, Vol. 34, 459-466.

ASTM E1316-06, 2006, Standard Terminology for Non-Destructive Examinations. ASTM International, USA.

ASTM E976-15, 2015, Standard guide for determining the reproducibility of acoustic emission sensor response. ASTM International, USA.

Bäckblom, G., 2008, Excavation damage and disturbance in crystalline rock—results from experiments and analyses, SKB Technical Report TR-08-08, Svensk Karnbranslehantering AB, Stockholm.

Bäckblom, G., Martin, C.D., 1999, Recent experiments in hard rocks to study the excavation response: implication for the performance of a nuclear waste geological repository, *Tunnelling and Underground Space Technology*, Vol. 14, No. 3, pp. 377-394.

Backers, T., Meier, T., Gipper, P., Stephansson, O., 2014, Rock Mechanics - Confidence of SKB's models for predicting the occurrence of spalling – Main Review Phase, 2014:10, Technical Note 49, Swedish radiation safety authority.

Bae, S.H., 2005, Characteristics of initial rock stress state in Korean tectonic provinces by hydraulic fracturing stress measurement, Ph.D. dissertation, Seoul National University, South Korea. (In Korean)

Barla, M., Antolini, F., 2014, Combined Finite-Discrete numerical modeling of rock spalling in tunnels. *Computer Methods and Recent Advances in Geomechanics*, pp. 1595-1600.

Barry-Macaulay, D., Bouazza, A., Singh, R.M., Wang, B., Ranjith, P.G., 2013, Thermal conductivity of soils and rocks from the Melbourne (Australia) region, *Engineering Geology*, Vol. 164, No. 17, pp. 131-138.

Basista, M., 2003, *Micromechanics of damage in brittle solids, Anisotropic Behaviour of Damaged Materials*, 1st Edition, Springer-Verlag.

Bauer, S.J., Johnson, B., 1979, Effects of slow, uniform heating on the physical properties of the Westerly and Charcoal granites, *Proceedings of the 20th U.S. Symposium on Rock Mechanics*, Austin, Texas.

Beattie, A.G., 2013, *Acoustic Emission Non-Destructive Testing of Structures using Source Location Techniques*, SANDIA Report, SAND 2013-7779.

Birkholzer, J., James, H., Tsang, C.-F., 2012, Geologic disposal of high-level radioactive waste: Status, Key Issues, and Trends. *Annual Review of Environment and Resources*, Vol. 37, pp. 79-106.

Blümling, P., Bernier, F., Lebon, P., Martin, C.D., 2007, The excavation damaged zone in clay formation time-dependent behaviour and influence on performance assessment, *Physics and Chemistry of the Earth, Parts A/B/C*, Vol. 32, pp. 588-599.

Bossart, P., Trick, T., Meier, P. M., Mayor, J., 2004, Structural and hydrogeological characterisation of the excavation-disturbed zone in the Opalinus Clay (Mont Terri Project, Switzerland), *Applied Clay Science*, Vol. 26, No. 1-4, pp. 429-448.

Cai, M., Kaiser, P.K., Martin, C.D., 1998, A tensile model for the interpretation of microseismic events near underground openings, *Pure and Applied Geophysics*, Vol. 152, No. 1, pp. 67-92.

Cao, R., Cao, P., Lin, H., Pu, C.Z., Ou, K., 2016, Mechanical behavior of brittle rock-like specimens with pre-existing fissures under uniaxial loading: experimental studies and particle mechanics approach, *Rock Mechanics and Rock Engineering*, Vol. 49, No. 3, pp. 763-783.

Carlson, S. R., Jansen, D. P., Young, R. P., 1993, Thermally induced fracturing of Lac du Bonnet granite, Technical Report, RP020 AECL, Queen's University, Kingston, pp.1-13.

Carter, B.J., Lajtai, E.Z., Petukhov, A., 1991, Primary and remote fracture around underground cavities, *International Journal for Numerical & Analytical Methods in Geomechanics*, Vol.15, No.1, pp. 21-40.

Chang, C.L., Chang, M., 2009, Inverse determination of thermal conductivity using semi-discretization method, *Applied Mathematical Modelling*, Vol. 33, No. 3, March 2009, pp. 1644-1655.

Cheon, D. S., 2006, Characteristics of brittle failure around a circular opening in homogeneous isotropic rock under true triaxial compression, Ph.D. dissertation, Seoul National University, South Korea. (In Korean)

Chernis, P.J., Robertson, P.B., 1993, Thermal cracking in Lac du Bonnet granite during slow heating to 205° C, AECL-10937, COG-93-358, Whiteshell Laboratories, Pinawa, Manitoba.

Cho, W.J., Kwon, S.K., 2010, Estimation of the thermal properties for partially saturated granite, Engineering Geology, Vol. 115, No. 1-2, pp. 132-138.

COMSOL, 2008, Structures Mechanics Module, User's Guide, COMSOL Multiphysics 3.5a, COMSOL Inc.

COMSOL, 2016, COMSOL Multiphysics®, COMSOL Inc., <http://www.comsol.com>.

Cundall, P.A., 2001, A discontinuous future for numerical modelling in Geomechanics, Geotechnical Engineering, Vol. 149, No. 1, pp. 41-47.

David, C., Menendez, B., Darot, M., 1999, Influence of stress-induced and thermal cracking on physical properties and microstructure of La Peyratte granite, International Journal of Rock Mechanics and Mining Sciences, Vol. 36, pp. 433-448.

Delage, P., 2013, On the thermal impact on the excavation damaged zone around deep radioactive waste disposal, Journal of Rock Mechanics and Geotechnical Engineering, Vol. 5, No. 3, pp. 179-190.

Diederichs, M.S., 2007, The 2003 Canadian geotechnical colloquium: Mechanistic interpretation and practical application of damage and spalling prediction criteria for deep tunneling, Canadian Geotechnical Journal, Vol. 44, No. 9, pp. 1082-1116.

Diederichs, M.S., Kaiser, P.K., Eberhard, E., 2004, Damage initiation and propagation in hard rock during tunneling and the influence of near-face stress rotation, *International Journal of Rock Mechanics and Mining Sciences*, Vol. 41, No. 5, pp. 785-812.

Duan, D., Zhang X.D., Liu L.B., 2014, Research on relationship between parameters correlation of acoustic emission and rock failure, *Sensors & Transducers*, Vol. 183, No. 12, pp. 147-154.

Emsley, S., Olsson, O., Stenberg, L., Alheid, H. J., Falls, S., 1997, ZEDDEX - A study of damage and disturbance from tunnel excavation by blasting and tunnel boring, SKB TR-97-30, Karnbranslehantering AB, Stockholm.

Ewy, R.T. and Cook, N.G.W., 1990, Deformation and fracture around cylindrical openings in rock: Parts I and II, *International Journal of Rock Mechanics and Mining Sciences & Geomechanics Abstracts*, Vol. 27, pp. 387-427.

Fairhurst, C., Damjanac, B., 1996, The excavation damage zone an international perspective, *Proceedings of the EDZ Workshop*, Canadian Nuclear Society, pp. 3-14.

Fairhurst, C., Gera, F., Gnirk, P., Gray, M., Stillborg, B., 1993, OECD/NEA International Stripa Project 1980-1992, Overview Volume I, Executive Summary, SKB, Stockholm.

Fakhimi, A., Carvalho, F., Ishida, T., Labuz, J.F., 2002, Simulation of failure around a circular opening in rock, *International Journal of Rock Mechanics and Mining Sciences*, Vol. 39, No. 4, pp. 507-515.

Fang, Z., Harrison, J.P., 2002, Development of a local degradation approach to the modelling of brittle fracture in heterogeneous rocks, *International Journal of Rock Mechanics and Mining Sciences*, Vol. 39, pp. 443-457.

Feng, X.-T., Pan, P.-Z., Zhou, H., 2006, Simulation of the rock microfracturing process under uniaxial compression using an elasto-plastic cellular automaton, *International Journal of Rock Mechanics and Mining Sciences*, Vol. 43, No. 7, pp. 1091-1108.

Ferrero, A. M., Marini, P., 2001, Technical Note Experimental Studies on the Mechanical Behaviour of two Thermal Cracked Marbles, *Rock Mechanics and Rock Engineering*, Vol. 34, No. 1, pp. 57-66.

Fredriksson, A., Staub, I., Outters, N., 2004, Äspö Pillar Stability Experiment, Final 2D coupled thermo-mechanical modelling, SKB R-04-02, Svensk Karnbranslehantering AB, Stockholm.

Friedman, M., Handin, J., Higgs, N. G., Lantz, J. R., 1979, Strength and ductility of four dry igneous rocks at low pressures and temperatures to partial melting, paper presented at 20th U.S. Symposium on Rock Mechanics, Austin, Texas.

Garza-Cruz, T.V., Pierce, M., Kaiser, P.K., 2014, Use of 3DEC to study spalling and deformation associated with tunneling at depth, Seventh International Conference on Deep and High Stress Mining, Ontario, Canada.

Ghassemi, A., 2012, A review of some rock mechanics issues in geothermal reservoir development. *Geotechnical and Geological Engineering*, Vol. 30, No. 3, pp. 647-664.

Gholizadeh, S., Leman, Z., Baharudin, B.T.H.T., 2015, A review of the application of acoustic emission technique in engineering, Vol. 54, No. 6, pp. 1075-4095.

Godin, N., Mili, M.R., Reynaud, P., Fantozzi, G., Lamon, J., 2011, Identification of damage modes in ceramic matrix composites by acoustic emission signal pattern recognition, *Mechanical Properties and Performance of Engineering Ceramics and composites VI*, Wiley & Sons, Inc., New Jersey.

Goktan, R.M., Yilmaz, N.G., 2005, A new methodology for the analysis of the relationship between rock brittleness index and drag pick cutting efficiency, *Journal of The South African Institute of Mining and Metallurgy*, Vol. 105, No. 10, pp. 727-732.

Golshani, A., Okui, Y., Oda, M., Suzuki, K., 2005, Simulation of damage around a circular opening in rock, 11th International Conference of IACMAG, Turin, Italy.

Grosse, C., Ohtsu, M., 2008, *Acoustic emission testing*, Springer, Berlin, Germany.

Hajiabdolmajid, V., Kaiser, P.K., Martin, C.D., 2002, Modelling brittle failure of rock. *International Journal of Rock Mechanics and Mining Sciences*, Vol. 39, pp. 731-741.

Handin, J., Friedman, M., Johnson. B., 1977, Study, evaluate, measure and calculate the thermal cracking of rocks, Final Report, U.S. Air Force Geophysics Laboratory Report, AFGL-TR-77-0122.

Heuze, F.E., 1983, High-temperature mechanical, physical and thermal properties of granitic rocks - A review, *International Journal of Rock Mechanics and Mining Sciences & Geomechanics Abstracts*, Vol. 20, No. 1, pp. 3-10.

Hoek, E., Martin, C.D., 2014, Fracture initiation and propagation in intact rock – A review, *Journal of Rock Mechanics and Geotechnical Engineering*, Vol. 6, No. 4, pp. 287-300.

Hökmark, H., Lönnqvist, M., Kristensson, O., Sundberg, J., Hellström, G., 2009, Strategy for thermal dimensioning of the final repository for spent nuclear fuel, SKB R-09-04, Svensk Karnbranslehantering AB, Stockholm.

Homand-Etienne, F., R. Houpert, R., 1989, Thermally induced microcracking in granites: characterization and analysis, *International Journal of Rock Mechanics and Mining Sciences & Geomechanics Abstracts*, Vol. 26, No. 2, pp. 125-134.

Hou, Z., 2003, Mechanical and hydraulic behavior of rock salt in the excavation disturbed zone around underground facilities, *International Journal of Rock Mechanics and Mining Sciences*, Vol. 40, No. 5, pp. 725-738.

Hsiung, S.M., Chowdhury, A.H., Nataraja, M.S., 2005, Numerical simulation of thermal–mechanical processes observed at the Drift-Scale Heater Test at Yucca Mountain, Nevada, USA, *International Journal of Rock Mechanics and Mining Sciences*, Vol. 42, No. 5–6, pp. 652-666.

Huang, M., Jiang, L., Liaw, P.K., Brooks, C. R., Seeley, R., Klarstrom, D. L., 1998, Using Acoustic Emission in Fatigue and Fracture, *Materials Research, Journal of Materials*, Vol. 50, No. 11, pp. 1-12.

Hucka, V., Das, B., 1974, Brittleness determination of rocks by different methods, *International Journal of Rock Mechanics and Mining Sciences & Geomechanics Abstracts*, Vol. 11, No. 10, pp. 389-392.

Hudson, J.A., Bäckström, A., Rutqvist, J., Jing, L., Backers, T., Chijimatsu, M., Christiansson, R., Feng, X.T., Kobayashi, A., Koyama, T., Lee, H.S., Neretnieks, I., Pan, P.Z., Rinne, M., Shen, B.T., 2009, Characterising and modelling the excavation damaged zone in crystalline rock in the context of radioactive waste disposal, *Environmental Geology*, Vol.57, No.6, pp. 1275-1297.

Hudson, J.A., Fairhurst, C., 1969, Tensile strength, Weibull's theory and a general statistical approach to rock failure. Structure, solid Mechanics and engineering design, *Proceedings of Southampton Civil Engineering Materials Conference, Part I, Univ. Southampton*, pp. 901-914.

Hudson, J.A., Harrison, J.P., 1997, *Rock mechanics interactions and rock engineering systems. Engineering rock mechanics*, 1st Edition, Elsevier Science Ltd, London.

Huotari, T., Kukkonen, I., 2004, Thermal Expansion Properties of Rocks: Literature Survey and Estimation of Thermal Expansion Coefficient for Olkiluoto Mica Gneiss, POSIVA Working Report 04-04, Eurajoki: Posiva Oy.

IAEA, 2009, Geological Disposal of Radioactive Waste: Technological implications for retrievability, IAEA Nuclear Energy Series, No. NW-T-1.19.

Ishida, T., Kinoshita, N., Wakabayashi, N., 2004, Acoustic emission monitoring during thermal cracking of a granite block, heated in a center hole, Proceedings of the ISRM International Symposium, 3rd ARMS, pp. 133-138.

Jansen, D.P., Carlson, S.R., Young, R.P., Hutchins, D.A., 1993, Ultrasonic imaging and acoustic emission monitoring of thermally induced microcracks in Lac du Bonnet Granite, Journal of Geophysical Research: Solid Earth, Vol. 98, No. B12, pp. 22231-22243.

Jing, L., Stephansson, O., 2007, Fundamentals of discrete Element Methods for Rock Engineering: Theory and Applications, Elsevier.

Johansson, E., Rautakorpi, J., 2000, Rock mechanics stability at Posiva investigation sites Olkiluoto, Hastholmen, Kivetty, Romuvaara, POSIVA Working Report 00-02, Eurajoki: Posiva Oy.

Johansson, E., Siren, T., Hakala, M., Kantia, P., 2014, ONKALO POSE Experiment - Phase 1 & 2: Execution and Monitoring. POSIVA Working Report 2012-60, Eurajoki: Posiva Oy.

Jung, H.Y., 2010, Experimental analysis on the relationship between punch penetration characteristics of rock and cutting performance of a TBM disc cutter, Master thesis, Seoul National University, South Korea. (In Korean)

Kelsall, P.C., Case, J.B., Chabannes, C.R., 1984, Evaluation of excavation-induced changes in rock permeability International Journal of Rock Mechanics and Mining Sciences and Geomechanics Abstracts, Vol. 21, No. 3, pp. 123-135.

Keshavarz, M., Pellet, F., Loret, B., 2010, Damage and changes in mechanical properties of a gabbro thermally loaded up to 1,000°C, Pure and Applied Geophysics, Vol. 167, No. 12, pp. 1511-1523.

Keshavarz, M., Pellet, F.L., Hosseini, K.A., 2009, Comparing the effectiveness of energy and hit rate parameters of acoustic emission for prediction of rock failure, International Symposium on Rock Mechanics, Rock Characterisation, Modelling and Engineering Design Methods, SinoRock 2009, Hong Kong, China.

Khazaei, C., Hazzard, J., Chalaturnyk, R., 2015, Damage quantification of intact rocks using acoustic emission energies recorded during uniaxial compression test and discrete element modeling, Computers and Geotechnics, Vol. 67, pp. 94-102.

Klerck, P.A., 2000, The finite element modelling of discrete fracture in quasi-brittle materials, Ph.D. dissertation, University of Wales, Swansea, UK.

Klubertanz, G., Folly, M., Hufschmied, P., Frank, E., 2008, Impact of the thermal load on the far field and galleries of a HLW-repository, Physics and Chemistry of the Earth, Parts A/B/C, Vol. 33, Supplement 1, 2008, pp. 457-461.

Kolgaonkar, A., 2005, Correlation of acoustic emission parameters with weight and velocity of moving vehicles, Master thesis, University of Central Florida.

Koyama, T., Chijimatsu, M., Shimizu, H., Nakama, S., Fujita, T., Kobayashi, A., Ohnishi, Y., 2013, Numerical modeling for the coupled thermo-mechanical processes and spalling phenomena in Äspö Pillar Stability Experiment (APSE), Journal of Rock Mechanics and Geotechnical Engineering, Vol. 5, No. 1, pp. 58-72.

Kristensson, O., Hökmark, H., 2007, Äspö Hard Rock Laboratory. Prototype Repository. Thermal 3D modelling of Äspö Prototype Repository, SKB IPR-07-01, Svensk Karnbranslehantering AB, Stockholm.

Kukkonen, I., Lindberg, A., 1998, Thermal properties of rocks at the investigation sites: measured and calculated thermal conductivity, specific heat capacity and thermal diffusivity, POSIVA Working Report 98-09e, Eurajoki: Posiva Oy.

Kwon, S., Cho, W.J., 2008, The influence of an excavation damaged zone on the thermal-mechanical and hydro-mechanical behaviors of an underground excavation, *Engineering Geology*, Vol.101, pp. 110-123

Kwon, S., Lee, C., Yoon, C.-H., Cho, W.-J., 2013, In situ borehole heater test at the KAERI Underground Research Tunnel in granite, *Annals of Nuclear Energy*, Vol. 62, pp. 526-535.

Labioise, V., Vietor, T., 2014, Laboratory and in situ simulation tests of the excavation damaged zone around galleries in Opalinus Clay *Rock Mechanics and Rock Engineering*, Vol. 47, No. 1, pp. 57-70.

Laouafa, F., Farret, R., Vidal-Gilbert, S., Kazmierczak, J.B., 2016, Overview and modeling of mechanical and thermomechanical impact of underground coal gasification exploitation, *Mitigation and Adaptation Strategies for Global Change*, Vol. 21, No. 4, pp. 547-576.

Lajtai, E.Z., Carter, B.J., Ayari, M.L., 1990, Criteria for brittle fracture in compression, *Engineering Fracture Mechanics*, Vol. 37, No. 1, pp. 59-74.

Lan, H., Martin, C.D., Andersson, J.C., 2013, Evolution of in situ rock mass damage induced by mechanical-thermal loading, *Rock Mechanics and Rock Engineering*, Vol.46, No.1, pp. 153-168.

Lee, C.S., 2012, Characterization of thermal-mechanical behavior of rock mass in the excavation damaged zone at KURT, Ph.D. dissertation, Seoul National University, South Korea. (In Korean)

Lemaitre, J., 1992, *A course on damage mechanics*, Springer-Verlag, Berlin Heideberg, New York.

Li, L.C., Tang, C.A., Zhu, W.C., Liang, Z.Z., 2009, Numerical analysis of slope stability based on the gravity increase method, *Computers and Geotechnics*, Vol. 36, No. 7, pp. 1246-1258.

Li, Y., Weetjens, E., Sillen, X., Vietor, T., Li, X., Delage, P., Labiouse, V., Charlier, R., 2014, Consequences of the thermal transient on the evolution of the damaged zone around a repository for heat-emitting high-level radioactive waste in a clay formation: a performance assessment perspective, *Rock Mechanics and Rock Engineering*, Vol. 47, No. 1, pp. 3-19.

Liang, Z. Z., Tang, C.A., Zhang, Y.B., Ma, T.H., 2008, On probability model of physico-mechanical parameters of quasi-brittle materials and associated mechanical failure behaviors, *Chinese Journal of Rock Mechanics and Engineering*, Vol. 27, No. 4, 718-727. (In Chinese)

Lisjak, A., Garitte, B., Grasselli, G., Müller, H.R., Vietor, T., 2015, The excavation of a circular tunnel in a bedded argillaceous rock (Opalinus Clay): Short-term rock mass response and FDEM numerical analysis. *Tunneling Underground Space Technology*, Vol. 45, pp. 227-248.

Liu, J., Pei, J., Ma, K., Zhou, H., Hou, M.Z., 2010, Damage evolution and fractal property of salt rock on tensile failure, *Underground Storage of CO<sub>2</sub> and Energy*, pp. 105-112.

Liu, Q., Xu, J., Liu, X.W., Jiang, J.D., Liu, B., 2015, The role of flaws on crack growth in rock-like material assessed by AE technique, *International Journal of Fracture*, Vol. 193, No. 2, pp. 99-115.

Martin, C.D., 1997, Seventeenth Canadian geotechnical colloquium: The effect of cohesion loss and stress path on brittle rock strength, *Canadian Geotechnical Journal*, Vol.34, No.5, pp. 698-725.

Martin, C.D., 2005, Preliminary assessment of potential underground stability (wedge and spalling) at Forsmark, Simpevarp and Laxemar sites, SKB R-05-71, Svensk Karnbranslehantering AB, Stockholm.

Martin, C.D., Christiansson, R., 2009, Estimating the potential for spalling around a deep nuclear waste repository in crystalline rock, *International Journal of Rock Mechanics & Mining Sciences*, Vol. 46, pp. 219-228.

Martin, C.D., Christiansson, R., Söderhäll, J., 2001, Rock stability considerations for siting and constructing a KBS-3 repository. Based on Experiences from Äspö HRL, AECL's URL, tunneling and mining, SKB TR-01-38, Svensk Karnbranslehantering AB, Stockholm.

Martin, C.D., Kaiser, P.K., McCreath, D.R., 1999, Hoek-Brown parameters for predicting the depth of brittle failure around tunnels, Canadian Geotechnical Journal, Vol.36, No.1, pp. 136-151.

Martin, C.D., Lanyon, G.W., Blumling, P., Mayor, J.C., 2003, The excavation disturbed zone around a test tunnel in the Opalinus Clay, Tunneling Association of Canada Annual Publication.

Martino, J.B., Chandler, N.A., 2004, Excavation-induced damage studies at the Underground Research Laboratory, International Journal of Rock Mechanics and Mining Sciences, Vol. 41, No. 8, pp. 1413-1426.

Miao, S. Q., Li, H. P., Chen, G., 2014, Temperature dependence of thermal diffusivity, specific heat capacity, and thermal conductivity for several types of rocks, Journal of Thermal Analysis and Calorimetry, Vol. 115, No. 2, pp. 1057-1063.

Michlmayr, G., Cohen, D., Or, D., 2012, Sources and characteristics of acoustic emissions from mechanically stressed geologic granular media – A review, Earth-Science Reviews, Vol. 112, No. 3-4, pp. 97-114.

Min, K.-B., Rutqvist, J., Tsang, C.-F., Jing, L., 2005, Thermally induced mechanical and permeability changes around a nuclear waste repository - A far-field study based on equivalent properties determined by a discrete approach, International Journal of Rock Mechanics and Mining Sciences, Vol. 42, pp. 765-780.

Mohanto, S., K. Singh, K., Chakraborty, T., Basu, D., 2014, Cyclic Thermo-Mechanical Analysis of Wellbore in Underground Compressed Air Energy Storage Cavern, Geotechnical and Geological Engineering, Vol. 32, No. 3, pp. 601-616.

NEA, 2013, Underground Research Laboratories (URL), Radioactive Waste Management NEA/RWM/R(2013)2.

Otto, C., Kempka, T., 2015, Thermo-Mechanical Simulations of Rock Behavior in Underground Coal Gasification Show Negligible Impact of Temperature-Dependent Parameters on Permeability Changes, *Energies*, Vol. 8, pp. 5800-5827.

PAC, 2007, PCI-2 based ae system user's manual, Rev 3, Physical Acoustics Corporation.

PAC, 2011a, Product data sheet of PICO sensor, Physical Acoustic Corporation.

PAC, 2011b, AEWin Software Installation, Operation and User's Reference Manual, Physical Acoustics Corporation.

Peng, J., Cai, M., Liu, D.Q., He, M.C., Zhou, C.B., 2015, A Phenomenological Model of Brittle Rocks under Uniaxial Compression, *International Journal of Geohazards and Environment*, Vol. 1, No. 2, pp. 53-62.

Perkowski, Z., 2008, Change of thermal conductivity of concrete caused by brittle damage evolution, *Bauphysik*, Vol. 30, No. 6, pp. 434-437.

Picandet, V., Khelidj, A., Bastian, G., 2001, Effect of axial compressive damage on gas permeability of ordinary and high-performance concrete, *Cement and Concrete Research*, Vol. 31, No. 11, pp. 1525-1532.

Plevova, E., Vaculikova, L., Kozusnikova, A., Ritz, M., Martynkova, G. S., 2016, Thermal expansion behaviour of granites, *Journal of Thermal Analysis and Calorimetry*, Vol. 123, No. 2, pp. 1555-1561.

Poelchau, H.S., Baker, D.R., Hantschel, Th., Horsfield, B., Wygrala, B., 1997, Basin simulation and the design of the conceptual basin model, *Petroleum and basin evaluation*, Springer, Berlin, pp. 36-41.

Pollock, A.A., 2013, AE signal features: energy, signal strength, absolute energy and RMS (Rev. 1.2). Mistras Group Inc – technical note 103-22-9/11, 3.

POSIVA, 2009, Olkiluoto Site Description 2008. POSIVA Report 2009-01. Eurajoki: Posiva Oy.

Potyondy, D.O., Cundall, P.A., 2004, A bonded-particle model for rock. *International Journal of Rock Mechanics and Mining Sciences*, Vol. 41, pp. 1329-1364.

Pribnow, D., Williams, C., Sass, J. H., Keating, R., 1996, Thermal conductivity of water-saturated rocks from the KTB pilot hole at temperatures of 25 to 300°C, *Geophysics Research Letters*, Vol. 23, No. 4, pp. 391-394.

Pudewills, A., 2006, Modelling of the hydro-mechanical processes around excavations in rock salt, Eurock 2006: Multiphysics Coupling and Long Term Behaviour in Rock Mechanics, Proceedings of the International Symposium of the International Society for Rock Mechanics, Liège, Belgium.

Pusch, R., 2008, Geological Storage of Highly Radioactive Waste, Current Concepts and Plans for Radioactive Waste Disposal, Springer Berlin Heidelberg.

Pusch, R., Stanfors, R., 1992, The zone of disturbance around blasted tunnels at depth, *International Journal of Rock Mechanics and Mining Sciences Abstract*, Vol. 29, No. 5, pp.447-456.

Ranjith P. G., Viete, D.R., Chen, B.J., Perera, M.S.A., 2012, Transformation plasticity and the effect of temperature on the mechanical behaviour of Hawkesbury sandstone at atmospheric pressure, *Engineering Geology*, Vol. 151, No., pp. 120-127.

Read, R. S., Martino J. B., Dzik, E. J., Oliver, S., Falls, S., Young, R. P., 1997, Analysis and Interpretation of AECL's Heated Failure Tests, Report No: 06819-REP-01200-0070 R00, Atomic Energy of Canada Ltd. Whiteshell Laboratories.

Read, R.S., 2004, 20 years of excavation response studies at AECL's Underground Research Laboratory, *International Journal of Rock Mechanics and Mining Sciences*, Vol.41, No.8, pp. 1251-1275.

Read, R.S., Martin, C.D., 1996, Technical summary of AECL's Mine-by-Experiment Phase I: Excavation response, AECL Report AECL-11311, COG-95-171, Atomic Energy of Canada Limited.

Rinne, M., Shen, B., Lee, H.S., 2004, Äspö Hard Rock Laboratory. Äspö pillar stability experiment. Modelling of Fracture Development of APSE by FRACOD, SKB IPR-04-04, Svensk Karnbranslehantering AB, Stockholm.

Rutqvist, J., 2012, The geomechanics of CO<sub>2</sub> storage in deep sedimentary formations, *Geotechnical and Geological Engineering*, Vol. 30, No. 3, pp. 525-551.

Rutqvist, J., Dobson, P.F., Garcia, J., Hartline, C., Jeanne, P., Curtis M., Oldenburg, C.M., Vasco, D.W., Walters, M., 2015, The northwest Geysers EGS demonstration project, California: Pre-stimulation modeling and interpretation of the stimulation, *Mathematical Geosciences*, Vol. 47, No. 1, pp. 3-29.

Schärli, U., Rybach, L., 1984, On the thermal conductivity of low-porosity crystalline rocks, *Tectonophysics*, Vol. 103, No. 1, pp. 307-313.

Shahidan, S., Pulin, R., Muhamad Bunnori, N., Holford, K.M., 2013, Damage classification in reinforced concrete beam by acoustic emission signal analysis, *Construction and Building Materials*, Vol. 45, pp. 78-86.

Shahidan, S., Zuki, S.S.M., Jamaluddin, N., 2016, Damage grading system for severity assessment on concrete structure, *Case Studies in Construction Materials*, Vol. 5, pp. 79-86.

Shin, S.W., Martin, C.D., Park, E.S., Christiansson, R., 2007, Methodology for estimation of excavation damaged zone around tunnels in hard rock. Presented at the 1st Canada - U.S. Rock Mechanics Symposium, American Rock Mechanics Association.

Shiu, W.J., Dedecker, F., Rachez, X., Peter-Borie, M., 2011, Discrete modeling of near-well thermo-mechanical behavior during CO<sub>2</sub> injection, 2nd International FLAC/DEM Symposium, Melbourne, Australia.

Sinaga, H.H., Phung, B.T., Ao, P.L., Blackburn, T.R., 2011, Partial Discharge Localization in Transformers Using UHF Sensors, 2011 Electrical Insulation Conference, Annapolis, Maryland.

Singh, M., Behrendt, D.R., 1994, Microstructure and mechanical properties of Reaction-Formed Silicon Carbide (RFSC) ceramics, *Materials Science and Engineering A*, Vol. 187, No. 2, pp. 183-187.

Siren, T., Hakala, M., Valli, J., Kantia, P., Hudson, J.A., Johansson, E., 2015, In situ strength and failure mechanisms of migmatitic gneiss and pegmatitic granite at the nuclear waste disposal site in Olkiluoto, Western Finland. *International Journal of Rock Mechanics and Mining Sciences*, Vol. 79, pp. 135-148.

SKB, 2004, Programme for research, development and demonstration of methods for the management and disposal of nuclear waste, including social science research, SKB TR-04-21, Svensk Karnbranslehantering AB, Stockholm.

Staub, I., Andersson, J.C., Magnor, B., 2004, Äspö Pillar Stability Experiment. Geology and mechanical properties of the rock in TASQ, SKB R-04-01, Svensk Karnbranslehantering AB, Stockholm.

Stephansson, O., Gipper, P., 2015, Rock Mechanics - Thermal properties and thermal modelling of the rock in a repository of spent nuclear fuel at Forsmark – Main Review Phase, 2015:01 Technical Note 75, Swedish radiation safety authority.

Sun, G.H., Sui, T., Korsunsky, A.M., 2016, Review of the Hybrid Finite-Discrete Element Method (FDEM), *Proceedings of the World Congress on Engineering 2016 Vol II*, WCE 2016, London, U.K.

Sundberg, J., Hellström, G., 2009, Inverse modelling of thermal conductivity from temperature measurements at the Prototype Repository, Äspö HRL, *International Journal of Rock Mechanics and Mining Sciences*, Vol. 46, No. 6, pp. 1029-1041.

- Tang, C.A., 1997, Numerical simulation of progressive rock failure and associated seismicity, *International Journal of Rock Mechanics and Mining Sciences*, Vol. 34, No. 2, pp. 249-261.
- Tang, C.A., Tang, S.B., 2011, Applications of rock failure process analysis (RFPA) method, *Journal of Rock Mechanics and Geotechnical Engineering*, Vol. 3, No. 4, pp. 352-372.
- Tiryaki, B., 2006, Evaluation of the indirect measures of rock brittleness and fracture toughness in rock cutting, *Journal of The South African Institute of Mining and Metallurgy*, Vol. 106, No. 6, pp. 409-423.
- Tsang, C.-F., Barnichon, J.D., Birkholzer, J., Li, X.L., Liu, H.H., Sillen, X., 2012, Coupled thermo-hydro-mechanical processes in the near field of a high-level radioactive waste repository in clay formations, *International Journal of Rock Mechanics and Mining Sciences*, Vol. 49, pp. 31-44.
- Tsang, C.-F., Bernier, F., Davies, C., 2005, Geohydromechanical processes in the Excavation Damaged Zone in crystalline rock, rock salt, and indurated and plastic clays - In the context of radioactive waste disposal, *International Journal of Rock Mechanics and Mining Sciences*, Vol. 42, No. 1, pp. 109-125.
- Valli, J., Hakala, M., Wanne, T., Kantia, P., Siren, T., 2013, ONKALO POSE Experiment - Phase 3: Execution and Monitoring, POSIVA Working Report 2013-41, Eurajoki: Posiva Oy.
- Wai, R.S.C, Lo, K.Y., Rowe, R.K., 1982, Thermal stress analysis in rocks with nonlinear properties. *International Journal of Rock Mechanics and Mining Sciences & Geomechanics Abstracts*, Vol. 19, No. 5, pp. 211-220.
- Wang, S.H., Lee, C.I., Ranjith, G., Tang, C.A., 2009, Modeling the effects of heterogeneity and anisotropy on the excavation damaged/disturbed zone (EDZ), *Rock Mechanics and Rock Engineering*, Vol. 42, No. 2, pp. 229-258.
- Wang, X.Q., Schubnel, A., Fortin, J., Guéguen, Y., Ge, H.K., 2013, Physical properties and brittle strength of thermally cracked granite under confinement. *Journal of Geophysical Research: Solid Earth*, Vol. 118, No. 12, pp. 6099-6112.

Wanne, T., Johansson, E., Saanio, D.P., 2004, Äspö Pillar Stability Experiment final coupled 3D thermo-mechanical modeling and preliminary particle-mechanical modeling, SKB R-04-03, Svensk Karnbranslehantering AB, Stockholm.

Wanne, T.S., Young, R.P., 2008, Bonded-particle modeling of thermally fractured granite. *International Journal of Rock Mechanics and Mining Sciences*, Vol. 45, No. 5, pp.789-799.

Waples, D.W. & Waples, 2004, A Review and Evaluation of Specific Heat Capacities of Rocks, Minerals, and Subsurface Fluids. Part 1: Minerals and Nonporous Rocks, *Natural Resources Research*, Vol. 13, No. 2, pp. 97-122.

Weibull, W., 1951, A statistical distribution function of wide applicability, *Journal of Applied Mechanics*, Vol. 18, pp. 293-297.

Wong, T.F., Wong, R.H.C., Chau, K.T., Tang, C.A., 2006, Microcrack statistics, Weibull distribution and micromechanical modeling of compressive failure in rock, *Mechanics of Materials*, Vol. 38, pp. 644-681.

Xu, Y., Jiang, L.H., Liu, J.P., Zhang, Y., Xu, J.X., He, G.Q., 2016, Experimental study and modeling on effective thermal conductivity of EPS lightweight concrete, *Journal of Thermal Science and Technology*, p. JTST0023.

Xu, Z. L., 2006, *Introduction to Elasticity*, 4th Edition, Higher Education Press. (In Chinese)

Yong, C., Wang, C.T., 1980, Thermally induced acoustic emission in Westerly granite, *Geophysical Research Letters*, Vol. 7, No. 12, pp. 1089-1092.

Zhang, L.Y., Mao, X.B., X, Liu, R.X., Guo, X.Q., Ma, D., 2014, The mechanical properties of mudstone at high temperatures: an experimental study, *Rock Mechanics and Rock Engineering*, Vol. 47, No.4, pp. 1479-1484.

Zhang, Z.X., 2016, *Rock Fracture and Blasting: Theory and Applications*, 1st Edition, Elsevier Science & Technology.

Zhao, X.D., Zhang, H.X., Zhu, W.C., 2014, Fracture evolution around pre-existing cylindrical cavities in brittle rocks under uniaxial compression, Transactions of Nonferrous Metals Society of China, Vol. 24, No. 3, pp. 806-815.

Zhou, X.P., Ha, Q.L., Zhang, Y.X., Zhu, K.S., 2004, Analysis of the localization of deformation and study on the complete stress-strain relation for brittle rock subjected to dynamic compressive loads, International Journal of Rock Mechanics and Mining Science, Vol. 41, No. 2, pp. 311-319.

Zhu, W.C., Tang, C.A., 2004, Micromechanical model for simulating the fracture process of rock, Rock Mechanics and Rock Engineering, Vol. 37, No. 1, pp. 25-56.

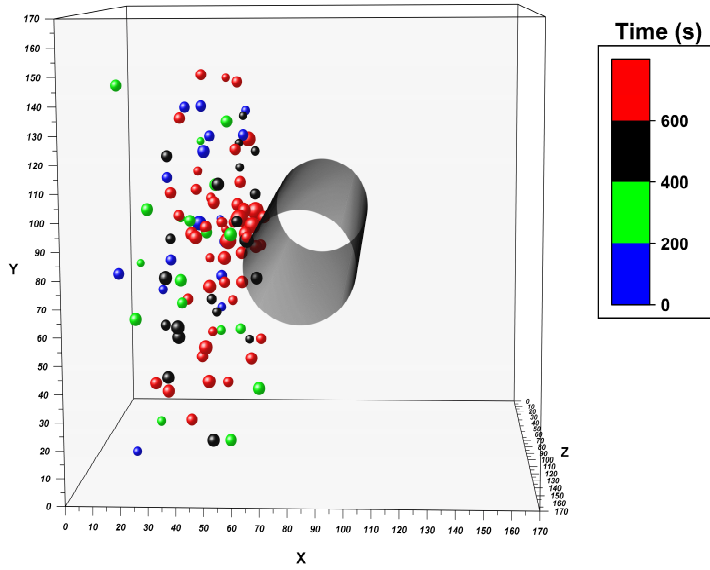
Zhu, W.C., Wei, C.H., 2011, Numerical simulation on mining-induced water inrushes related to geologic structures using a damage-based hydromechanical model, Environmental Earth Sciences, Vol. 62, No. 1, pp. 43-54.

[http://www.engineeringtoolbox.com/convective-heat-transfer-d\\_430.html](http://www.engineeringtoolbox.com/convective-heat-transfer-d_430.html)

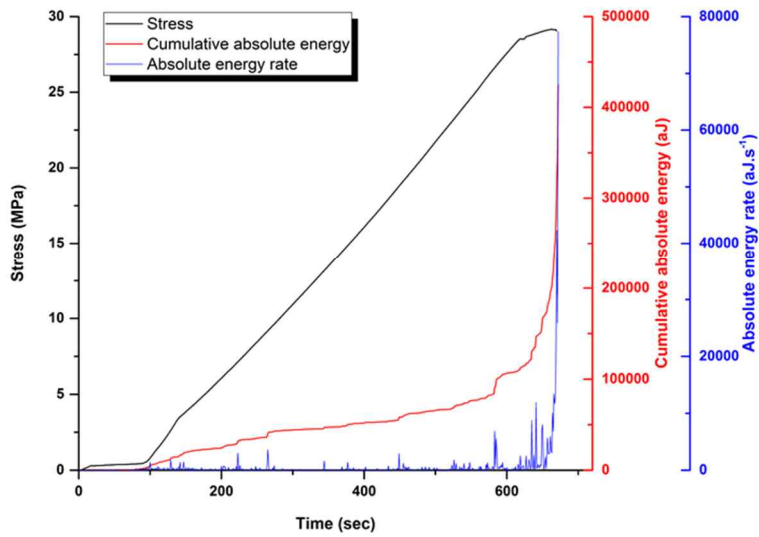
# Appendix

**Appendix A. Summary of experimental results of biaxial compression tests, including the contents as follows:**

- 1) 3D AE source locations
- 2) 3D Laser profiler results
- 3) Cumulative absolute energy and energy rate
- 4) Depth and extent of failed zone

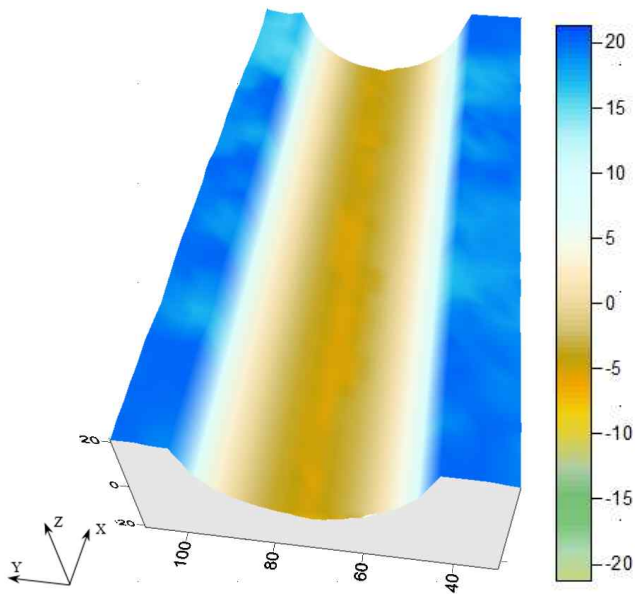


(a) 3D AE source location

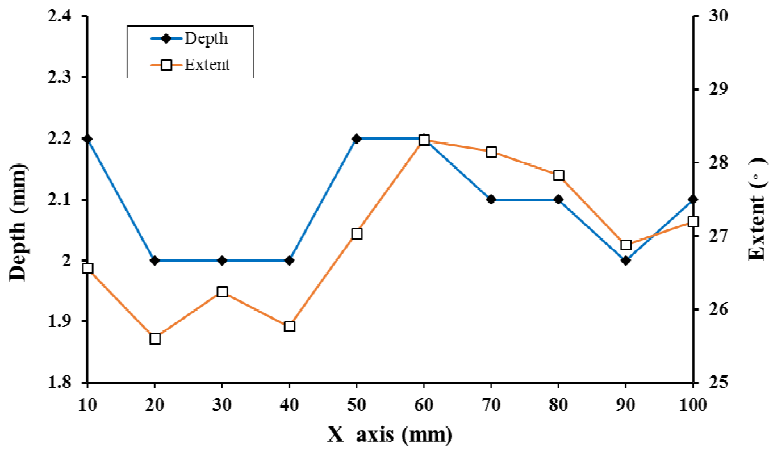


(b) Cumulative absolute energy and energy rate

Figure A.1 Test results of #CM-M1.

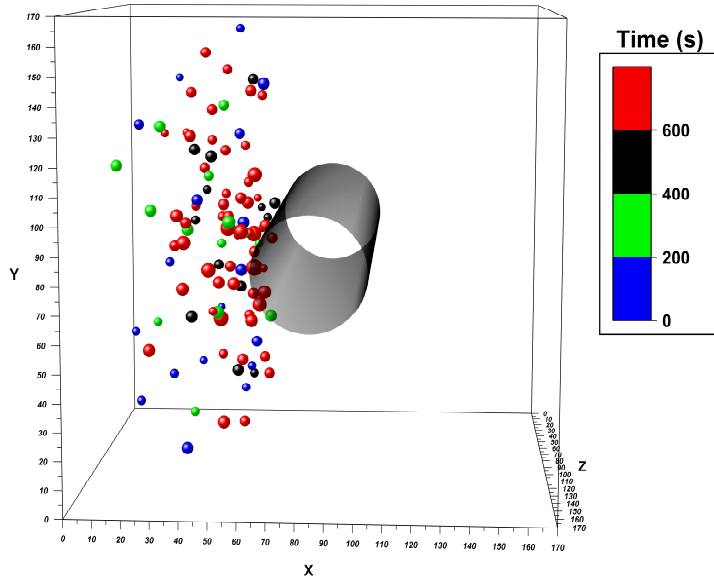


(c) 3D surface of failed zone (Unit: mm)

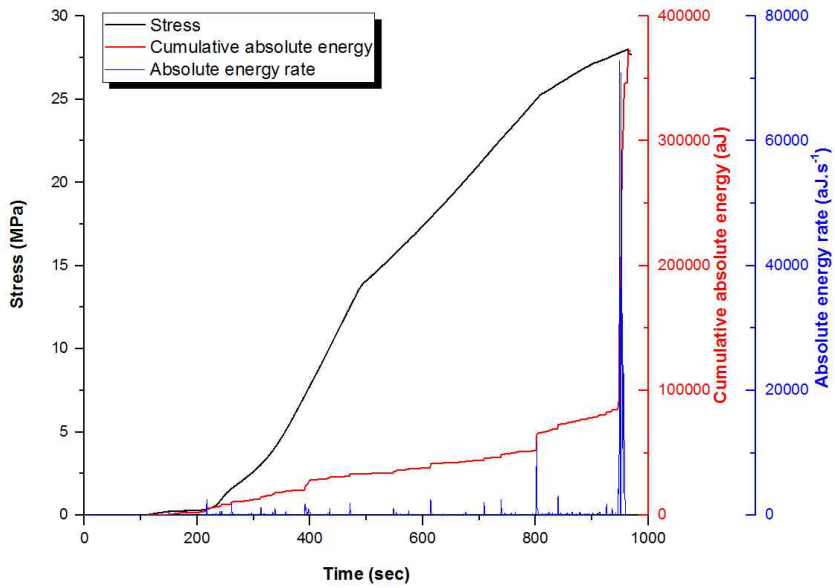


(d) Failed depth and extent

Figure A.1 continued.

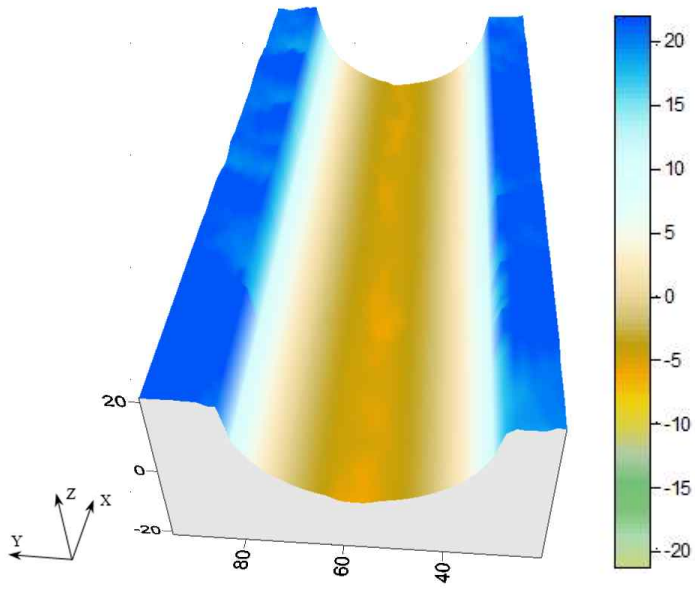


(a) 3D AE source location

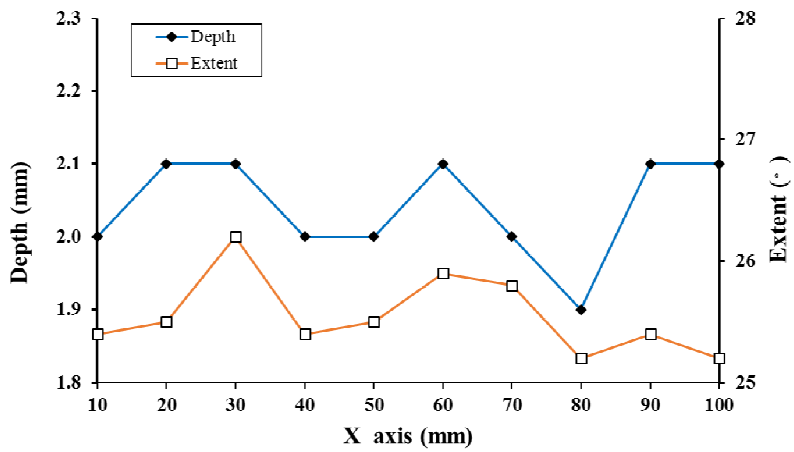


(b) Cumulative absolute energy and energy rate

Figure A.2 Test results of #CM-M2.

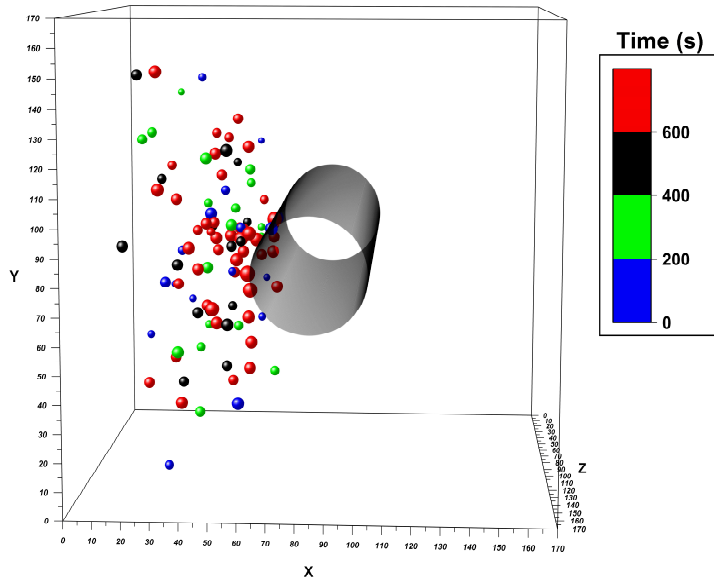


(c) 3D surface of failed zone (Unit: mm)

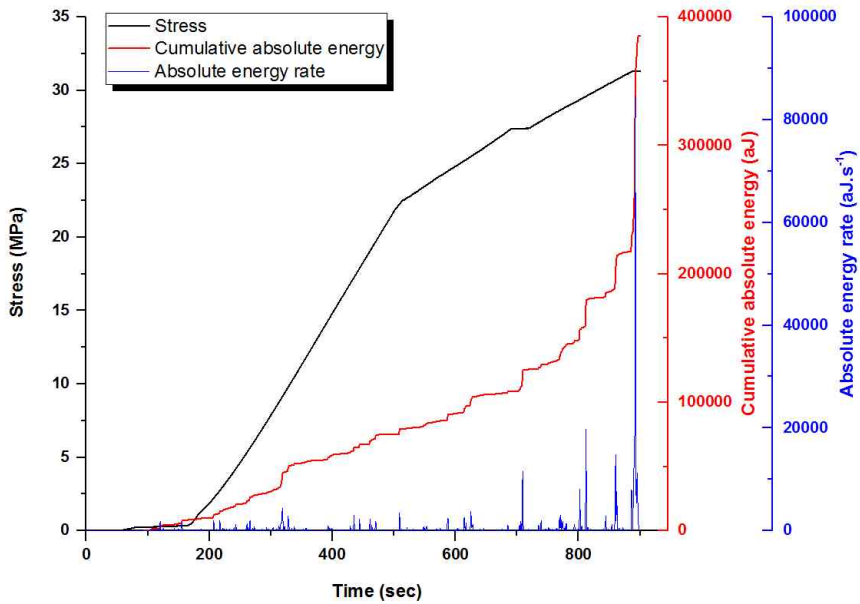


(d) Failed depth and extent

Figure A.2 Continued.

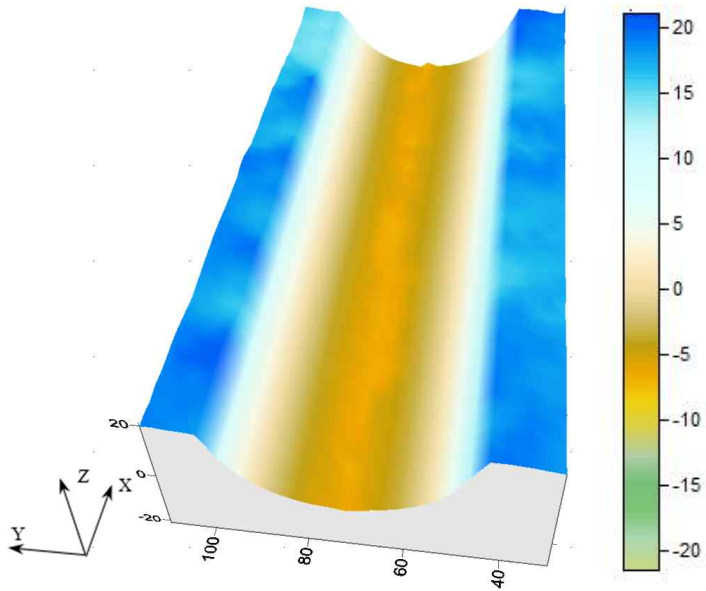


(a) 3D AE source location

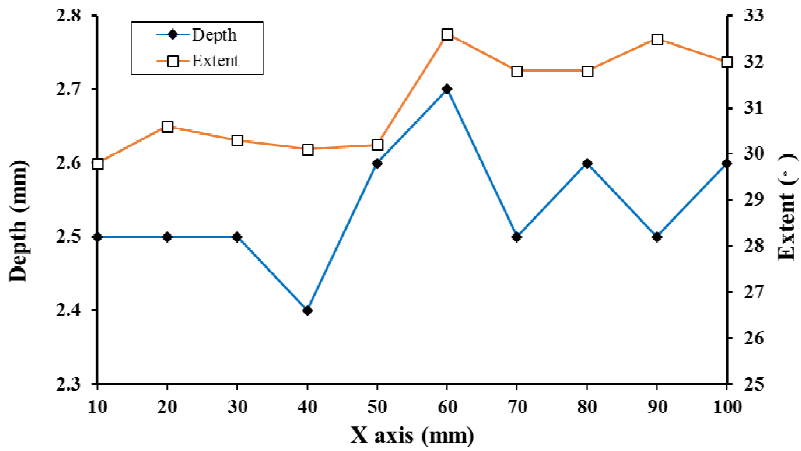


(b) Cumulative absolute energy and energy rate

Figure A.3 Test results of #CM-M3.

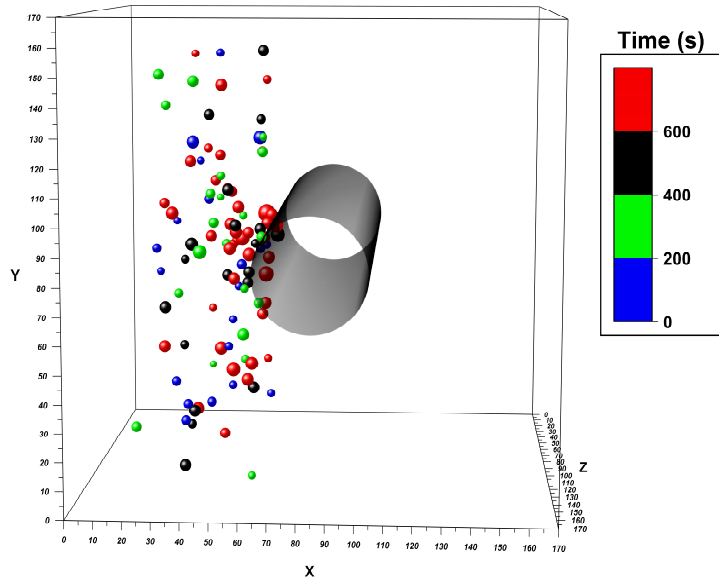


(c) 3D surface of failed zone (Unit: mm)

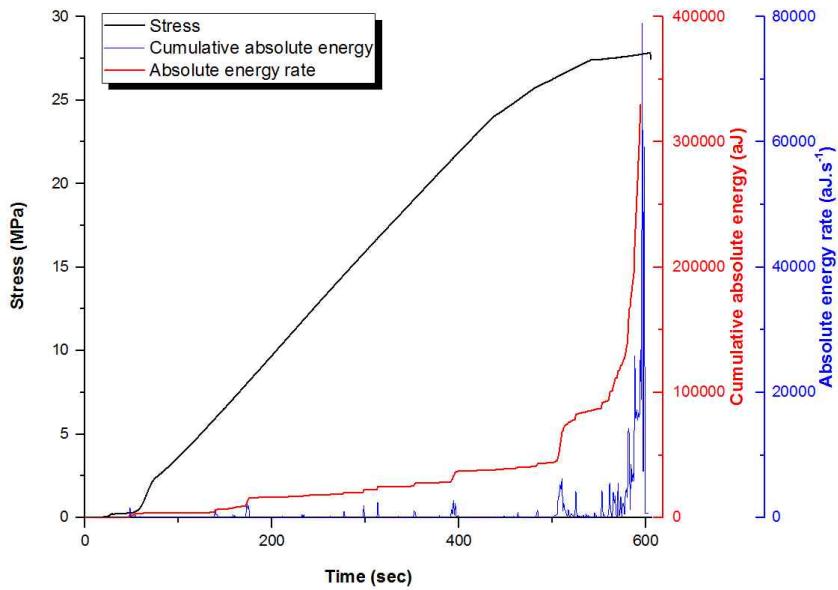


(d) Failed depth and extent

Figure A.3 Continued.

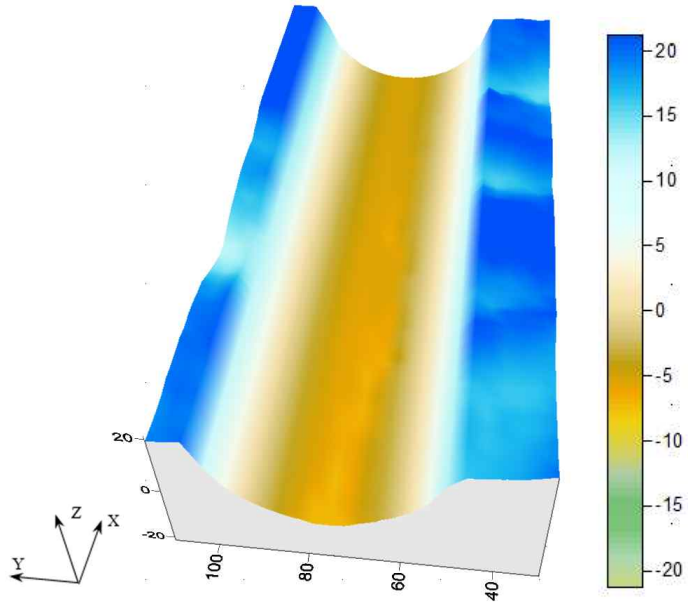


(a) 3D AE source location

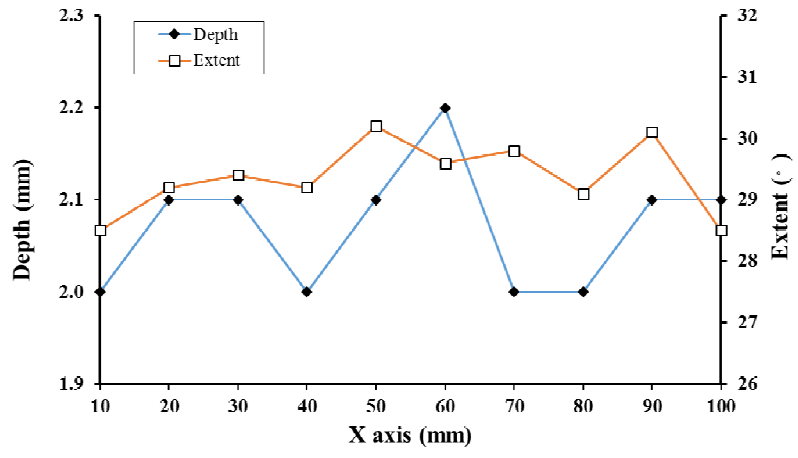


(b) Cumulative absolute energy and energy rate

Figure A.4 Test results of #CM-M4.



(c) 3D surface of failed zone (Unit: mm)



(d) Failed depth and extent

Figure A.4 Continued.

## Appendix B. Heater test preparation process



Figure B.1 Hole drilling for thermocouple installment.



Figure B.2 Heater placement.



Figure B.3 Sand packing.



Figure B.4 Installment of AE sensors and thermocouples.

## 초 록

암반 내에서 온도 증가에 따른 암반손상대(Excavation Damaged Zone, EDZ)영역의 확장은 고준위 방사성 폐기물 처분장의 안정성 평가에 있어 중요한 문제이다. 추가적인 손상으로 인해 발생할 수 있는 열응력은 암반의 역학적 특성을 저하시킬 수 있으며 처분 공동 주변의 EDZ 영역을 확장시켜 핵종의 이동 통로로 작용할 수 있는 위험성이 있다.

이 연구에서는 유사 암석 시료를 사용하여 열-역학적 하중에 의한 공동 주변 손상 영역에 대한 연구를 수행하였다. 정육면체의 시멘트 모르타르 시료를 대상으로 원형 공동 주변에서의 취성 파괴 특성을 조사하였다. 원형 공동 주변에서 발생하는 파괴 과정을 관측하기 위해 미소파괴음(Acoustic emission, AE) 측정 기법을 적용하였다. AE 에너지 절대값을 이용하여 파괴과정을 3 단계로 구분할 수 있음을 규명하였으며 파괴 영역의 깊이와 크기는 3D 레이저 측정기를 통해 계측하였다. 이를 통해 파괴 영역의 깊이와 응력의 크기 간의 상관 관계를 도출하였다.

또한 손상영역에 대한 열응력의 영향을 조사하기 위하여 손상되지 않은(undamaged) 시멘트 모르타르 시험편과 이미 손상된(pre-damaged) 시험편을 대상으로 실내 히터 시험을 수행하였다. 손상되지 않은 시험편의 경우 공동 주변 표면에서 온도 상승으로 인한 별다른 손상이 관측되지 않았다. 반면 이미 손상된 시험편의 경우 원형 공동 주변 표면에서 균열이 발생하였음을 확인하였다.

그러나 추가적인 스폐링(spalling)은 관찰되지 않았으며 이러한 실험 결과들은 ONKALO 지하연구시설에서 단일공에 대해 수행된 히터 테스트와 동일한 결과를 나타냈다.

이축압축 상태에서 원형 공동 주변에서의 취성 파괴를 모사하기 위하여 수치해석을 수행하였으며 유사 암석 시험편의 역학적 물성 불균질성을 모사하기 위하여 탄성 손상 모델을 사용하였다. 이를 토대로 실내 히터 시험을 재현하기 위하여 열-역학적 해석을 수행하였다. 수치해석 결과 온도의 변화와 원형 공동 주변의 손상 영역의 크기는 실험결과와 유사함을 확인하였다. 또한 수치해석 모델의 적용성을 평가하기 위하여 스웨덴의 Äspö 에서 수행된 현장 시험을 모사하고자 하였다. 해석 결과 다른 수치해석 기법을 사용한 결과 및 현장 시험 결과와 잘 일치함을 확인하였다.

이 연구에서는 실내 시험 및 수치해석을 통해 열-역학적 조건에 따른 원형 공동 주변에서의 손상 영역 특성을 규명하고자 하였다. 연구 결과는 고준위 방사성 폐기물의 심지층 처분 시설의 계획 및 시공 시 유용하게 활용될 수 있을 것으로 판단된다.

**주요어:** 열-역학적, 손상영역, 스폐링, 히터 시험, 미소파괴음, 수치해석